

Ultrasound Tomography: An Inverse Scattering Approach

by

Pedram Mojabi

A Thesis submitted to the Faculty of Graduate Studies of

The University of Manitoba

in partial fulfilment of the requirements of the degree of

MASTER OF SCIENCE

Department of Electrical and Computer Engineering

University of Manitoba

Winnipeg

Copyright © 2014 by Pedram Mojabi

Abstract

This thesis is in the area of ultrasound tomography, which is a non-destructive imaging method that attempts to create quantitative images of the acoustical properties of an object of interest (OI). Specifically, three quantitative images per OI are created in this thesis, two of which correspond to the complex compressibility profile of the OI, and the other corresponds to its density profile.

The focus of this thesis is on the development of an appropriate two-dimensional inverse scattering algorithm to create these quantitative images. The core of this algorithm is the Born iterative method that is used in conjunction with a fast and efficient method of moments forward solver, a Krylov subspace regularization technique, and a balancing method. This inversion algorithm is capable of simultaneous inversion of multiple-frequency data, and can handle a large imaging domain. This algorithm is finally tested against synthetic and measured data.

Contributions

The research presented in this thesis was performed in the Electromagnetic Imaging Laboratory (EIL) at the University of Manitoba. Research in the lab has focused on electromagnetic imaging except for the contributions made by Gabriel Faucher on the calibration and inversion of data obtained from a prototype Ultrasound system [1]. The research in this thesis represents the lab's first attempt at using fully non-linear inversion techniques for Ultrasound imaging. Broadly speaking, this thesis contributes to the area of ultrasound tomography by investigating the possibility of simultaneously creating three quantitative images of the object being imaged using time-harmonic scattered pressure data collected outside the object. These three quantitative images are related to three acoustical properties of the object; namely, compressibility, attenuation, and density.

To this end, the following specific contributions have been made:

- A forward scattering algorithm based on the Neumann series was implemented. This algorithm was implemented based on a recently published work*. The Neumann forward solver described in that work was expanded to take into account the variations of both compressibility and density without considering any linear relationship between these two properties.

*Haynes and Moghaddam, IEEE Trans. Biomed. Eng., 57(11), 2010.

- A Method of Moments (MoM) forward solver to handle the complex compressibility and density profiles was implemented. The conjugate gradient algorithm, which is used in this MoM forward solver, requires the definition of the so-called domain operator and its adjoint. This operator and its adjoint have been derived analytically, and implemented numerically.
- The MoM forward solver was equipped with the fast matrix-vector multiplication based on the Toeplitz matrix formulation and a Fourier technique. Also, the use of this formulation allows the implementation of an efficient memory storage technique for this forward solver. The marching-on-source technique was also used to make the convergence of the forward solver faster.
- The Born Iterative Method (BIM) in conjunction with the MoM forward solver was developed to simultaneously reconstruct the complex compressibility and density profiles.
- The BIM was extended to simultaneously invert multiple-frequency data sets.
- A balancing method was developed and implemented to enhance the BIM reconstructions.
- The CGLS regularization technique was used with the BIM method.

Although all of these techniques have been used in the past for such problems as microwave tomography, to the best of the author's knowledge it is the first time that they have been put to use to solve the UT imaging problem. Some of the adjoint operators of the acoustic integral equations formulated in this thesis, which allow simultaneous inhomogeneities in all three parameters: compressibility, attenuation,

and density, and which are required for the implementation of the CG method, have been derived for the first time here.

Acknowledgments

I would like to thank my advisor, Prof. Joe LoVetri, for his guidance and support during my MSc studies. I would also like to thank my friends at the Electromagnetic Imaging Laboratory at the University of Manitoba: Majid Ostadrahimi, Amer Zakaria, Ian Jeffrey, Staci Baran, Colin Gilmore, Gabriel Faucher, Mohammad Asefi, Cam Kaye, Dustin Isleifson, Liang Ding, and Zoran Trajkoski.

I would like to express my appreciation for the time taken by my examining committee members: Prof. Greg Bridges and Prof. Daniel Rickey. The financial support of NSERC is also appreciated.

I would like to thank my family in Winnipeg, Puyan, Shiva, and Hamid, for their kindness and support. Last but not least, my biggest thank-you goes to my parents, Amir and Parvin, and my grandmother.

Table of Contents

List of Tables	ix
List of Figures	x
1 Introduction	1
1.1 Literature Review	4
2 Physics of Acoustics	14
2.1 Inhomogeneous Acoustic Wave Equation	15
2.2 Scattered Field Equation	20
2.3 General Scattered Field Equation	28
3 Forward Solver	32
3.1 Neumann Series Forward Solver	33
3.2 Method of Moments (MoM) Forward Solver	36
3.3 MoM Features	44
3.3.1 Marching-on-in-source technique	44
3.3.2 Toeplitz Block Matrix	48
3.3.3 Fast Fourier Transform (FFT) Multiplication	52
4 Inverse Solver	61
4.1 Born Iterative Method (BIM)	63
4.2 Data Operator	65
4.3 Efficient implementation of the data operator	70
4.4 Balancing of the Contrasts	72
4.5 Simultaneous frequency inversion	79
5 Regularization Methods	84
5.1 Why do we need a regularization?	85
5.2 The Singular Value Decomposition	86
5.3 Truncated Singular value Decomposition	90
5.4 Tikhonov Regularization	90
5.5 CGLS Regularization	95

6	Results	102
6.1	Synthetic Results	102
6.1.1	Reconstruction of a cylinder	103
6.1.2	Reconstruction of two cylinders	105
6.1.3	Two Cylinders Without Applying Balancing Method	111
6.1.4	Two-cylinders reconstruction with reduced information	113
6.1.5	Two cylinders with different contrast profiles	115
6.1.6	Simple Synthetic Breast Model	116
6.2	Measurement Results	126
7	Summary, Conclusions and Future Work	132
7.1	Summary and Conclusions	132
7.2	Future Work	135
A	Discretization of the Forward Model	137
B	Conjugate Gradient Method	142
C	Multiplicative Regularization	145
D	L_1-norm Regularization	156
E	Flowchart of the Inversion Algorithm	159
	References	161

List of Tables

6.1	Data misfit for different iterations of the BIM inversion algorithm for the cylinder with a radius of $1.7\lambda_{min}$	105
6.2	Data misfit for different iterations of the BIM inversion algorithm for the case that the OI is two cylinders with the same contrast profiles. Three percent noise is added and also balancing coefficients are applied.	110
6.3	Data misfit for different iterations of the BIM inversion algorithm for two cylinders without applying a balancing method.	111
6.4	Data misfit for different iterations of the BIM inversion algorithm for two cylinders using a single frequency.	115
6.5	Residual error for each contrast profile with respect to the exact value of contrast profile for the case that the OI is two cylinders with different contrast profiles. These values for each iteration of the BIM are shown below.	116
6.6	Ultrasound properties for breast tissue at $22^{\circ}C$	120
6.7	χ_1^c and χ_2 for breast tissues at $22^{\circ}C$	120
6.8	Residual error and data misfit for the breast model within a $12\lambda_{min} \times 12\lambda_{min}$ imaging domain. These values for each iteration of the BIM are shown below.	122

List of Figures

1.1	Ultrasound tomography setup in which the object of interest (OI) is enclosed by an array of ultrasound transmitters/receivers.	2
3.1	Comparison between the calculated scattered pressure using the Neumann series and MoM forward solver. (a) the real part of χ_1^c of the OI. (b) The imaginary part of χ_1^c of the OI. (c) Contrast of inverse density, χ_2 , of the OI. (d) Comparing the magnitude of the scattered pressure at receiver positions using Neumann and MoM forward solver. (e) Comparing the phase of scattered pressure at receiver positions using Neumann and MoM forward solver.	42
6.1	True contrast profiles: (a) the real part of compressibility contrast, (b) the imaginary part of compressibility contrast, and (c) the contrast of inverse density.	104
6.2	Simultaneous reconstruction of χ_1^c and χ_2 for the cylinder data set with three percent noise. The first, second, third, fourth and fifth rows correspond to the reconstruction of the contrast profiles at the 1 st , 2 nd , 4 th , 6 th , and 8 th iterations of the BIM respectively.	106
6.3	True value of contrast profiles for two identical cylinders. The size of the domain is $10\lambda_{\min} \times 10\lambda_{\min}$. (a) the real part of the contrast of compressibility (b) the imaginary part of contrast of compressibility and (c) the contrast of inverse density.	107
6.4	Simultaneous reconstruction of χ_1^c and χ_2 for the two cylinder data set with 3% noise based on the average value. The first, second, third, fourth and fifth rows correspond to the reconstruction of contrast profiles for the 1 st , 3 rd , 5 th , 7 th and 11 th iterations of the BIM inversion algorithm respectively.	109
6.5	Simultaneous reconstruction of χ_1^c and χ_2 for the two cylinder data set with three percent noise using the maximum value.	110
6.6	Simultaneous reconstruction of χ_1^c and χ_2 for two cylinders without applying the balancing method. The first, second, third, fourth and fifth rows correspond to the reconstruction of contrast profiles for the 1 st , 3 rd , 5 th , 6 th and 9 th iterations of the BIM, respectively.	112

6.7	Simultaneous reconstruction of χ_1^c and χ_2 for two cylinders using a single-frequency data set. The first, second, third, fourth, and fifth rows correspond to the reconstruction of contrast profiles for the 1 st , 2 nd , 3 rd , 5 th and 6 th iterations of the BIM, respectively.	114
6.8	Simultaneous reconstruction of χ_1^c and χ_2 for two cylinders with different contrast profiles. The first row is the true value of the contrast profiles. The second, third and fourth rows correspond to the reconstruction of contrast profiles for the 1 st , 4 th and 11 th iterations of the BIM respectively.	117
6.9	Antidiagonal cut from the bottom left corner to the top right for the case that the OI is two cylinders with different contrast profiles. The first, second and third rows correspond to the first, fourth and eleventh iterations of the BIM. The solid blue line corresponds to the actual contrast profiles and the dashed red line corresponds to the reconstructed contrast profiles	118
6.10	True value of χ_1^c and χ_2 for breast tissues for the case that the size of imaging domain is $12\lambda_{\min} \times 12\lambda_{\min}$	122
6.11	Reconstruction of χ_1^c and χ_2 for the breast model within a $12\lambda_{\min} \times 12\lambda_{\min}$ imaging domain. The first, second, third, fourth, and fifth rows correspond to the reconstruction of the contrast profiles for the 1 st , 3 rd , 5 th , 6 th , and 8 th iteration of the BIM, respectively.	123
6.12	Diagonal cut from the top left corner to the bottom right for the breast model within a $12\lambda_{\min} \times 12\lambda_{\min}$ imaging domain. The first, second, third, fourth and fifth rows correspond to the first, third, fifth, sixth and eighth iterations of the BIM. The solid blue line corresponds to the actual contrast profiles and the dashed red line corresponds to the reconstructed contrast profiles	124
6.13	Reconstruction of χ_1^c and χ_2 for the breast model within a $12\lambda_{\min} \times 12\lambda_{\min}$ imaging domain and three percent noise is added. A single frequency is used and the balancing method is not applied. The first, second, third, fourth, and fifth row correspond to the reconstruction of the contrast profiles for the 1 th , 2 th , 4 th , 6 th , and 8 th iterations of the BIM inversion algorithm respectively.	125
6.14	Simultaneous reconstruction of χ_1^c and χ_2 for the realistic numerical breast model. The size of the domain is 11.6 cm by 11.6 cm ($22\lambda \times 22\lambda$). $nRx, nTx = 120$, $n_f = 7$ and $250\text{KHz} \leq f \leq 280\text{KHz}$. Four BIM iterations are used. The number CGLS iterations used in this example are 4, 18, 50 and 80.	127
6.15	The ultrasound measurement system at the Electromagnetic Imaging Laboratory at the University of Manitoba.	130
6.16	Simultaneous reconstruction of χ_1^c and χ_2 for two wires.	130
6.17	Simultaneous reconstruction of χ_1^c and χ_2 for three wires.	131

A.1	Calculation of ∇p_{ij} for the 2D case using the central finite difference approximation.	139
A.2	The discretization of the imaging domain using square cells is shown in this figure. n_x and n_y are the number of elements in the x and y axis. The red dashed circle represents the location of the transducers.	141
C.1	circle 1 is the inhomogeneous region. circle 2 and circle 3 are the homogeneous region.	152
D.1	A linear function used to compare the penalty term for L_1 -norm with Tikhonov regularization.	157

List of Algorithms

5.1	CGLS Algorithm	101
-----	--------------------------	-----

Introduction

This thesis presents research work in the area of ultrasound tomography (UT). In UT, the goal is to create quantitative images of the compressibility and density profiles of the object of interest (OI) from ultrasound data collected outside the OI. This information can be of use in biomedical diagnosis such as breast cancer imaging where it may allow one to differentiate malignant tissues from healthy tissues. The fact that the data is collected outside the OI makes this imaging modality a non-invasive method; thus, removing the need for biopsy.

As far as the UT data collection is concerned, the OI is surrounded by several transducers as shown in Fig 1.1. Each of these transducers can either work as a transmitter or a receiver of ultrasound energy. When one transducer operates as a transmitter, the others work as receivers. This procedure continues until all the transducers act as a transmitter [2–5]. Different frequencies can also be used to generate more information about the OI [6–13]. The region of interest in the absence of the OI and transducers is called the background medium. The background medium is usually a known homogeneous medium, and is chosen in such a way that the reflection from the OI is minimized. For example, for breast imaging applications, it is common to use water as the background medium [7, 14]. This is due to the fact that the relevant physical parameters of breast tissues match closely to those of

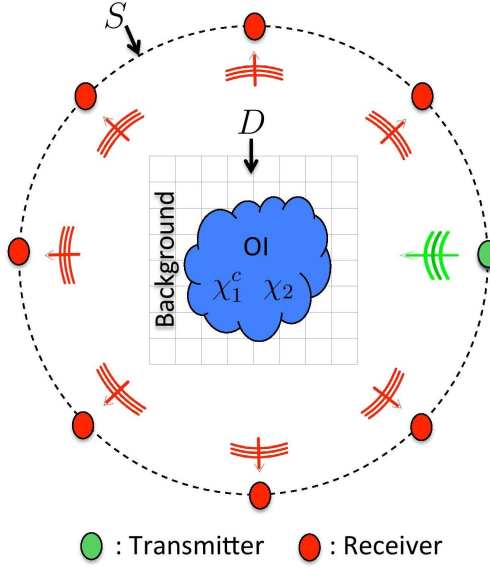


Figure 1.1: Ultrasound tomography setup in which the object of interest (OI) is enclosed by an array of ultrasound transmitters/receivers.

water. Therefore, much of the energy in the ultrasound waves penetrates into the breast tissues; thus, extracting more information from the OI.

Two domains are defined in UT. The first one containing the OI and a background medium is called the imaging domain and denoted by D as shown in Fig 1.1. The second domain containing all the transmitters and receivers is called the data domain and denoted by S as shown in Fig 1.1. It should be noted that the data domain is outside the imaging domain.

The data to be used in UT is the scattered field data. To obtain scattered field information, the measurements are first performed in the background medium in the absence of the OI. This measured data is usually called the incident field measurement. Next, the same measurement is performed in the presence of the object of interest. This set of data is usually called the total field data. Subtraction of the incident field

data from the total field data yields the scattered field data, which serves as the input data to the UT problem.

The UT problem can then be mathematically formulated as an inverse scattering problem, which is nonlinear and ill-posed [6, 7, 15, 16]. The non-linearity comes from the fact that the two unknowns in this problem, i.e., (1) contrast profiles of the compressibility and density, and (2) the total field inside the imaging domain, are nonlinearly related to each other. Also, one of the main challenges in solving the inverse problem associated with UT is that a small change in the measured data can result in a large change in the predicted contrast profiles (instability). According to the definition of ill-posed problems given by Hadamard [17], the UT problem is, therefore, ill-posed.

To quantitatively solve this nonlinear and ill-posed problem, different types of iterative algorithms have been proposed such as the Born iterative method (BIM) [6, 7, 18], the Distorted Born Iterative Method (DBIM) [19–22] and the Contrast Source Inversion (CSI) method [23]. These algorithms first create some form of cost function which includes the discrepancy between the measured data and the simulated data due to some predicted contrast profiles. They will then try to minimize this cost function using different optimization methods. Due to the ill-posedness of the problem, different regularization methods should be used in these inversion algorithms such as Krylov subspace regularization [24, 25], Tikhonov [22, 26–29], Multiplicative [30, 31] or L_1 -norm [32, 33] regularization methods. At each iteration of these inversion algorithms, the contrast profiles and the total field inside the imaging domain is updated. The algorithm is terminated when the discrepancy between the measured data and the simulated data is sufficiently small.

1.1 Literature Review

Relatively speaking, there has not been much research work that has focused on the development of appropriate inversion algorithms, to be used with UT, to quantitatively reconstruct various acoustic properties of an OI. Even less, has been published on the simultaneous reconstruction of the compressibility, density, and attenuation profiles. As will be shown in subsequent chapters, these are converted into a complex valued compressibility profile and a real valued density profile. Here, a short literature review of the potential application areas of interest to the author and of previous UT work is outlined so as to set the context of the research that will be presented.

Probably the most studied application of biomedical ultrasound tomography is in the area of breast cancer detection [7, 34–38]. Breast cancer is currently the second most common occurring cancer across the world and is ranked first in the number of cancer occurrences in women. It is estimated that around 1,152,000 new breast cancer cases occurs each year, and around 411,000 people die per year due to this cancer [39]. Early detection of breast cancer is crucial in dealing with this problem. To achieve this goal, imaging methods which have a good resolution to detect breast cancer in its early stage are needed. Such imaging methods should also distinguish between benign and malignant tumors. Recently, microwave and ultrasound tomography using inverse scattering methods have been investigated as alternatives to the current imaging methods such as X-ray mammograms, Magnetic Resonance Imaging (MRI), X-ray Computed tomography (CT) and conventional ultrasound imaging [40]. In what follows, some other imaging methods are briefly described.

MRI is a high resolution imaging method and can be used for early detection of breast cancer. However, this method has some disadvantages: (1) its high cost, (2) it

is not portable (3) and it requires the use of contrast agents for breast imaging [36,41]. X-ray mammography is based on the absorption of photons in different tissues. In this method, it is assumed that the cancer mass is denser than the healthy tissues and it also has different attenuation. As far as the sensitivity is concerned, this method is not good for women with dense breasts. This is due to the fact that the variation of density is an important criteria to be considered. That is, some healthy tissues may have the same density as cancerous tissue and it is difficult to distinguish these tissues from cancer masses [34, 36, 41, 42]. X-rays are ionizing radiation which, if possible, is better to avoid [43]. In addition, microwave tomography (MWT) is also being investigated for breast cancer imaging applications. However, at the current state-of-the-art, the resolution achievable from MWT is not sufficient for early detection of breast tumors. The Electromagnetic lab at the University of Manitoba is investigating the hybridization of UT with MWT as future work.

The invention of the supersonic reflectoscope was the starting point of ultrasound imaging [1, 44]. Since then, different types of ultrasound imaging techniques such as sonography and Ultrasound Tomography have been proposed to reconstruct an image of the OI. Sonography is more accurate in dense breast imaging compared to the X-ray mammography. The main problem with this method is that it is operator dependent. To solve this problem, one should have a fixed measurement system that is not dependent on the person doing the measurements [36].

Ultrasound Tomography (UT) is a quantitative imaging system which has much potential for biomedical imaging. As described previously, UT uses ultrasonic waves to interrogate the OI and create acoustic property profiles or images of the OI. These can be 2D tomographic images or full 3D images. Different approaches are available to process the data collected in a UT system including (1) Time of Flight tomography

[36, 42, 45], (2) Diffraction Tomography [34, 36, 46–48], and (3) Full-wave inversion algorithms. The focus of this thesis is on full-wave inversion algorithms because these can provide quantitative images of many more acoustical properties of the OI. However, in what follows, we briefly describe the other two processing methods.

Time of Flight tomography (TFT) is one of the most important approaches for creating images from ultrasonic data [36]. In this method, instead of solving the full-wave equation, which is computationally very expensive, the geometrical acoustic ray approximation is used to reconstruct the image of the OI. This method is computationally more efficient than solving the full-wave equation [45]. Two different approaches are applied in TFT. In the first approach, it is assumed that the wave propagates in the straight line (ray approximation). This approximation leads to a linear problem. The second approach uses a better “bent” or “diffracted” ray approximation to model the wave propagation inside the OI and is thus better, or more accurate, than the first approach (which uses a direct ray) [36, 45]. In this method, time of flight can be found using the relationship between the speed of the sound and propagation paths. This second approach leads to a nonlinear ill-posed problem. The nonlinearity of this problem is due to the fact that both the speed of the sound and propagation paths are unknown and nonlinearly related to each other [45]. Therefore, within the framework of the bent ray for TFT, some researchers have defined a cost function and then tried to minimize it using optimization methods. Regularization is required for this problem due to its ill-posedness [45]. The goal of solving this problem is to reconstruct the speed of the sound and attenuation within the OI [42]. The resolution obtained using this method has not been particularly good, and therefore it is not a good method for early detection of breast cancer [36].

Diffraction tomography is based on the first-order (Born) approximation which

linearizes the wave propagation within the OI [36, 47, 48]. It simply assumes that the total field inside the domain is equal to the incident field and thus removes one of the unknowns from the problem [47]. That is, now the only unknown in the problem will be the contrast profile. Therefore, this method can only be used for low-contrast objects where the total field inside the imaging domain will be close to the incident field. To satisfy this condition the object should be (1) small compared to the utilized wavelength, and (2) should have a low contrast compared to the background medium [34, 36, 46]. As is obvious based on these criteria, this method is not suitable for breast imaging due to the fact that the size of the breast is usually much larger than the wavelength of operation.

Full-wave UT methods can be very accurate for reconstructions of the OI. The key in these algorithms is their ability to take into account multiple scattering events within the OI. That is, as opposed to the TFT and diffraction tomography algorithms, full-wave UT methods attempt to model the wave interaction (multiple scattering) within the OI without any approximations. Within the framework of these full-wave methods, the UT problem is mathematically cast as a nonlinear inverse scattering problem where both the contrast profiles and the total field inside the imaging domain are taken to be the unknown [7, 18]. Different inversion algorithms can be used to solve this inverse scattering problem; e.g., the Born Iterative Method (BIM), the Distorted Born Iterative Method (DBIM), and the Contrast Source Inversion Method (CSI). All of these inversion methods are iterative methods for solving the nonlinear inverse scattering problem. When they work, they can provide more accurate reconstructions with enhanced resolution over TFT and diffraction tomography. These full-wave UT methods are the focus of this thesis.

As mentioned earlier, our goal is to find the quantitative properties of the OI

which are the complex valued compressibility and density profiles. In most of the papers published in this area, it is assumed that the density profile is constant and the only unknown is the compressibility profile [21, 22, 49–51]. However, the density profile in most human imaging applications is not a constant as a function of position; for example, experimental results show that the variation of density affects the reconstruction of sound speed in human tissues [20, 52]. In [7], the authors used an improved approach in which they assumed a linear relationship between the contrast of compressibility and density profiles. Therefore, the effect of density profile is only partially taken into account in this approach. The advantage of assuming such a linear relationship is that the number of unknowns will remain the same as in the case where the density is assumed to be constant. However, assuming this linear relationship does not provide very accurate reconstructions.

It is thus concluded a premise of the research described in this thesis is that both the density and the complex valued compressibility profiles should be treated as unknowns in the UT problem so as to achieve a more accurate reconstruction and obtain as much information as possible in the images of the OI. In some papers, various manifestations of these properties have been solved for as unknowns; e.g., see [6, 18–20, 23, 53]. These papers might be classified into two categories. The first category [19, 20] formulates the problem in such a way that the final result consists of two images: (1) an image of the sound speed profile, and (2) an image of the attenuation profile. In the second category [6, 18, 23, 53], the problem is formulated in such a way that the final result consists of three different images: (1) an image of the compressibility profile, (2) an image of the density profile, and (3) an image of the attenuation profile. Therefore, in the second category, the number of unknowns is greater than the first case and thus more computationally expensive. However,

the advantage of this method is that one gets more information about the OI. This thesis is focused on this second category but as will be shown in the next Chapter, it is more efficient to define a complex valued compressibility which takes into account compressibility and attenuation.

Inversion algorithms require a forward solver either explicitly or implicitly. Most forward solvers that have been proposed for UT assume that the OI has a constant density profile. For example, a conjugate gradient Method of Moments method has been used as a forward solver in [49]. The multilevel fast multipole algorithm (MLFMA) has also been proposed as a fast forward solver that can be used for this application [21]. Time-domain and a frequency-domain eigenfunction methods have also been proposed in [50] and [51], respectively. However, all of these forward solvers assume that the density profile of the OI is a constant (no spatial variation).

Some forward solvers have also been proposed to simultaneously account for variable density and compressibility profiles. For example, in [20], the T-matrix approach is used for this purpose. According to this paper, the T-matrix approach has difficulty to converge when the size of the object is on the order of the wavelength. To solve this problem, the frequency hopping approach was used. In [15], the fast multipole method (FMM) was used as a forward solver. In [18], a time-domain method was used as a forward solver, however, the inversion algorithm used in conjunction with this time-domain forward solver is in the frequency domain. The time-domain results obtained from this forward solver were transferred to the frequency-domain using the Fast Fourier transform (FFT). It should be noted that the main reason for having a frequency-domain inverse solver is that inversion in the time-domain is very computationally expensive [16].

In this thesis, we have implemented a Method of Moments (MoM) forward solver

based on the Conjugate Gradient (CG) method and the FFT for the general case in which both the compressibility and density profiles are non-constant. This forward solver has some features that make it fast and efficient: (1) only one row of the MoM matrix needs to be calculated and stored in this code due to the use of Toeplitz block matrix properties, (2) the FFT is used to accelerate the matrix-vector multiplications, (3) marching-on-source is implemented to provide a better initial guess for the CG solver; thus, resulting in faster convergence, and (4) the magnitudes of the unknowns are appropriately balanced to provide a more accurate solution [54].

Different nonlinear inversion algorithms have been proposed in MWT and can also be used in UT as well, including the BIM [6, 7, 18], the DBIM [19–22] and the CSI [23]. BIM is used in this thesis as the nonlinear inversion algorithm. The main reason for choosing BIM as our inversion algorithm is that BIM is faster and more efficient compared to the other two methods especially when we are simultaneously dealing with two unknowns, *i.e.* the compressibility and density profiles [7]. It should be noted that DBIM and CSI can generally provide better reconstructions of high-contrast objects compared to BIM. However, for biomedical imaging applications, if the background medium is chosen wisely so as to minimize the reflection from the OI, tissues will have relatively low contrast (less than one) [7]. This justifies the use of BIM as opposed to DBIM and CSI for this application.

As previously mentioned, this problem is an ill-posed problem. Therefore, regularization is required. For ill-posed problems, different regularization techniques have been proposed such as the Conjugate Gradient Least Squares (CGLS) method [24, 25, 27], different forms of Multiplicative regularization [30, 31], Tikhonov regularization [22, 26–28] and the L_1 -norm [32, 33] regularization. In Tikhonov regularization, the two-norm of the solution is added to the cost function. This term has a weighting

coefficient called the regularization parameter. The regularization parameter can be found using several techniques such as the L-curve method [27] and the Generalized Cross Validation (GCV) [55]. Finding a regularization parameter is computationally very expensive especially for large domain problems. In nonlinear ill-posed problems, such as the UT problem, the regularization parameter should be found at each iteration of the inversion algorithm; this makes the whole process even more computationally expensive. In L_1 -norm regularization, a term which is the one-norm of the solution is added to the cost function. This regularization is very good in finding the edges of the OI. However, it is computationally more expensive compared to the other methods [32, 33]. Multiplicative regularization [30, 31] is another regularization technique in which the regularization term is multiplied against the original cost function. The main advantage of the multiplication regularization technique is that it automatically finds the regularization parameter at each iteration of the algorithm. Therefore, there is no need to use another method such as the L-curve to find the regularization parameter at each iteration of the algorithm. Moreover, this regularization also has edge-preserving characteristics.

The CGLS regularization method [24, 25, 27] is used in this thesis. This method has been successfully used for the MWT problem. Here, we show how it can be applied to the UT problem. In the CGLS regularization scheme, the solution is iteratively projected onto a Krylov subspace. In early iterations of the CGLS algorithm, the low-spatial frequency components of the contrast profiles are reconstructed. As the algorithm goes on with more iterations, it gradually reconstructs more of the higher spatial frequency components of the contrast profiles. In this method, the regularization parameter becomes the iteration number at which one terminates the CGLS algorithm. The main advantage of this regularization technique is that it is extremely

fast as it only relies on simple matrix-vector multiplications [24,25,27]. However, this algorithm, in its current form, is not capable of providing edge-preserving reconstruction. In UT, the domain size is extremely large compared to the wavelength. Therefore, in practical situations, we always deal with large-scale problems; thus, fast regularization methods are of necessity.

As the size of the imaging domain in UT is usually much larger than the wavelength, after discretizing the imaging domain the number of unknowns will be very large. On the other hand, the data is usually collected on a circle around the OI with a limited number of transducers. Therefore, the number of unknowns is usually larger than the number of measured data. To compensate for this imbalance between the number of measured data points and the number of unknowns, we perform our measurements at multiple frequencies so as to generate more information about the OI. This complicates the development of the inversion algorithm as multiple-frequency data needs to be processed by the algorithm. There are two different ways to process multiple-frequency data sets. In the first method, called the frequency-hopping technique, the inversion is first applied to the lowest frequency data set. The converged image is then given as the initial guess to the inversion algorithm with the next higher frequency data set. This process continues until all frequency data sets have been used. In other words, the frequency-hopping technique attempts to first reconstruct low resolution information about the OI. As we use higher frequency data sets, the algorithm will provide higher resolution information about the OI [8,9,19]. In the second method, which is called simultaneous frequency inversion [6,10–13], all the multiple-frequency data sets are used at the same time to reconstruct the OI. The simultaneous frequency inversion method is much more complicated in terms of code development compared to the frequency-hopping technique. However, the re-

sults obtained using this method are usually much better than those obtained with the frequency hopping technique.

The rest of this thesis is structured as follows. The physics of acoustics relevant to the work presented in this thesis is described in Chapter 2. Chapter 3 describes the forward scattering solver that was developed for this research. The inverse solver utilized in this thesis is then described in detail in Chapter 4. The regularization method used in conjunction with the inverse algorithm, as well as some overview of other common regularization techniques, are described in Chapter 5. Numerical results are then presented in Chapter 6. Finally, conclusions and some ideas for future work are outlined in Chapter 7.

2

Physics of Acoustics

There are several similarities between electromagnetic and ultrasonic waves [56]. For example, pressure, velocity, compressibility and density are analogous to electric field, magnetic field, permittivity and permeability, respectively [1]. Therefore, methods used in electromagnetics are often applicable to ultrasonic wave modelling. One of the main differences between ultrasonic and electromagnetic waves lies in the arrangement of the field components. The velocity field components in ultrasonic pressure waves are in the direction of the wave propagation; thus, they are sometimes called longitudinal waves. On the other hand, the arrangement of the electromagnetic field components is generally perpendicular to the direction of the wave propagation for simple plane waves; thus, they are sometimes referred to as transverse waves [56, 57].

In Section 2.1, the inhomogeneous acoustic wave equation will be formulated using the conservation of mass and linear momentum laws. Then in Section 2.2, the equations for the scattered field will be derived using the assumption that the magnitude of the imaginary part of the wavenumber is much less than the magnitude of the real part of the wavenumber [58]. In Section 2.3, the general form of the scattered field equation without using the previous assumption will be derived.

2.1 Inhomogeneous Acoustic Wave Equation

The acoustic wave equation is the basis on which to model the scattered field in a UT system. Here we follow the development given in [1, 56, 59].

To derive the acoustic wave equation, the following forms of the conservation of mass and linear momentum are used:

- Conservation of mass [56]: in an isolated system, the mass will remain constant. Thus, the rate of density change is set to zero.

$$\frac{d}{dt} \int_{V(t)} \rho(\mathbf{r}, t) dv = 0 \quad (2.1)$$

where $V(t)$ is the volume which can be changing with the time t and \mathbf{r} is the position vector. ρ [$\frac{\text{kg}}{\text{m}^3}$] is the fluid mass density. Applying the Liebnitz identity to (2.1), we have

$$\begin{aligned} \frac{d}{dt} \int_{V(t)} \rho(\mathbf{r}, t) dv &= \int_{V(t)} \frac{\partial \rho(\mathbf{r}, t)}{\partial t} dv + \oint_{A(t)} \rho(\mathbf{r}, t) \mathbf{u}(\mathbf{r}, t) \cdot \hat{n} da \\ &= \int_{V(t)} \left(\frac{\partial \rho(\mathbf{r}, t)}{\partial t} + \nabla \cdot [\rho(\mathbf{r}, t) \mathbf{u}(\mathbf{r}, t)] \right) dv = 0 \end{aligned} \quad (2.2)$$

where $\mathbf{u}(\mathbf{r}, t)$ [$\frac{\text{m}}{\text{s}}$] is the velocity of the surface and $A(t)$ is a closed surface. Thus,

$$\frac{\partial \rho(\mathbf{r}, t)}{\partial t} + \nabla \cdot [\rho(\mathbf{r}, t) \mathbf{u}(\mathbf{r}, t)] = 0 \quad (2.3)$$

- Conservation of linear momentum [56] : Linear momentum is the product of velocity and mass. This law says if we have a closed surface and we assume that we don't have any external forces, the linear momentum cannot be changed [1,

56]:

$$\frac{d}{dt} \int_{V(t)} \rho(\mathbf{r}, t) \mathbf{u}(\mathbf{r}, t) dv = \int_{V(t)} \mathbf{F}(\mathbf{r}, t) dv \quad (2.4)$$

where $\mathbf{F}(\mathbf{r}, t)$ [$\frac{N}{m^3}$] is the total force on the volume of fluid and it can be found as [1, 56]

$$\mathbf{F}(\mathbf{r}, t) = -\nabla p(\mathbf{r}, t) \quad (2.5)$$

where p [$\frac{N}{m^2}$] is the pressure. In the above equation, it is assumed that viscosity and external forces are zero. Applying the Liebnitz identity to the (2.4), we have

$$\begin{aligned} \frac{d}{dt} \int_{V(t)} \rho(\mathbf{r}, t) \mathbf{u}(\mathbf{r}, t) dv &= \int_{V(t)} \frac{\partial}{\partial t} [\rho(\mathbf{r}, t) \mathbf{u}(\mathbf{r}, t)] dv + \oint \rho(\mathbf{r}, t) \mathbf{u}(\mathbf{r}, t) \mathbf{u}(\mathbf{r}, t) \cdot \hat{n} da \\ &= \int_{V(t)} \left[\frac{\partial}{\partial t} [\rho(\mathbf{r}, t) \mathbf{u}(\mathbf{r}, t)] + \nabla \cdot [\rho(\mathbf{r}, t) \mathbf{u}(\mathbf{r}, t) \mathbf{u}(\mathbf{r}, t)] \right] dv \\ &= \int_{V(t)} \mathbf{F}(\mathbf{r}, t) dv = \int_{V(t)} -\nabla p(\mathbf{r}, t) dv \end{aligned} \quad (2.6)$$

According to (2.6), we can conclude that

$$\frac{\partial}{\partial t} [\rho(\mathbf{r}, t) \mathbf{u}(\mathbf{r}, t)] + \nabla \cdot [\rho(\mathbf{r}, t) \mathbf{u}(\mathbf{r}, t) \mathbf{u}(\mathbf{r}, t)] = -\nabla p(\mathbf{r}, t) \quad (2.7)$$

We can also define density, pressure and velocity as a constant number plus some fluctuations as [1, 56]

$$\begin{aligned} \rho &= \rho_0 + \rho_1(\mathbf{r}, t) \\ p &= p_0 + p(r, t) \\ \mathbf{u} &= \mathbf{u}_0 + \mathbf{u}(\mathbf{r}, t) \end{aligned} \quad (2.8)$$

We also have the following relation [1, 56]

$$\frac{\partial p}{\partial \rho} = \frac{\kappa'}{\rho} \quad (2.9)$$

where κ' is the incompressibility. Substituting (2.8) into (2.9), we have

$$\frac{p(\mathbf{r}, t)}{\rho_1(\mathbf{r}, t)} = \frac{\kappa'}{\rho_0} \quad (2.10)$$

or

$$\rho_1(\mathbf{r}, t) = \frac{\rho_0}{\kappa'} p(\mathbf{r}, t) \quad (2.11)$$

Substituting (2.8) and (2.11) into (2.3) and (2.7), we have [59]

$$\nabla p(\mathbf{r}, t) = -\rho(\mathbf{r}) \frac{\partial \mathbf{u}(\mathbf{r}, t)}{\partial t} \quad (2.12)$$

$$\nabla \cdot \mathbf{u}(\mathbf{r}, t) = -\frac{1}{\kappa'} \frac{\partial p(\mathbf{r}, t)}{\partial t} \quad (2.13)$$

If it is assumed that pressure and velocity have a $e^{+j\omega t}$ time dependency then the frequency domain version of (2.12) becomes

$$\nabla p(\mathbf{r}) = -j\omega\rho(\mathbf{r})\mathbf{u}(\mathbf{r}) \implies \mathbf{u}(\mathbf{r}) = \frac{j}{\omega\rho(\mathbf{r})}\nabla p(\mathbf{r}) \quad (2.14)$$

The vector $\mathbf{u}(\mathbf{r})$ can be written as

$$\mathbf{u}(\mathbf{r}) = u_x(\mathbf{r})\hat{x} + u_y(\mathbf{r})\hat{y} + u_z(\mathbf{r})\hat{z} \quad (2.15)$$

where

$$u_x(\mathbf{r}) = \frac{j}{\omega\rho(\mathbf{r})} \frac{\partial p(\mathbf{r})}{\partial x} \quad (2.16)$$

$$u_y(\mathbf{r}) = \frac{j}{\omega\rho(\mathbf{r})} \frac{\partial p(\mathbf{r})}{\partial y} \quad (2.17)$$

$$u_z(\mathbf{r}) = \frac{j}{\omega\rho(\mathbf{r})} \frac{\partial p(\mathbf{r})}{\partial z} \quad (2.18)$$

The frequency domain version of (2.13) is

$$\nabla \cdot \mathbf{u}(\mathbf{r}) = \frac{-j\omega}{\kappa'(\mathbf{r})} p(\mathbf{r}) \quad (2.19)$$

Substituting (2.16), (2.17) and (2.18) into (2.19), we have

$$\frac{\partial}{\partial x} \left(\frac{j}{\omega\rho(\mathbf{r})} \frac{\partial p(\mathbf{r})}{\partial x} \right) + \frac{\partial}{\partial y} \left(\frac{j}{\omega\rho(\mathbf{r})} \frac{\partial p(\mathbf{r})}{\partial y} \right) + \frac{\partial}{\partial z} \left(\frac{j}{\omega\rho(\mathbf{r})} \frac{\partial p(\mathbf{r})}{\partial z} \right) = \frac{-j\omega}{\kappa'(\mathbf{r})} p(\mathbf{r}) \quad (2.20)$$

We can multiply both sides of (2.20) with ω/j . Thus,

$$\frac{\partial}{\partial x} \left(\frac{1}{\rho(\mathbf{r})} \frac{\partial p(\mathbf{r})}{\partial x} \right) + \frac{\partial}{\partial y} \left(\frac{1}{\rho(\mathbf{r})} \frac{\partial p(\mathbf{r})}{\partial y} \right) + \frac{\partial}{\partial z} \left(\frac{1}{\rho(\mathbf{r})} \frac{\partial p(\mathbf{r})}{\partial z} \right) = \frac{-\omega^2}{\kappa'(\mathbf{r})} p(\mathbf{r}) \quad (2.21)$$

$$\begin{aligned} \frac{1}{\rho(\mathbf{r})} \frac{\partial^2 p(\mathbf{r})}{\partial x^2} + \frac{-1}{\rho^2(\mathbf{r})} \frac{\partial \rho(\mathbf{r})}{\partial x} \frac{\partial p(\mathbf{r})}{\partial x} + \frac{1}{\rho(\mathbf{r})} \frac{\partial^2 p(\mathbf{r})}{\partial y^2} + \frac{-1}{\rho^2(\mathbf{r})} \frac{\partial \rho(\mathbf{r})}{\partial y} \frac{\partial p(\mathbf{r})}{\partial y} \\ + \frac{1}{\rho(\mathbf{r})} \frac{\partial^2 p(\mathbf{r})}{\partial z^2} + \frac{-1}{\rho^2(\mathbf{r})} \frac{\partial \rho(\mathbf{r})}{\partial z} \frac{\partial p(\mathbf{r})}{\partial z} = \frac{-\omega^2}{\kappa'(\mathbf{r})} p(\mathbf{r}) \end{aligned} \quad (2.22)$$

Rewriting (2.22), we get

$$\nabla^2 p(\mathbf{r}) - \frac{1}{\rho(\mathbf{r})} \nabla \rho(\mathbf{r}) \cdot \nabla p(\mathbf{r}) + \frac{\omega^2 \rho(\mathbf{r})}{\kappa'(\mathbf{r})} p(\mathbf{r}) = 0 \quad (2.23)$$

Notice that

$$\frac{1}{\rho(r)} \nabla \rho(r) = -\rho(r) \nabla \rho^{-1}(r) \quad (2.24)$$

Substituting (2.24) into (2.23), we have

$$\nabla^2 p(\mathbf{r}) + \rho(\mathbf{r}) \nabla \rho^{-1}(\mathbf{r}) \cdot \nabla p(\mathbf{r}) + \frac{\omega^2 \rho(\mathbf{r})}{\kappa'(\mathbf{r})} p(\mathbf{r}) = 0 \quad (2.25)$$

Instead of using incompressibility, $\kappa'(\mathbf{r})$, we can use compressibility, $\kappa(\mathbf{r})$, which is defined as

$$\kappa(\mathbf{r}) \triangleq \frac{1}{\kappa'(\mathbf{r})} \quad (2.26)$$

Therefore, (2.25) can be rewritten as

$$\nabla^2 p(\mathbf{r}) + \rho(\mathbf{r}) \nabla \rho^{-1}(\mathbf{r}) \cdot \nabla p(\mathbf{r}) + \omega^2 \rho(\mathbf{r}) \kappa(\mathbf{r}) p(\mathbf{r}) = 0 \quad (2.27)$$

The first two terms of (2.27) can be written as

$$\nabla^2 p(\mathbf{r}) + \rho(\mathbf{r}) \nabla \rho^{-1}(\mathbf{r}) \cdot \nabla p(\mathbf{r}) = \rho(\mathbf{r}) \nabla \cdot [\rho^{-1}(\mathbf{r}) \nabla p(\mathbf{r})] \quad (2.28)$$

Thus,

$$\rho(\mathbf{r}) \nabla \cdot [\rho^{-1}(\mathbf{r}) \nabla p(\mathbf{r})] + \omega^2 \rho(\mathbf{r}) \kappa(\mathbf{r}) p(\mathbf{r}) = 0 \quad (2.29)$$

The speed of the sound can be found as [59]

$$c(\mathbf{r}) = \frac{1}{\sqrt{\rho(\mathbf{r}) \kappa(\mathbf{r})}} \quad (2.30)$$

Thus, the lossless wave number in acoustics is defined as

$$k(\mathbf{r}) = \frac{\omega}{c(\mathbf{r})} = \omega \sqrt{\rho(\mathbf{r}) \kappa(\mathbf{r})} \quad (2.31)$$

so

$$k^2(\mathbf{r}) = \omega^2 \rho(\mathbf{r}) \kappa(\mathbf{r}) \quad (2.32)$$

Therefore, the ultrasound wave equation can be written as [15, 53, 60]

$$\rho(\mathbf{r}) \nabla \cdot [\rho^{-1}(\mathbf{r}) \nabla p(\mathbf{r})] + k^2(\mathbf{r}) p(\mathbf{r}) = 0 \quad (2.33)$$

This equation is used to find the scattered field equation as will be explained in section 2.2.

2.2 Scattered Field Equation

The scattered field equation is used in the inverse scattering problem to find the properties of the object of interest. This equation addresses the problem in a general form in the sense that it assumes (1) both compressibility and density profiles can vary, and (2) both the object of interest and background medium may be lossy (having a non-zero attenuation profile).

The attenuation parameter determines the decay of the amplitude of the travelling US signal and it is denoted by α [61, 62]. This parameter has an important role in medical imaging because the attenuation for different tissue types can vary significantly [35, 62, 63]. The effect of the attenuation can be modeled by assuming a complex valued wave number [15, 38, 60].

$$\hat{k}(\mathbf{r}) \triangleq \frac{\omega}{c(\mathbf{r})} - j\alpha(\mathbf{r}) \quad (2.34)$$

where $\hat{k}(\mathbf{r})$ is a complex wave number and $\alpha(\mathbf{r})$ is the attenuation. The minus sign in (2.34) is due to the assumed $e^{+j\omega t}$ time dependency. Similarly the background wave

number, \hat{k}_b , is defined as

$$\hat{k}_b \triangleq \frac{\omega}{c_0} - j\alpha_0 \quad (2.35)$$

where α_0 is the background attenuation. In this thesis, k_0 is used as a background wavenumber without attenuation

$$k_0 = \frac{\omega}{c_0} \quad (2.36)$$

Therefore, the complex background wavenumber can be written as

$$\hat{k}_b = k_0 - j\alpha_0 \quad (2.37)$$

The square of the complex wave number is

$$\begin{aligned} \hat{k}^2(\mathbf{r}) &= \frac{\omega^2}{c^2(\mathbf{r})} - \alpha^2(\mathbf{r}) - j\frac{2\alpha(\mathbf{r})\omega}{c(\mathbf{r})} \\ &= \frac{\omega}{c(\mathbf{r})} \left[\frac{\omega}{c(\mathbf{r})} - \frac{\alpha^2(\mathbf{r})c(\mathbf{r})}{\omega} - j2\alpha \right] \end{aligned} \quad (2.38)$$

The magnitude of the imaginary part of the wavenumber is much less than the magnitude of its real part in most cases [58]. That is, we can make the assumption that

$$\frac{\alpha(\mathbf{r})c(\mathbf{r})}{\omega} \ll 1 \quad (2.39)$$

The derivation of the scattered field equation without using this assumption is provided in Section 2.3. Using (2.39) into (2.38) makes the second term of (2.38) small compared to the other terms and it can therefore be neglected:

$$\hat{k}^2(\mathbf{r}) = \frac{\omega^2}{c^2(\mathbf{r})} - j\frac{2\alpha(\mathbf{r})\omega}{c(\mathbf{r})} \quad (2.40)$$

The same procedure can also be applied for the square of background wave number:

$$\hat{k}_b^2 = \frac{\omega^2}{c_0^2} - j \frac{2\alpha_0\omega}{c_0} \quad (2.41)$$

To find the scattered field equation, two parameters need to be defined. The first parameter, $\delta\rho^{-1}(\mathbf{r})$, is defined as

$$\delta\rho^{-1}(\mathbf{r}) \triangleq \rho^{-1}(\mathbf{r}) - \rho_b^{-1} \quad (2.42)$$

and represents the difference between the inverse density at position \mathbf{r} with the background inverse density. Thus, the inverse density at position \mathbf{r} can be written as

$$\rho^{-1}(\mathbf{r}) = \delta\rho_b^{-1}(\mathbf{r}) + \rho_b^{-1} \quad (2.43)$$

The second parameter, $\delta\kappa(\mathbf{r})$, is defined as

$$\delta\kappa(\mathbf{r}) \triangleq \kappa(\mathbf{r}) - \kappa_b \quad (2.44)$$

and represents the difference between the compressibility at position \mathbf{r} with the background compressibility. Thus, the compressibility at position \mathbf{r} can be written as

$$\kappa(\mathbf{r}) = \delta\kappa(\mathbf{r}) + \kappa_b \quad (2.45)$$

In UT, the background medium plays an important role in the reconstruction of the properties of the object of interest: compressibility and density. The background medium should be chosen to closely match those of the object of interest so that the US waves will better penetrate the object. We say that the scattered fields contain

more information about or better interrogates the object of interest when more energy penetrates the object.

The properties of the object can be related to the background properties by defining contrast variables. The contrast of the compressibility is defined as

$$\chi_1(\mathbf{r}) \triangleq \frac{\kappa(\mathbf{r}) - \kappa_b}{\kappa_b} \quad (2.46)$$

and contrast of inverse density is defined as

$$\chi_2(\mathbf{r}) \triangleq \frac{\rho^{-1}(\mathbf{r}) - \rho_b^{-1}}{\rho_b^{-1}} \quad (2.47)$$

where $\chi_2(\mathbf{r})$ is the contrast of the inverse density, ρ_b^{-1} is the background inverse density and $\rho^{-1}(\mathbf{r})$ is the inverse density at position \mathbf{r} . If the values of $\chi_1(\mathbf{r})$ and $\chi_2(\mathbf{r})$ are known, we can easily find the exact values of compressibility and density because it is assumed that the background properties are known.

Substituting (2.40) into (2.33), we have

$$\rho(\mathbf{r})\nabla \cdot [\rho^{-1}(\mathbf{r})\nabla p(\mathbf{r})] + \left[\frac{\omega^2}{c^2(\mathbf{r})} - j\frac{2\alpha(\mathbf{r})\omega}{c(\mathbf{r})} \right] p(\mathbf{r}) = 0 \quad (2.48)$$

where $p(\mathbf{r})$ is the total pressure field. Using (2.30), we have

$$\rho(\mathbf{r})\nabla \cdot [\rho^{-1}(\mathbf{r})\nabla p(\mathbf{r})] + \omega^2\rho(\mathbf{r})\kappa(\mathbf{r})p(\mathbf{r}) - j2\alpha(\mathbf{r})\omega\sqrt{\rho(\mathbf{r})\kappa(\mathbf{r})}p(\mathbf{r}) = 0 \quad (2.49)$$

Both sides of (2.49) are now multiplied by $\rho^{-1}(\mathbf{r})$, giving

$$\nabla \cdot [\rho^{-1}(\mathbf{r})\nabla p(\mathbf{r})] + \omega^2\kappa(\mathbf{r})p(\mathbf{r}) - j2\alpha(\mathbf{r})\omega\sqrt{\rho^{-1}(\mathbf{r})\kappa(\mathbf{r})}p(\mathbf{r}) = 0 \quad (2.50)$$

Substituting (2.43) and (2.45) into (2.50), we have

$$\begin{aligned} & \nabla \cdot [(\delta\rho^{-1}(\mathbf{r}) + \rho_b^{-1})\nabla p] + \omega^2[\delta\kappa(\mathbf{r}) + \kappa_b]p(\mathbf{r}) \\ & - j2\alpha(\mathbf{r})\omega\sqrt{[\delta\rho^{-1}(\mathbf{r}) + \rho_b^{-1}][\delta\kappa(\mathbf{r}) + \kappa_b]}p(\mathbf{r}) = 0 \end{aligned} \quad (2.51)$$

This can be expanded as

$$\begin{aligned} & \nabla \cdot [\delta\rho^{-1}(\mathbf{r})\nabla p(\mathbf{r})] + \nabla \cdot [\rho_b^{-1}\nabla p(\mathbf{r})] + \omega^2\delta\kappa(\mathbf{r})p(\mathbf{r}) \\ & + \omega^2\kappa_b p(\mathbf{r}) - j2\alpha(\mathbf{r})\omega\sqrt{\frac{\delta\rho^{-1}(\mathbf{r}) + \rho_b^{-1}}{\rho_b^{-1}} \frac{\delta\kappa(\mathbf{r}) + \kappa_b}{\kappa_b}} \rho_b^{-1}\kappa_b p(\mathbf{r}) = 0 \end{aligned} \quad (2.52)$$

Substituting (2.46) and (2.47) into (2.52), we get

$$\begin{aligned} & \nabla \cdot [\delta\rho^{-1}(\mathbf{r})\nabla p(\mathbf{r})] + \nabla \cdot [\rho_b^{-1}\nabla p(\mathbf{r})] + \omega^2\delta\kappa(\mathbf{r})p(\mathbf{r}) \\ & + \omega^2\kappa_b p(\mathbf{r}) - j2\alpha(\mathbf{r})\omega\sqrt{[\chi_2(\mathbf{r}) + 1][\chi_1(\mathbf{r}) + 1]}\rho_b^{-1}\kappa_b p(\mathbf{r}) = 0 \end{aligned} \quad (2.53)$$

Multiplying both sides of (2.53) with ρ_b assumed to be constant, we will have

$$\begin{aligned} & \nabla \cdot \left[\frac{\delta\rho^{-1}(\mathbf{r})}{\rho_b^{-1}} \nabla p(\mathbf{r}) \right] + \rho_b \nabla \cdot [\rho_b^{-1}\nabla p(\mathbf{r})] + \omega^2\rho_b\kappa_b \frac{\delta\kappa(\mathbf{r})}{\kappa_b} p(\mathbf{r}) \\ & + \omega^2\rho_b\kappa_b p(\mathbf{r}) - j2\alpha(\mathbf{r})\omega\sqrt{[\chi_2(\mathbf{r}) + 1][\chi_1(\mathbf{r}) + 1]}\rho_b\kappa_b p(\mathbf{r}) = 0 \end{aligned} \quad (2.54)$$

After some simplifications and applying (2.36), (2.42) and (2.44) into (2.54), we will have

$$\begin{aligned} & \nabla \cdot [\chi_2(\mathbf{r})\nabla p(\mathbf{r})] + \nabla^2 p(\mathbf{r}) + k_0^2\chi_1(\mathbf{r})p(\mathbf{r}) + k_0^2 p(\mathbf{r}) \\ & - j2\alpha(\mathbf{r})\frac{\omega}{c_0}\sqrt{[\chi_1(\mathbf{r}) + 1][\chi_2(\mathbf{r}) + 1]}p(\mathbf{r}) = 0 \end{aligned} \quad (2.55)$$

which can be written as the Helmholtz equation for the pressure with an inhomogeneous right hand side

$$\begin{aligned} \nabla^2 p(\mathbf{r}) + k_0^2 p(\mathbf{r}) &= -k_0^2 \chi_1(\mathbf{r}) p(\mathbf{r}) - \nabla \cdot [\chi_2(\mathbf{r}) \nabla p(\mathbf{r})] \\ &\quad + j2\alpha(\mathbf{r}) k_0 \sqrt{[\chi_1(\mathbf{r}) + 1][\chi_2(\mathbf{r}) + 1]} p(\mathbf{r}) \end{aligned} \quad (2.56)$$

If we add $-j\frac{2\alpha_0\omega}{c_0}p(\mathbf{r})$ to the both sides of (2.56) so as to introduce the attenuation, then we have

$$\begin{aligned} \nabla^2 p(\mathbf{r}) + [k_0^2 - j\frac{2\alpha_0\omega}{c_0}] p(\mathbf{r}) &= -k_0^2 \chi_1(\mathbf{r}) p(\mathbf{r}) - \nabla \cdot [\chi_2(\mathbf{r}) \nabla p(\mathbf{r})] \\ &\quad + j2\alpha(\mathbf{r}) k_0 \sqrt{[\chi_1(\mathbf{r}) + 1][\chi_2(\mathbf{r}) + 1]} p(\mathbf{r}) - j\frac{2\alpha_0\omega}{c_0} p(\mathbf{r}) \end{aligned} \quad (2.57)$$

Substituting (2.36) and (2.41) into (2.57), we have

$$\begin{aligned} \nabla^2 p(\mathbf{r}) + \hat{k}_b^2 p(\mathbf{r}) &= -k_0^2 \chi_1(\mathbf{r}) p(\mathbf{r}) - \nabla \cdot [\chi_2(\mathbf{r}) \nabla p(\mathbf{r})] \\ &\quad + j2\alpha(\mathbf{r}) k_0 \sqrt{[\chi_1(\mathbf{r}) + 1][\chi_2(\mathbf{r}) + 1]} p(\mathbf{r}) \\ &\quad - j2\alpha_0 k_0 p(\mathbf{r}) \end{aligned} \quad (2.58)$$

The contrast values of $\chi_1(\mathbf{r})$ and $\chi_2(\mathbf{r})$ are small in biomedical applications such as breast cancer imaging ($\chi_1 \ll 1$ & $\chi_2 \ll 1$) [7, 14, 64, 65]. Therefore, we can assume that

$$\sqrt{[\chi_1(\mathbf{r}) + 1][\chi_2(\mathbf{r}) + 1]} = \sqrt{\chi_1(\mathbf{r})\chi_2(\mathbf{r}) + \chi_1(\mathbf{r}) + \chi_2(\mathbf{r}) + 1} \simeq 1 \quad (2.59)$$

Substituting this approximation into (2.58), we have

$$\begin{aligned}\nabla^2 p(\mathbf{r}) + \hat{k}_b^2 p(\mathbf{r}) &= -k_0^2 \chi_1(\mathbf{r}) p(\mathbf{r}) - \nabla \cdot [\chi_2(\mathbf{r}) \nabla p(\mathbf{r})] \\ &+ j2\alpha(\mathbf{r}) k_0 p(\mathbf{r}) - j2\alpha_0 k_0 p(\mathbf{r})\end{aligned}\quad (2.60)$$

or

$$\nabla^2 p(\mathbf{r}) + \hat{k}_b^2 p(\mathbf{r}) = -k_0^2 \chi_1(\mathbf{r}) p(\mathbf{r}) - \nabla \cdot [\chi_2(\mathbf{r}) \nabla p(\mathbf{r})] + j2k_0 [\alpha(\mathbf{r}) - \alpha_0] p(\mathbf{r}) \quad (2.61)$$

We define $\delta\alpha(\mathbf{r})$ as

$$\delta\alpha(\mathbf{r}) \triangleq \alpha(\mathbf{r}) - \alpha_0 \quad (2.62)$$

where $\alpha(\mathbf{r})$ is the attenuation at position \mathbf{r} and α_0 is the background attenuation.

Thus, (2.61) can be written as

$$\nabla^2 p(\mathbf{r}) + \hat{k}_b^2 p(\mathbf{r}) = -k_0^2 \chi_1(\mathbf{r}) p(\mathbf{r}) - \nabla \cdot [\chi_2(\mathbf{r}) \nabla p(\mathbf{r})] + j2k_0 \delta\alpha(\mathbf{r}) p(\mathbf{r}) \quad (2.63)$$

We can factor out k_0^2 in (2.63) to get

$$\nabla^2 p(\mathbf{r}) + \hat{k}_b^2 p(\mathbf{r}) = -k_0^2 \left[\chi_1(\mathbf{r}) - j \frac{2\delta\alpha(\mathbf{r})}{k_0} \right] p(\mathbf{r}) - \nabla \cdot [\chi_2(\mathbf{r}) \nabla p(\mathbf{r})] \quad (2.64)$$

Now consider (2.33) for the incident field where there is no object inside the domain.

The background properties are the only properties used in the incident field equation

which can be written as

$$\rho_b \nabla \cdot [\rho_b^{-1} \nabla p^{inc}(\mathbf{r})] + \hat{k}_b^2 p^{inc}(\mathbf{r}) = 0 \quad (2.65)$$

where p^{inc} is the incident pressure (the pressure at the absence of the object of interest). Now assuming that the background density is constant, we have

$$\nabla^2 p^{inc}(\mathbf{r}) + \hat{k}_b^2 p^{inc}(\mathbf{r}) = 0 \quad (2.66)$$

The scattered field equation can be found by subtracting incident field equation (2.66) from total field equation (2.64) and defining $p^{scat} \triangleq p - p^{inc}$:

$$\nabla^2 p^{scat}(\mathbf{r}) + \hat{k}_b^2 p^{scat}(\mathbf{r}) = -k_0^2 [\chi_1(\mathbf{r}) - j \frac{2\delta\alpha(\mathbf{r})}{k_0}] p(\mathbf{r}) - \nabla \cdot [\chi_2(\mathbf{r}) \nabla p(\mathbf{r})] \quad (2.67)$$

where p^{scat} is the scattered pressure. According to the definition of the Green's function for the Helmholtz equation, we have

$$\nabla^2 g(\mathbf{r}, \mathbf{r}') + \hat{k}_b^2 g(\mathbf{r}, \mathbf{r}') = -\delta(\mathbf{r} - \mathbf{r}') \quad (2.68)$$

where \hat{k}_b is the background wavenumber including the background attenuation and $\delta(\cdot)$ is the Dirac delta function. Knowing the Green's function we can formulate the solution of (2.67) as

$$\begin{aligned} p^{scat}(\mathbf{r}) &= k_0^2 \int_V g(\mathbf{r}, \mathbf{r}') [\chi_1(\mathbf{r}') - j \frac{2\delta\alpha(\mathbf{r}')}{k_0}] p(\mathbf{r}') dv' \\ &+ \int_V g(\mathbf{r}, \mathbf{r}') \nabla \cdot [\chi_2(\mathbf{r}') \nabla p(\mathbf{r}')] dv' \end{aligned} \quad (2.69)$$

where, to summarize, k_0 is a background wave number assuming no attenuation, χ_1 is the contrast of compressibility, χ_2 is the contrast of inverse density, $\delta\alpha(\mathbf{r}')$ is the difference between the value of attenuation at position \mathbf{r} and the background attenuation, and $g(\mathbf{r}, \mathbf{r}')$ is the known Green's function. This represents the integral

equation for the scattered pressure field under the approximations (2.39) and (2.59). Note that this equation could represent a way to calculate the scattered pressure field outside of $V = D$, some imaging domain, given χ_1 , χ_2 and $\delta\alpha$ as well as the pressure field inside D . In this case, where $\mathbf{r} \notin V = D$ it would be a Fredholm integral equation of the first kind, nonlinear in $p(\mathbf{r} \in V)$ with each of χ_1 , χ_2 , and $\delta\alpha$.

2.3 General Scattered Field Equation

In the previous section, we assumed that the magnitude of the real part of the wavenumber is much greater than the magnitude of the imaginary part and this led to (2.40) and (2.41) [58]. This assumption is valid for several practical applications including biomedical applications. Therefore, the equation obtained in Section 2.2, (2.69), will be used throughout this thesis. However, in this section, the general formulation without using this assumption will be shown for completeness.

If this assumption is not used, we should substitute the original square of the wavenumber (2.38), into (2.33) giving

$$\rho(\mathbf{r})\nabla \cdot [\rho^{-1}(\mathbf{r})\nabla p(\mathbf{r})] + \left[\frac{\omega^2}{c^2(\mathbf{r})} - \alpha^2(\mathbf{r}) - j\frac{2\alpha(\mathbf{r})\omega}{c(\mathbf{r})} \right] p(\mathbf{r}) = 0 \quad (2.70)$$

Equation (2.70) can be expanded as

$$\rho(\mathbf{r})\nabla \cdot [\rho^{-1}(\mathbf{r})\nabla p(\mathbf{r})] + \omega^2 \rho(\mathbf{r})\kappa(\mathbf{r})p(\mathbf{r}) - \alpha^2(\mathbf{r})p(\mathbf{r}) - j2\alpha(\mathbf{r})\omega\sqrt{\rho(\mathbf{r})\kappa(\mathbf{r})}p(\mathbf{r}) = 0 \quad (2.71)$$

If both sides of (2.71) are multiplied with $\rho^{-1}(\mathbf{r})$, then we have

$$\nabla \cdot [\rho^{-1}(\mathbf{r})\nabla p(\mathbf{r})] + \omega^2 \kappa(\mathbf{r})p(\mathbf{r}) - \frac{\alpha^2(\mathbf{r})}{\rho(\mathbf{r})}p(\mathbf{r}) - j2\alpha(\mathbf{r})\omega\sqrt{\rho^{-1}(\mathbf{r})\kappa(\mathbf{r})}p(\mathbf{r}) = 0 \quad (2.72)$$

Applying (2.43) and (2.45) in (2.72), we will have

$$\begin{aligned} \nabla \cdot [(\delta\rho^{-1}(\mathbf{r}) + \rho_b^{-1})\nabla p(\mathbf{r})] + \omega^2[\delta\kappa(\mathbf{r}) + \kappa_b]p(\mathbf{r}) - \alpha^2(\mathbf{r})[\delta\rho^{-1}(\mathbf{r}) + \rho_b^{-1}]p(\mathbf{r}) \\ - j2\alpha(\mathbf{r})\omega\sqrt{[\delta\rho^{-1}(\mathbf{r}) + \rho_b^{-1}][\delta\kappa(\mathbf{r}) + \kappa_b]}p(\mathbf{r}) = 0 \end{aligned} \quad (2.73)$$

which can be written as

$$\begin{aligned} \nabla \cdot [\delta\rho^{-1}(\mathbf{r})\nabla p(\mathbf{r})] + \nabla \cdot [\rho_b^{-1}\nabla p(\mathbf{r})] + \omega^2\delta\kappa(\mathbf{r})p(\mathbf{r}) + \omega^2\kappa_b p(\mathbf{r}) \\ - \alpha^2(\mathbf{r})\delta\rho^{-1}(\mathbf{r})p(\mathbf{r}) - \alpha^2(\mathbf{r})\rho_b^{-1}p(\mathbf{r}) \\ - j2\alpha(\mathbf{r})\omega\sqrt{[\chi_2(\mathbf{r}) + 1][\chi_1(\mathbf{r}) + 1]}\rho_b^{-1}\kappa_b p(\mathbf{r}) = 0 \end{aligned} \quad (2.74)$$

Multiplying both sides of (2.74) with ρ_b , we have

$$\begin{aligned} \nabla \cdot \left[\frac{\delta\rho^{-1}(\mathbf{r})}{\rho_b^{-1}} \nabla p(\mathbf{r}) \right] + \rho_b \nabla \cdot [\rho_b^{-1}\nabla p(\mathbf{r})] + \omega^2\rho_b\kappa_b \frac{\delta\kappa(\mathbf{r})}{\kappa_b} p(\mathbf{r}) + \omega^2\rho_b\kappa_b p(\mathbf{r}) \\ - \alpha^2(\mathbf{r})\frac{\delta\rho^{-1}(\mathbf{r})}{\rho_b^{-1}} p(\mathbf{r}) - \alpha^2(\mathbf{r})p(\mathbf{r}) \\ - j2\alpha(\mathbf{r})\omega\sqrt{[\chi_2(\mathbf{r}) + 1][\chi_1(\mathbf{r}) + 1]}\rho_b\kappa_b p(\mathbf{r}) = 0 \end{aligned} \quad (2.75)$$

Substituting (2.36), (2.42), (2.44), (2.46) and (2.47) into (2.75), we have

$$\begin{aligned} \nabla \cdot [\chi_2(\mathbf{r})\nabla p(\mathbf{r})] + \nabla^2 p(\mathbf{r}) + k_0^2\chi_1(\mathbf{r})p(\mathbf{r}) + k_0^2 p(\mathbf{r}) \\ - \alpha^2(\mathbf{r})\chi_2(\mathbf{r})p(\mathbf{r}) - \alpha^2(\mathbf{r})p(\mathbf{r}) \\ - j2\alpha(\mathbf{r})\frac{\omega}{c_0}\sqrt{[\chi_1(\mathbf{r}) + 1][\chi_2(\mathbf{r}) + 1]}p(\mathbf{r}) = 0 \end{aligned} \quad (2.76)$$

or

$$\begin{aligned}\nabla^2 p(\mathbf{r}) + k_0^2 p(\mathbf{r}) &= -k_0^2 \chi_1(\mathbf{r}) p(\mathbf{r}) - \nabla \cdot [\chi_2(\mathbf{r}) \nabla p(\mathbf{r})] + \alpha^2(\mathbf{r}) [\chi_2(\mathbf{r}) + 1] p(\mathbf{r}) \\ &+ j2\alpha(\mathbf{r}) k_0 \sqrt{[\chi_1(\mathbf{r}) + 1][\chi_2(\mathbf{r}) + 1]} p(\mathbf{r})\end{aligned}\quad (2.77)$$

If we add $(-\alpha_0^2 - j\frac{2\alpha_0\omega}{c_0})p(\mathbf{r})$ to the both sides of (2.77), we will have

$$\begin{aligned}\nabla^2 p(\mathbf{r}) + [k_0^2 - \alpha_0^2 - j\frac{2\alpha_0\omega}{c_0}] p(\mathbf{r}) &= -k_0^2 \chi_1(\mathbf{r}) p(\mathbf{r}) - \nabla \cdot [\chi_2(\mathbf{r}) \nabla p(\mathbf{r})] \\ &+ j2\alpha(\mathbf{r}) k_0 \sqrt{[\chi_1(\mathbf{r}) + 1][\chi_2(\mathbf{r}) + 1]} p(\mathbf{r}) - j\frac{2\alpha_0\omega}{c_0} p(\mathbf{r}) \\ &- \alpha_0^2 p(\mathbf{r}) + \alpha^2(\mathbf{r}) [\chi_2(\mathbf{r}) + 1] p(\mathbf{r})\end{aligned}\quad (2.78)$$

Again using approximation (2.59) that the values of $\chi_1(\mathbf{r})$ and $\chi_2(\mathbf{r})$ are much smaller than one, we get

$$\begin{aligned}\nabla^2 p(\mathbf{r}) + \hat{k}_b^2 p(\mathbf{r}) &= -k_0^2 \chi_1(\mathbf{r}) p(\mathbf{r}) - \nabla \cdot [\chi_2(\mathbf{r}) \nabla p(\mathbf{r})] + j2k_0 [\alpha(\mathbf{r}) - \alpha_0] p(\mathbf{r}) \\ &+ \left(\alpha^2(\mathbf{r}) [\chi_2(\mathbf{r}) + 1] - \alpha_0^2 \right) p(\mathbf{r})\end{aligned}\quad (2.79)$$

The last term is problematic because it involves $\alpha(\mathbf{r})$, $\chi_2(\mathbf{r})$ and $p(\mathbf{r})$ in a nonlinear fashion. We can deal with this final term by again applying that the contrast of density is small [7, 14, 64, 65], That is

$$\chi_2(\mathbf{r}) \ll 1 \quad \Rightarrow \quad \alpha^2(\mathbf{r}) [\chi_2(\mathbf{r}) + 1] - \alpha_0^2 \simeq \alpha^2(\mathbf{r}) - \alpha_0^2 \quad (2.80)$$

Plugging (2.62) and (2.80) into (2.79) , we have

$$\begin{aligned} \nabla^2 p(\mathbf{r}) + \hat{k}_b^2 p(\mathbf{r}) = & - k_0^2 [\chi_1(\mathbf{r}) - j \frac{2\delta\alpha}{k_0}] p(\mathbf{r}) - \nabla \cdot [\chi_2(\mathbf{r}) \nabla p(\mathbf{r})] \\ & + [\alpha^2(\mathbf{r}) - \alpha_0^2] p(\mathbf{r}) \end{aligned} \quad (2.81)$$

As before, the scattered field equation can be found by subtracting the incident field equation (2.66) from the total field equation (2.81).

$$\begin{aligned} \nabla^2 p^{scat}(\mathbf{r}) + \hat{k}_b^2 p^{scat}(\mathbf{r}) = & - k_0^2 [\chi_1(\mathbf{r}) - j \frac{2\delta\alpha(\mathbf{r})}{k_0}] p(\mathbf{r}) - \nabla \cdot [\chi_2(\mathbf{r}) \nabla p(\mathbf{r})] \\ & + [\alpha^2(\mathbf{r}) - \alpha_0^2] p(\mathbf{r}) \end{aligned} \quad (2.82)$$

Applying the same Green's function technique as before we get

$$\begin{aligned} p^{scat}(\mathbf{r}) = & k_0^2 \int_V g(\mathbf{r}, \mathbf{r}') [\chi_1(\mathbf{r}') - j \frac{2\delta\alpha(\mathbf{r}')}{k_0}] p(\mathbf{r}') dv' \\ & + \int_V g(\mathbf{r}, \mathbf{r}') \nabla \cdot [\chi_2(\mathbf{r}') \nabla p(\mathbf{r}')] dv' \\ & - \int_V g(\mathbf{r}, \mathbf{r}') [\alpha^2(\mathbf{r}') - \alpha_0^2] p(\mathbf{r}') dv' \end{aligned} \quad (2.83)$$

As can be seen by comparing (2.83) to (2.69), when we do not assume that the magnitude of imaginary part of the wave number is much smaller than the magnitude of the real part of the wave number, (2.39), (still assuming that $\chi_1 \ll 1$ and $\chi_2 \ll 1$) then the scattered field integral equation, (2.83), has one more term.

3

Forward Solver

In ultrasound inverse scattering, the goal is to find the compressibility and density profiles of the OI using measurement data which is the scattered pressure information at receiving sites. The so-called inversion algorithms used to find these profiles are iterative. In each iteration of these algorithms, the discrepancy between the measurement and simulated data due to predicted profiles is found, and will be used for updating the predicted profiles. Therefore, we need a solver to find the simulated scattered pressure at the receiving sites due to given profiles. This solver, which is usually called a forward solver, is the topic of this chapter. Using this forward solver, the simulated data can then be compared with the measured data.

The scattered pressure can be found using either (2.69) or (2.83). In this thesis, it is assumed that the magnitude of the imaginary part of the wavenumber is much smaller than the magnitude of the real part of wavenumber [58]. Therefore, (2.69) will be used.

The contrast profiles of the object, as well as the receiver and transmitter positions are known information provided to the forward solver. According to (2.69), to find the scattered pressure at any receiver location due to a predicted profile, the total pressure inside the domain should be found. To this end, r and r' in (2.69) should be both in the region that we have the OI ($r, r' \subset D$). In this case, (2.69) is called domain equation.

In Section 3.1, it will be explained how to find the total pressure inside the domain using the Neumann series along with the limitations of this method. Then, in Section 3.2, an MoM forward solver based on using operator A and its adjoint will be explained. (It will also be shown how to find the adjoint of this operator.) In Section 3.3, some features of the MoM forward solver that was implemented for this thesis will be explained. These features make this MoM forward solver fast and efficient.

3.1 Neumann Series Forward Solver

In this forward solver, a Neumann Series approximation [7] has been used to find the total pressure inside the imaging domain. This forward solver has some limitations: (i) the object (scatterer) should be low contrast [7], and (ii) the size of OI should be small compared to the wavelength of operation.

To explain the Neumann series forward solver, let's start by noting that both χ_1 and χ_2 are real functions in Equation 2.69 (In the discrete form, they will be real vectors.). Inside the first integral in this equation, we have the term $\chi_1(\mathbf{r}') - j\frac{2\delta\alpha(\mathbf{r}')}{k_0}$. For notational simplicity, in the rest of this thesis, this term is denoted by χ_1^c , and will be treated as a complex parameter. (The superscript c denotes that this is a complex parameter.) Thus, the total pressure equation can be written as

$$\begin{aligned}
 p(\mathbf{r}) &= p^{inc}(\mathbf{r}) + k_0^2 \int g(\mathbf{r}, \mathbf{r}') \chi_1^c(\mathbf{r}') p(\mathbf{r}') d\mathbf{r}' \\
 &+ \int g(\mathbf{r}, \mathbf{r}') \nabla \cdot [\chi_2(\mathbf{r}') \nabla p(\mathbf{r}')] d\mathbf{r}'
 \end{aligned} \tag{3.1}$$

and the scattered pressure equation as

$$\begin{aligned} p^{scat}(\mathbf{r}) &= k_0^2 \int g(\mathbf{r}, \mathbf{r}') \chi_1^c(\mathbf{r}') p(\mathbf{r}') d\mathbf{r}' \\ &+ \int g(\mathbf{r}, \mathbf{r}') \nabla \cdot [\chi_2(\mathbf{r}') \nabla p(\mathbf{r}')] d\mathbf{r}' \end{aligned} \quad (3.2)$$

where χ_2 is the contrast of the reciprocal of the density and $g(\mathbf{r}, \mathbf{r}')$ is the Green's function of the background medium. The superscript *scat* and *inc* denote scattered and incident pressure respectively. As noted above, $\chi_1^c(\mathbf{r}')$ is a complex profile that is equal to $\chi_1(\mathbf{r}') - j \frac{2\delta\alpha(\mathbf{r}')}{k_0}$, where χ_1 is the contrast of compressibility, k_0 is the background wavenumber without any attenuation and $\delta\alpha$ is the difference between the attenuation of the object and the attenuation of the background.

Two operators are now defined where both operate on the total pressure inside the domain; namely,

$$\mathcal{G}_1(\cdot) \triangleq k_0^2 \int_D g(\mathbf{r}, \mathbf{r}') \chi_1^c(\mathbf{r}') (\cdot) d\mathbf{r}' \quad \mathbf{r}, \mathbf{r}' \in D \quad (3.3)$$

$$\mathcal{G}_2(\cdot) \triangleq \int_D g(\mathbf{r}, \mathbf{r}') \nabla' \cdot [\chi_2(\mathbf{r}') \nabla' (\cdot)] d\mathbf{r}' \quad \mathbf{r}, \mathbf{r}' \in D \quad (3.4)$$

D is the domain where the object exists. Substituting (3.3) and (3.4) into (3.1), we have

$$p(\mathbf{r}) = p^{inc}(\mathbf{r}) + \mathcal{G}_1\{p(\mathbf{r}')\} + \mathcal{G}_2\{p(\mathbf{r}')\} \quad (3.5)$$

This is an equation for the total pressure inside the domain given the total pressure inside the D . Thus,

$$p(\mathbf{r}) = p^{inc}(\mathbf{r}) + (\mathcal{G}_1 + \mathcal{G}_2)\{p(\mathbf{r}')\} \quad (3.6)$$

Another operator is simply defined as the summation of these two operators:

$$\mathcal{G} \triangleq \mathcal{G}_1 + \mathcal{G}_2 \quad (3.7)$$

Equation 3.6 can be written as

$$(\mathcal{I} - \mathcal{G})\{p(\mathbf{r})\} = p^{inc}(\mathbf{r}) \quad (3.8)$$

where \mathcal{I} is the identity operator. Therefore, total pressure inside the imaging domain can be found as [7]

$$p(\mathbf{r}) = (\mathcal{I} - \mathcal{G})^{-1}\{p^{inc}(\mathbf{r})\} \quad (3.9)$$

If $\|\mathcal{G}\| < 1$, the Neumann series can be applied to (3.9) giving [7, 66, 67]

$$(\mathcal{I} - \mathcal{G})^{-1} = (\mathcal{I} + \mathcal{G} + \mathcal{G}^2 + \dots) \quad (3.10)$$

The total pressure using the Neumann series is thus

$$p(\mathbf{r}) = (\mathcal{I} + \mathcal{G} + \mathcal{G}^2 + \dots)\{p^{inc}(\mathbf{r})\} \quad (3.11)$$

It should be noted that (3.11) can only be used when $\|\mathcal{G}\| < 1$, and it is due to this condition that the OI should be of low contrast and small compared to the operating wavelength. The convergence of the Neumann series, (3.10), is related to the norm of \mathcal{G} : as $\|\mathcal{G}\|$ increases more terms in the series are needed to converge to the solution. It should be noted that if only the first term in (3.11) is utilized, this approximation will be equivalent to the Born approximation [7, 68]. This Neumann series is the basis of the work presented in [7].

3.2 Method of Moments (MoM) Forward Solver

To remove the deficiencies of the Neumann series forward solver which can only be used if the OI is (1) of low contrast, and (2) small compared to the wavelength of operation, we implement an MoM solution of the integral equation. This is required for UT, where we are usually faced with a large object with respect to the operating wavelength (That is, the wavelength in UT applications is very small, on the order of a few millimeters). Therefore, a forward solver that does not have the Neumann series forward solver limitation is needed in UT. An MoM forward solver is proposed to handle this challenge.

The MoM is a general technique to solve linear equations of the form $Ax = b$ where for our case b is the known incident field inside the imaging domain and x is the unknown total pressure inside the imaging domain. The operator A is given as

$$\begin{aligned} A &= \mathcal{I} - \mathcal{G} \\ &= \mathcal{I} - \mathcal{G}_1 - \mathcal{G}_2 \end{aligned} \tag{3.12}$$

To solve this $Ax = b$, the Conjugate Gradient (CG) method will be used and therefore it is crucial to know what adjoint of the operator A and its adjoint, A^a , is. We next explain how to find A^a for this problem. According to the properties of the adjoint operator, we have

$$\begin{aligned} A^a &= (\mathcal{I} - \mathcal{G})^a \\ &= (\mathcal{I} - \mathcal{G}_1 - \mathcal{G}_2)^a \\ &= \mathcal{I} - \mathcal{G}_1^a - \mathcal{G}_2^a \end{aligned} \tag{3.13}$$

Therefore, to find A^a , we only need to know what \mathcal{G}_1^a and \mathcal{G}_2^a are. The adjoint of \mathcal{G}_1 can be found using its definition.

$$\langle \mathcal{G}_1\{p(\mathbf{r}')\}, \psi(\mathbf{r}) \rangle_D = \langle p(\mathbf{r}'), \mathcal{G}_1^a\{\psi(\mathbf{r})\} \rangle_D \quad (3.14)$$

where $\langle \cdot, \cdot \rangle$ is the inner product and the subscript D denotes that this inner product is taken over the domain D . The dummy function $\psi(\mathbf{r})$ is arbitrary over D . It should be noted that the argument inside $\{\}$ is the argument on which the operator operates. According to the definition of the inner product, we will have

$$\int_D \mathcal{G}_1\{p(\mathbf{r}')\} \psi^*(\mathbf{r}) d\mathbf{r} = \int_D p(\mathbf{r}') [\mathcal{G}_1^a\{\psi(\mathbf{r})\}]^* d\mathbf{r}' \quad (3.15)$$

where $*$ denotes the complex conjugate. Inserting the definition of the operator (3.3), into the left side of (3.15), we have

$$I_1 = \int_D k_0^2 \int_D g(\mathbf{r}, \mathbf{r}') \chi_1^c(\mathbf{r}') p(\mathbf{r}') d\mathbf{r}' \psi^*(\mathbf{r}) d\mathbf{r} \quad (3.16)$$

This equation can be written as

$$I_1 = \int_D p(\mathbf{r}') k_0^2 \chi_1^c(\mathbf{r}') \int_D g(\mathbf{r}, \mathbf{r}') \psi^*(\mathbf{r}) d\mathbf{r} d\mathbf{r}' \quad (3.17)$$

Comparing the right hand side of (3.15) with (3.17), we have

$$\left[\mathcal{G}_1^a\{\psi(\mathbf{r})\} \right]^* = k_0^2 \chi_1^c(\mathbf{r}') \int_D g(\mathbf{r}, \mathbf{r}') \psi^*(\mathbf{r}) d\mathbf{r} \quad (3.18)$$

Thus,

$$\mathcal{G}_1^a\{\psi(\mathbf{r})\} = [k_0^2\chi_1^c(\mathbf{r}')]^* \int_D g^*(\mathbf{r}, \mathbf{r}')\psi(\mathbf{r})d\mathbf{r} \quad (3.19)$$

which can also be written as

$$\mathcal{G}_1^a\{\psi(\mathbf{r}')\} = [k_0^2\chi_1^c(\mathbf{r})]^* \int_D g^*(\mathbf{r}', \mathbf{r})\psi(\mathbf{r}')d\mathbf{r}' \quad (3.20)$$

because of the symmetry of g . Therefore, the adjoint of \mathcal{G}_1 will be

$$\mathcal{G}_1^a\{\cdot\} = [k_0^2\chi_1^c(\mathbf{r})]^* \int_D g^*(\mathbf{r}', \mathbf{r})(\cdot)d\mathbf{r}' \quad (3.21)$$

The same procedure is used to find the adjoint of \mathcal{G}_2 . Thus, we start with the definition

$$\langle \mathcal{G}_2\{p(\mathbf{r}')\}, \psi(\mathbf{r}) \rangle_D = \langle p(\mathbf{r}'), \mathcal{G}_2^a\{\psi(\mathbf{r})\} \rangle_D \quad (3.22)$$

and expanding the inner product, we have

$$\int_D \mathcal{G}_2\{p(\mathbf{r}')\}\psi^*(\mathbf{r})d\mathbf{r} = \int_D p(\mathbf{r}')[\mathcal{G}_2^a\{\psi(\mathbf{r})\}]^*d\mathbf{r}' \quad (3.23)$$

Using (3.4) and denoting the LHS of (3.23) by I_2 we have

$$I_2 = \int_D \int_D g(\mathbf{r}, \mathbf{r}')\nabla' \cdot [\chi_2(\mathbf{r}')\nabla'p(\mathbf{r}')]d\mathbf{r}'\psi^*(\mathbf{r})d\mathbf{r} \quad (3.24)$$

We also know that

$$\nabla' \cdot [\chi_2(\mathbf{r}')\nabla'p(\mathbf{r}')] = \chi_2(\mathbf{r}')\nabla'^2p(\mathbf{r}') + \nabla'\chi_2(\mathbf{r}') \cdot \nabla'p(\mathbf{r}') \quad (3.25)$$

which substitutions into (3.24) gives

$$\begin{aligned}
I_2 &= \int_D \int_D g(\mathbf{r}, \mathbf{r}') [\chi_2(\mathbf{r}') \nabla'^2 p(\mathbf{r}') + \nabla' \chi_2(\mathbf{r}') \cdot \nabla' p(\mathbf{r}')] d\mathbf{r}' \psi^*(\mathbf{r}) d\mathbf{r} \\
&= \int_D \int_D g(\mathbf{r}, \mathbf{r}') \chi_2(\mathbf{r}') \nabla'^2 p(\mathbf{r}') d\mathbf{r}' \psi^*(\mathbf{r}) d\mathbf{r} + \int_D \int_D g(\mathbf{r}, \mathbf{r}') \nabla' \chi_2(\mathbf{r}') \cdot \nabla' p(\mathbf{r}') d\mathbf{r}' \psi^*(\mathbf{r}) d\mathbf{r} \\
&= \int_D \left[\int_D g(\mathbf{r}, \mathbf{r}') \psi^*(\mathbf{r}) d\mathbf{r} \right] \chi_2(\mathbf{r}') \nabla'^2 p(\mathbf{r}') d\mathbf{r}' + \int_D \left[\int_D g(\mathbf{r}, \mathbf{r}') \psi^*(\mathbf{r}) d\mathbf{r} \right] \nabla' \chi_2(\mathbf{r}') \cdot \nabla' p(\mathbf{r}') d\mathbf{r}'
\end{aligned} \tag{3.26}$$

For the simplicity in writing, we define $F(\mathbf{r}')$ as

$$F(\mathbf{r}') \triangleq \int_D g(\mathbf{r}, \mathbf{r}') \psi^*(\mathbf{r}) d\mathbf{r} \tag{3.27}$$

Substituting (3.27) into (3.26), we have

$$I_2 = \int_D F(\mathbf{r}') \chi_2(\mathbf{r}') \nabla'^2 p(\mathbf{r}') d\mathbf{r}' + \int_D F(\mathbf{r}') \nabla' \chi_2(\mathbf{r}') \cdot \nabla' p(\mathbf{r}') d\mathbf{r}' \tag{3.28}$$

We call the first and second terms of (3.28) C_1 and C_2 respectively. We also have

$$\nabla' [F(\mathbf{r}') \chi_2(\mathbf{r}')] = \chi_2(\mathbf{r}') \nabla' F(\mathbf{r}') + F(\mathbf{r}') \nabla' \chi_2(\mathbf{r}') \tag{3.29}$$

Substituting (3.29) into C_2 , we have

$$\begin{aligned}
C_2 &= \int_D F(\mathbf{r}') \nabla' \chi_2(\mathbf{r}') \cdot \nabla' p(\mathbf{r}') d\mathbf{r}' \\
&= \int_D [\nabla' [F(\mathbf{r}') \chi_2(\mathbf{r}')] - \chi_2(\mathbf{r}') \nabla' F(\mathbf{r}')] \cdot \nabla' p(\mathbf{r}') d\mathbf{r}' \\
&= \int_D \nabla' [F(\mathbf{r}') \chi_2(\mathbf{r}')] \cdot \nabla' p(\mathbf{r}') d\mathbf{r}' - \int_D \chi_2(\mathbf{r}') \nabla' F(\mathbf{r}') \cdot \nabla' p(\mathbf{r}') d\mathbf{r}' \tag{3.30}
\end{aligned}$$

We call the first and second terms of the (3.30) D_1 and D_2 , respectively. D_1 is thus

$$\begin{aligned}
D_1 &= \int_D \nabla' [F(\mathbf{r}') \chi_2(\mathbf{r}')] \cdot \nabla' p(\mathbf{r}') d\mathbf{r}' \\
&= \int_D (\nabla' \cdot [F(\mathbf{r}') \chi_2(\mathbf{r}') \nabla' p(\mathbf{r}')] - F(\mathbf{r}') \chi_2(\mathbf{r}') \nabla'^2 p(\mathbf{r}')) d\mathbf{r}' \\
&= \int_D \nabla' \cdot [F(\mathbf{r}') \chi_2(\mathbf{r}') \nabla' p(\mathbf{r}')] d\mathbf{r}' - \int_D F(\mathbf{r}') \chi_2(\mathbf{r}') \nabla'^2 p(\mathbf{r}') d\mathbf{r}' \\
&= \int_{\partial D} F(\mathbf{r}') \chi_2(\mathbf{r}') \nabla' p(\mathbf{r}') d\Gamma - \int_D F(\mathbf{r}') \chi_2(\mathbf{r}') \nabla'^2 p(\mathbf{r}') d\mathbf{r}' \quad (3.31)
\end{aligned}$$

where ∂D represents the integral over the boundary. Therefore, if we assume that the contrast of inverse density (χ_2) is zero on the boundary, then the first part of (3.31) becomes zero. The second part of (3.31) will be canceled with C_1 . Therefore, I_2 will be

$$\begin{aligned}
I_2 &= D_2 \\
&= - \int_D \chi_2(\mathbf{r}') \nabla' p(\mathbf{r}') \cdot \nabla' F(\mathbf{r}') d\mathbf{r}' \\
&= - \int_D \chi_2(\mathbf{r}') [\nabla' \cdot (p(\mathbf{r}') \nabla' F(\mathbf{r}')) - p(\mathbf{r}') \nabla'^2 F(\mathbf{r}')] d\mathbf{r}' \\
&= - \int_D \chi_2(\mathbf{r}') \nabla' \cdot [p(\mathbf{r}') \nabla' F(\mathbf{r}')] d\mathbf{r}' + \int_D p(\mathbf{r}') \chi_2(\mathbf{r}') \nabla'^2 F(\mathbf{r}') d\mathbf{r}' \quad (3.32)
\end{aligned}$$

We call the first and second terms of (3.32) E_1 and E_2 , respectively. If we apply the

divergence theorem to E_1 , we will have

$$\begin{aligned}
E_1 &= - \int_D \chi_2(\mathbf{r}') \nabla' \cdot [p(\mathbf{r}') \nabla' F(\mathbf{r}')] d\mathbf{r}' \\
&= - \int_D \left[\nabla' \cdot [\chi_2(\mathbf{r}') p(\mathbf{r}') \nabla' F(\mathbf{r}')] - \nabla' \chi_2(\mathbf{r}') \cdot p(\mathbf{r}') \nabla' F(\mathbf{r}') \right] d\mathbf{r}' \\
&= - \int_D \nabla' \cdot [\chi_2(\mathbf{r}') p(\mathbf{r}') \nabla' F(\mathbf{r}')] d\mathbf{r}' + \int_D \nabla' \chi_2(\mathbf{r}') \cdot p(\mathbf{r}') \nabla' F(\mathbf{r}') d\mathbf{r}' \\
&= - \int_{\partial D} \chi_2(\mathbf{r}') p(\mathbf{r}') \nabla' F(\mathbf{r}') d\Gamma + \int_D \nabla' \chi_2(\mathbf{r}') \cdot p(\mathbf{r}') \nabla' F(\mathbf{r}') d\mathbf{r}' \quad (3.33)
\end{aligned}$$

If we assume that χ_2 is zero on the boundary, it makes the first part of (3.33) zero.

Thus,

$$E_1 = \int_D p(\mathbf{r}') \nabla' \chi_2(\mathbf{r}') \cdot \nabla' F(\mathbf{r}') d\mathbf{r}' \quad (3.34)$$

Finally I_2 can be found as

$$\begin{aligned}
I_2 &= E_1 + E_2 \\
&= \int_D p(\mathbf{r}') \nabla' \chi_2(\mathbf{r}') \cdot \nabla' F(\mathbf{r}') d\mathbf{r}' + \int_D p(\mathbf{r}') \chi_2(\mathbf{r}') \nabla'^2 F(\mathbf{r}') d\mathbf{r}' \\
&= \int_D p(\mathbf{r}') [\nabla' \chi_2(\mathbf{r}') \cdot \nabla' F(\mathbf{r}') + \chi_2(\mathbf{r}') \nabla'^2 F(\mathbf{r}')] d\mathbf{r}' \quad (3.35)
\end{aligned}$$

Comparing (3.23) with the right hand side of (3.35), we have

$$\left[\mathcal{G}_2^a \{ \psi(\mathbf{r}') \} \right]^* = \nabla' \chi_2(\mathbf{r}') \cdot \nabla' F(\mathbf{r}') + \chi_2(\mathbf{r}') \nabla'^2 F(\mathbf{r}') \quad (3.36)$$

We can also change the variable. Thus,

$$\left[\mathcal{G}_2^a \{ \psi(\mathbf{r}') \} \right]^* = \nabla \chi_2(\mathbf{r}) \cdot \nabla F(\mathbf{r}) + \chi_2(\mathbf{r}) \nabla^2 F(\mathbf{r}) \quad (3.37)$$

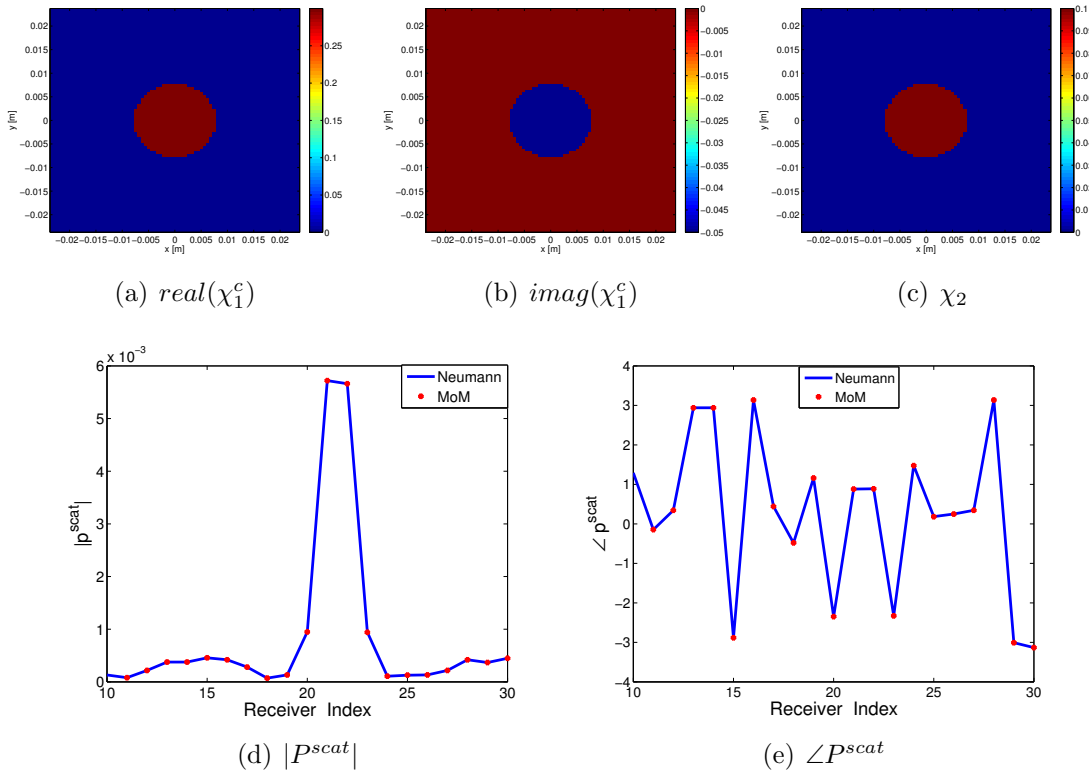


Figure 3.1: Comparison between the calculated scattered pressure using the Neumann series and MoM forward solver. (a) the real part of χ_1^c of the OI. (b) The imaginary part of χ_1^c of the OI. (c) Contrast of inverse density, χ_2 , of the OI. (d) Comparing the magnitude of the scattered pressure at receiver positions using Neumann and MoM forward solver. (e) Comparing the phase of scattered pressure at receiver positions using Neumann and MoM forward solver.

Substituting (3.27) into (3.37), we have

$$\begin{aligned} \left[\mathcal{G}_2^a \{ \psi(\mathbf{r}') \} \right]^* &= \nabla \chi_2(\mathbf{r}) \cdot \nabla \int g(\mathbf{r}', \mathbf{r}) \psi^*(\mathbf{r}') d\mathbf{r}' \\ &+ \chi_2(\mathbf{r}) \nabla^2 \int_D g(\mathbf{r}', \mathbf{r}) \psi^*(\mathbf{r}') d\mathbf{r}' \end{aligned} \quad (3.38)$$

When \mathcal{G}_2^a operates on the $\psi(\mathbf{r}')$, we have

$$\mathcal{G}_2^a \{ \psi(\mathbf{r}') \} = \nabla \chi_2^*(\mathbf{r}) \cdot \nabla \int g^*(\mathbf{r}', \mathbf{r}) \psi(\mathbf{r}') d\mathbf{r}' + \chi_2^*(\mathbf{r}) \nabla^2 \int g^*(\mathbf{r}', \mathbf{r}) \psi(\mathbf{r}') d\mathbf{r}' \quad (3.39)$$

Thus, the adjoint operator \mathcal{G}_2^a is written

$$\mathcal{G}_2^a \{ \cdot \} = \nabla \chi_2^*(\mathbf{r}) \cdot \nabla \int g^*(\mathbf{r}', \mathbf{r}) (\cdot) d\mathbf{r}' + \chi_2^*(\mathbf{r}) \nabla^2 \int g^*(\mathbf{r}', \mathbf{r}) (\cdot) d\mathbf{r}' \quad (3.40)$$

The adjoint operator of A that is mentioned in (3.13) can be found using (3.21) and (3.40). It should be noted that the only assumption used to find the adjoint operator is that the contrast of the reciprocal of the density is zero on the boundary. This assumption is true in practice. With the OI surrounded by the background medium, the contrast is zero on the boundary.

The way that the imaging domain and contrast profiles are discretized is explained in Appendix A. In this Appendix, we also explain how to handle the singularity in the domain equation. The Conjugate Gradient (CG) algorithm which is required in MoM forward solver is explained in Appendix B.

The comparison between the magnitude and phase of scattered pressure at receiver positions using the Neumann series and MoM forward solver for a cylinder object which has $\chi_1^c = 0.3 - j0.05$ and $\chi_2 = 0.1$ is shown in Figure 3.1.

3.3 MoM Features

The MoM forward solver that was implemented for this thesis has some features that make it fast and efficient. These features are

- The use of the marching-on-in-source technique.
- The use of the Toeplitz Block Matrix for the memory storage.
- The use of the fast Fourier transform (FFT) for matrix-vector multiplications.

These features are now explained in more details.

3.3.1 Marching-on-in-source technique

One of the methods used in this thesis to accelerate the MoM forward solver is the marching-on-in-source method. As explained above, our MoM forward solver uses the CG method to solve the associated $Ax = b$ problem where x is the unknown total pressure in the imaging domain. One of the inputs to the CG algorithm is an initial guess for the unknown total field pressure. This initial guess is usually chosen to be either the incident pressure inside the imaging domain or zero. The choice of the initial guess plays a very important role in the number of CG iterations needed for the convergence. That is, if we have a good choice for the initial guess (close to the actual value of the total pressure inside the imaging domain), a much fewer number of CG iterations will be needed. As a result, much less matrix-vector multiplications will be performed; thus, having a much faster forward solver.

Herein, we have implemented the marching-on-in-source technique to provide a good initial guess for the CG algorithm. This technique was originally developed for the electromagnetic forward scattering problem [69], and here we apply this method

to the ultrasound forward scattering problem. The idea behind this technique is that if we have a couple of transmitters close to each other, and we know the total pressure due to a few of them, we can somehow predict what the total pressure due to an adjacent transmitter will be. This is due to the fact that if the transmitters are close to each other, the total pressure inside the domain due to these transmitters should be close to each other.

When using the marching-on-in-source technique in conjunction with the CG-MoM forward solver, we first find the total pressure due to a few transmitters, say 3 of them, using a standard initial guess, *e.g.*, zero. We then use these calculated total pressures to find a good initial guess for the forward scattering problem corresponding to the next transmitter. In the next step, we can use this recently-calculated total pressure with previously-calculated total pressures to find a good initial guess for the forward scattering problem corresponding to the next transmitter. This procedure continues until we solve all the forward scattering problems.

Now, let's explain this method in the mathematical framework. Assume that we want to find a good initial guess for the forward scattering problem corresponding to the m^{th} transmitter. This good initial guess can be written as a linear combination of the previously-found total pressures due to Q previous transmitters. Denoting the initial guess corresponding to the m^{th} transmitter by x_m^0 , and the total pressure corresponding to the $(m - q)^{\text{th}}$ by x_{m-q} , the initial guess can then be found as

$$x_m^0 = \sum_{q=1}^Q a_q x_{m-q} \quad (3.41)$$

where a_q is the weighting coefficient for the total pressure inside the domain due to the transmitter $m - q$. These weighting coefficients are unknown. If we can find these

unknown coefficients, we will then have our initial guess. To find these coefficients, it should be noted that a good initial guess should be close to the exact solution. In other words, it should minimize the following norm

$$\operatorname{argmin}_{x_m^0} \{ \|Ax_m^0 - b\|^2 \} \quad (3.42)$$

where $\|\cdot\|$ is denoted as the norm. Substituting (3.41) into (3.42), we have

$$\operatorname{argmin}_{a_q} \left\{ \left\| A \sum_{q=1}^Q a_q x_{m-q} - b \right\|^2 \right\} \quad (3.43)$$

The above minimization can be written as

$$\operatorname{argmin}_{a_q} \left\{ \left\| \sum_{q=1}^Q a_q Ax_{m-q} - b \right\|^2 \right\} \quad (3.44)$$

where A is the operator that operates on the total pressure inside the domain, x_{m-q} is the total field due to the transmitter $m - q$ and b is the incident field due to the transmitter m . It should be noted that when A operates on x_{m-q} , it gives the incident pressure inside the domain due to transmitter $m - q$. Thus, (3.44) can be written as

$$\operatorname{argmin}_{a_q} \left\{ \left\| \sum_{q=1}^N a_q p_{m-q}^{inc} - p_m^{inc} \right\|^2 \right\} \quad (3.45)$$

where p_{m-q}^{inc} is the incident pressure inside the domain due to the transmitter $m - q$. In our implementation, p_{m-q}^{inc} is a column vector whose size is equal to the number of discretizing pulses, N , within the imaging domain. Now, we can write the above

minimization in the following form:

$$\operatorname{argmin}_{a_q} \left\{ \left\| \begin{pmatrix} p_{m-1}^{inc} & p_{m-2}^{inc} & \cdots & p_{m-Q}^{inc} \end{pmatrix} \begin{pmatrix} a_1 \\ a_2 \\ \vdots \\ a_Q \end{pmatrix} - p_m^{inc} \right\|^2 \right\} \quad (3.46)$$

where $\begin{pmatrix} p_{m-1}^{inc} & p_{m-2}^{inc} & \cdots & p_{m-Q}^{inc} \end{pmatrix}$ is an $N \times Q$ matrix. This norm minimization is equivalent to solving the following linear algebra equation:

$$\begin{pmatrix} p_{m-1}^{inc} & p_{m-2}^{inc} & \cdots & p_{m-Q}^{inc} \end{pmatrix} \begin{pmatrix} a_1 \\ a_2 \\ \vdots \\ a_Q \end{pmatrix} = p_m^{inc} \quad (3.47)$$

Multiplying both sides of (3.47) with the Hermitian of the first term, we will have

$$\begin{aligned} & \begin{pmatrix} p_{m-1}^{inc} & p_{m-2}^{inc} & \cdots & p_{m-Q}^{inc} \end{pmatrix}^H \begin{pmatrix} p_{m-1}^{inc} & p_{m-2}^{inc} & \cdots & p_{m-Q}^{inc} \end{pmatrix} \begin{pmatrix} a_1 \\ a_2 \\ \vdots \\ a_Q \end{pmatrix} \\ & = \begin{pmatrix} p_{m-1}^{inc} & p_{m-2}^{inc} & \cdots & p_{m-Q}^{inc} \end{pmatrix}^H p_m^{inc} \end{aligned} \quad (3.48)$$

Therefore, these coefficients can be found as

$$\begin{pmatrix} a_1 \\ a_2 \\ \vdots \\ a_Q \end{pmatrix} = \left[\begin{pmatrix} p_{m-1}^{inc} & p_{m-2}^{inc} & \cdots & p_{m-Q}^{inc} \end{pmatrix}^H \begin{pmatrix} p_{m-1}^{inc} & p_{m-2}^{inc} & \cdots & p_{m-Q}^{inc} \end{pmatrix} \right]^{-1} \begin{pmatrix} p_{m-1}^{inc} & p_{m-2}^{inc} & \cdots & p_{m-Q}^{inc} \end{pmatrix}^H p_m^{inc} \quad (3.49)$$

Note that the size of the matrix for which we need to find the inverse according to the above equation is $Q \times Q$. As noted above, we may use the previous $Q = 3$ transmitters to find a good initial guess for the next transmitter. In this situation, the size of the matrix will be 3×3 . Therefore, finding the inverse matrix is very quick. Also, the matrix itself only depends on the incident pressures, which means that the matrix itself can be precomputed and stored. Finally, having these coefficients, we can find a good initial guess for each of our transmitters.

3.3.2 Toeplitz Block Matrix

To understand the Toeplitz block matrix, we first describe a Toeplitz matrix. A Toeplitz matrix is a matrix whose diagonals are constant [70]. In our particular case,

a symmetric Toeplitz matrix such as the following form is needed.

$$\begin{pmatrix} \boxed{\text{p}} & \boxed{\text{e}} & \boxed{\text{d}} & \boxed{\text{r}} & \boxed{\text{a}} & \boxed{\text{m}} \\ \boxed{\text{e}} & \boxed{\text{p}} & \boxed{\text{e}} & \boxed{\text{d}} & \boxed{\text{r}} & \boxed{\text{a}} \\ \boxed{\text{d}} & \boxed{\text{e}} & \boxed{\text{p}} & \boxed{\text{e}} & \boxed{\text{d}} & \boxed{\text{r}} \\ \boxed{\text{r}} & \boxed{\text{d}} & \boxed{\text{e}} & \boxed{\text{p}} & \boxed{\text{e}} & \boxed{\text{d}} \\ \boxed{\text{a}} & \boxed{\text{r}} & \boxed{\text{d}} & \boxed{\text{e}} & \boxed{\text{p}} & \boxed{\text{e}} \\ \boxed{\text{m}} & \boxed{\text{a}} & \boxed{\text{r}} & \boxed{\text{d}} & \boxed{\text{e}} & \boxed{\text{p}} \end{pmatrix}$$

Now, let's focus on our UT forward scattering problem. From (3.2) the following term is common in both integrals:

$$\int g(\mathbf{r}, \mathbf{r}') d\mathbf{r}' \quad (3.50)$$

This provides us with a hint as to how we might be able to take advantage of the Toeplitz matrix properties in our numerical implementation. Before discussing this further, let's remind ourselves that we are dealing with a 2D time-harmonic problem with $e^{+j\omega t}$ time-dependency. Thus,

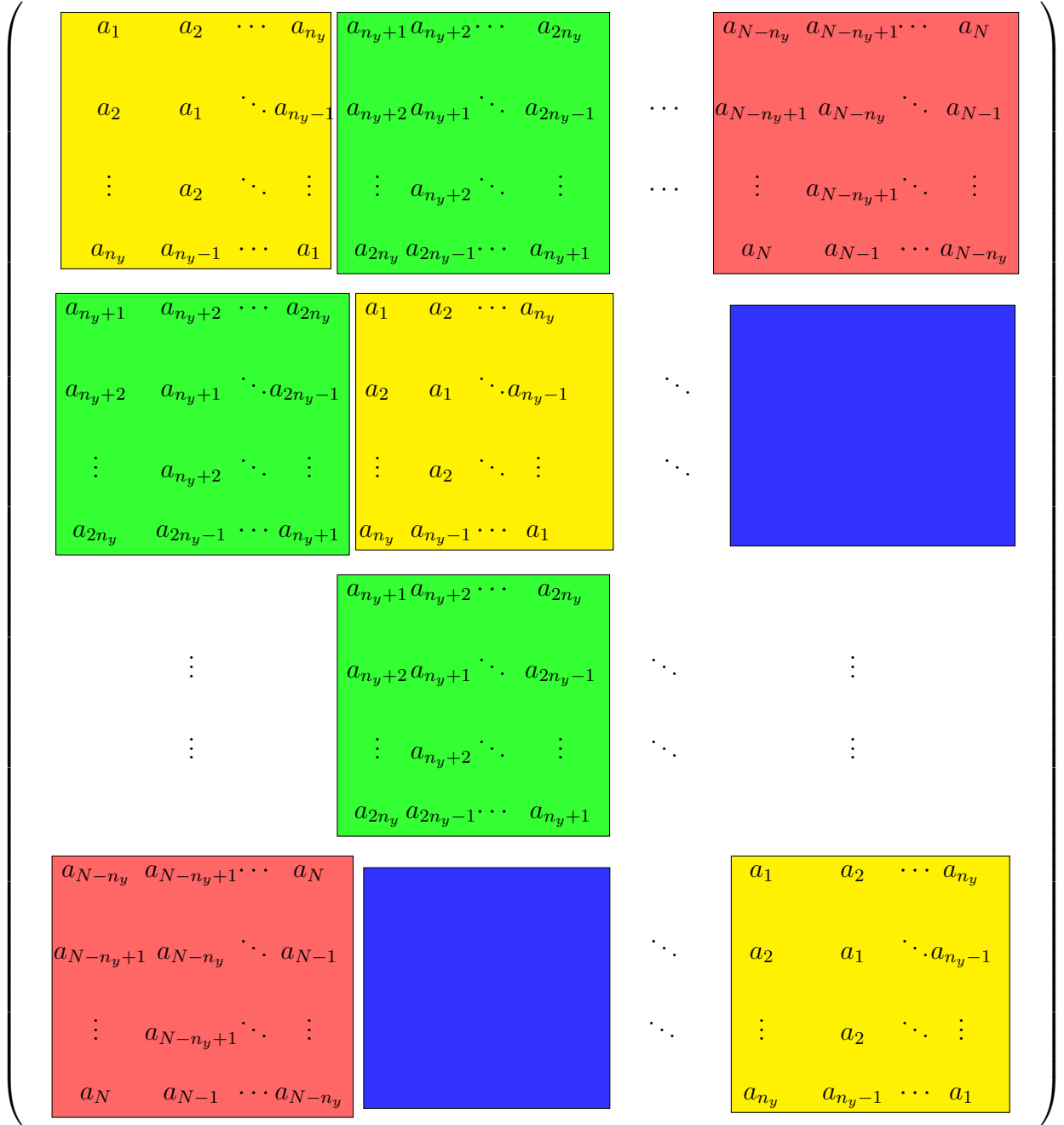
$$g(\mathbf{r}, \mathbf{r}') = \frac{1}{4j} H_0^{(2)}(k_0 |\mathbf{r} - \mathbf{r}'|) \quad (3.51)$$

where k_0 is the background wavenumber neglecting attenuation and $H_0^{(2)}$ is the zeroth-order Hankel function of the second kind. To find the total pressure inside the imaging domain, we should use the domain equation for which $\mathbf{r}, \mathbf{r}' \in D$. In this case, if we discretize the imaging domain, the size of $\int g(\mathbf{r}, \mathbf{r}') d\mathbf{r}'$ will be $N \times N$ where N is the

total number of the pixels in the domain, that is

$$N = n_x \times n_y \tag{3.52}$$

and n_x and n_y are the number of pixels in the x and y directions respectively. As can be seen in (3.51), the Green's function depends only on the distance between the source and observation points inside the domain. Therefore, if we discretize $\int g(\mathbf{r}, \mathbf{r}') d\mathbf{r}'$, we have the following $N \times N$ matrix.



As can be seen, this matrix consists of blocks; each of which is a Toeplitz matrix. The size of each Toeplitz matrix is $n_y \times n_y$ and the total number of Toeplitz blocks is $n_x \times n_x$. If we think about each of these Toeplitz blocks as one element, then they

make a large Toeplitz matrix. For example, if we assume that $n_x = 5$, then we have 25 Toeplitz blocks. These blocks will then make a block Toeplitz matrix that is shown below.

$$\begin{pmatrix} \text{yellow} & \text{red} & \text{blue} & \text{orange} & \text{green} \\ \text{red} & \text{yellow} & \text{red} & \text{blue} & \text{orange} \\ \text{blue} & \text{red} & \text{yellow} & \text{red} & \text{blue} \\ \text{orange} & \text{blue} & \text{red} & \text{yellow} & \text{red} \\ \text{green} & \text{orange} & \text{blue} & \text{red} & \text{yellow} \end{pmatrix}$$

Now, let's look at this matrix carefully. It can be easily seen that if we only know the first row of this matrix, we can find the rest of its elements. Implementing this into the algorithm will make it very efficient in terms of memory storage. This is due to the fact that we only need to find and store N elements of this matrix instead of N^2 elements. This will be especially useful for the large domain problems considered herein.

3.3.3 Fast Fourier Transform (FFT) Multiplication

The other technique implemented in the forward solver of this thesis to make the CG-MoM forward solver faster, is the use of the fast Fourier transform (FFT) for the matrix-vector multiplication. This is important because standard matrix-vector multiplication has a computational complexity of the order of $\mathcal{O}(n^2)$ whereas the computational complexity of FFT-accelerated matrix-vector multiplication is $\mathcal{O}(n \log(n))$.

It is well-known that matrix-vector multiplication can be accelerated by the FFT if the matrix is circulant. A circulant matrix is a Toeplitz matrix where each row is

shifted with respect to the previous row [71]. For example, the following matrix is a circulant matrix:

$$\begin{pmatrix} \boxed{M} & \boxed{O} & \boxed{J} & \boxed{A} & \boxed{B} & \boxed{I} \\ \boxed{I} & \boxed{M} & \boxed{O} & \boxed{J} & \boxed{A} & \boxed{B} \\ \boxed{B} & \boxed{I} & \boxed{M} & \boxed{O} & \boxed{J} & \boxed{A} \\ \boxed{A} & \boxed{B} & \boxed{I} & \boxed{M} & \boxed{O} & \boxed{J} \\ \boxed{J} & \boxed{A} & \boxed{B} & \boxed{I} & \boxed{M} & \boxed{O} \\ \boxed{O} & \boxed{J} & \boxed{A} & \boxed{B} & \boxed{I} & \boxed{M} \end{pmatrix}$$

Circulant matrix-vector multiplication can be performed using FFT multiplication:

$$\begin{pmatrix} m_0 & m_1 & \cdots & m_{p-1} & m_p \\ m_p & m_0 & \cdots & m_{p-2} & m_{p-1} \\ \vdots & m_p & m_0 & \cdots & \vdots \\ m_2 & \cdots & m_p & \cdots & m_1 \\ m_1 & m_2 & \cdots & m_p & m_0 \end{pmatrix} \begin{pmatrix} n_0 \\ n_1 \\ n_2 \\ \vdots \\ n_p \end{pmatrix} = \text{ifft} \left[\text{fft}[M(1, :)] \text{fft}[N(:, 1)] \right] \quad (3.53)$$

where M is the above circulant matrix and N is the above column vector. ifft and fft are the inverse fast Fourier transform and fast Fourier transform, respectively. $M(1, :)$ is the first row of the circulant matrix and $N(:, 1)$ is the column vector that should be multiplied with a circulant matrix. Therefore, if we only know the first row of a circulant matrix, we can find the results of a circulant matrix-vector multiplication.

This method can be applied to the Toeplitz block matrix method mentioned in Section 3.3.2. In this case, the $N \times N$ matrix which is a large block Toeplitz matrix

is to multiply an $N \times 1$ vector. In this section, the goal is to show how to use only the first row of the $N \times N$ Toeplitz block matrix to multiply an $N \times 1$ vector using FFT multiplication. As mentioned in Section 3.3.2, the first row of the $N \times N$ matrix corresponds to the first rows of n_x Toeplitz blocks where the size of the first row of each Toeplitz block is $1 \times n_y$. To use the FFT multiplication, each Toeplitz block matrix should be converted to a circulant matrix.

Conversion of a Toeplitz Matrix to a Circulant Matrix:

Being a Toeplitz matrix, a circulant matrix will have constant diagonals. To convert a Toeplitz matrix into a circulant matrix [72], some columns should be added to the Toeplitz matrix. For example, if we have the following $n_y \times n_y$ Toeplitz matrix,

$$\begin{pmatrix} a_1 & a_2 & \cdots & a_{n_y-1} & a_{n_y} \\ a_2 & a_1 & a_2 & & a_{n_y-1} \\ \vdots & a_2 & a_1 & \ddots & \vdots \\ a_{n_y-1} & & \ddots & \ddots & a_2 \\ a_{n_y} & a_{n_y-1} & \cdots & a_2 & a_1 \end{pmatrix}$$

we should add $n_y - 2$ columns to convert it to a circulant matrix. The size of the obtained circulant matrix will be $n_y \times (2n_y - 2)$. The elements which are added to the first row of a Toeplitz matrix are $(a_{n_y-1} \ a_{n_y-2} \ \cdots \ a_3 \ a_2)$. The other elements of the circulant matrix can be found using the first row of the circulant matrix as shown

below:

$$\left(\begin{array}{ccccc|ccccc} a_1 & a_2 & \cdots & a_{n_y-1} & a_{n_y} & a_{n_y-1} & a_{n_y-2} & \cdots & a_3 & a_2 \\ a_2 & a_1 & a_2 & & a_{n_y-1} & a_{n_y} & a_{n_y-1} & & a_4 & a_3 \\ \vdots & a_2 & a_1 & \ddots & \ddots & \ddots & a_{n_y} & a_{n_y-1} & \ddots & \vdots \\ a_{n_y-1} & & \ddots & \ddots & a_2 & a_3 & & \ddots & \ddots & a_{n_y} \\ a_{n_y} & a_{n_y-1} & \cdots & a_2 & a_1 & a_2 & a_3 & \cdots & a_{n_y-2} & a_{n_y-1} \end{array} \right)$$

Here the yellow box is a Toeplitz matrix and the green box is added to a Toeplitz matrix to make it a circulant matrix. It should be noted that an $n_y \times n_y$ Toeplitz matrix should multiply an $n_y \times 1$ vector. Therefore, when a Toeplitz matrix is converted into a circulant matrix, some elements should be added to the vector which will be multiplied by the circulant matrix. This is due to the fact that the size of the new circulant matrix is $n_y \times (2n_y - 2)$. Thus, the size of the vector which is multiplied with this matrix should be $(2n_y - 2) \times 1$. The elements which are added to a column vector are denoted by $c_1, c_2, \dots, c_{n_y-2}$. The advantage is that now instead of using a Toeplitz matrix-vector multiplication, we can use a circulant matrix vector

multiplication. The results of both matrix-vector multiplications are shown below:

$$\begin{pmatrix}
 \begin{array}{ccccc}
 a_1 & a_2 & \cdots & a_{n_y-1} & a_{n_y} \\
 a_2 & a_1 & a_2 & & a_{n_y-1} \\
 \vdots & a_2 & a_1 & \ddots & \ddots \\
 a_{n_y-1} & & \ddots & \ddots & a_2 \\
 a_{n_y} & a_{n_y-1} & \cdots & a_2 & a_1
 \end{array} &
 \begin{array}{ccccc}
 a_{n_y-1} & a_{n_y-2} & \cdots & a_3 & a_2 \\
 a_{n_y} & a_{n_y-1} & & a_4 & a_3 \\
 \ddots & a_{n_y} & a_{n_y-1} & \ddots & \vdots \\
 a_3 & & \ddots & \ddots & a_{n_y} \\
 a_2 & a_3 & \cdots & a_{n_y-2} & a_{n_y-1}
 \end{array}
 \end{pmatrix}
 \begin{pmatrix}
 b_1 \\
 b_2 \\
 \vdots \\
 b_{n_y-1} \\
 b_{n_y} \\
 c_1 \\
 c_2 \\
 \vdots \\
 c_{n_y-2}
 \end{pmatrix}
 =
 \begin{pmatrix}
 \begin{array}{ccccc}
 a_1 & a_2 & \cdots & a_{n_y-1} & a_{n_y} \\
 a_2 & a_1 & a_2 & & a_{n_y-1} \\
 \vdots & a_2 & a_1 & \ddots & \vdots \\
 a_{n_y-1} & & \ddots & \ddots & a_2 \\
 a_{n_y} & a_{n_y-1} & \cdots & a_2 & a_1
 \end{array}
 \end{pmatrix}
 \begin{pmatrix}
 b_1 \\
 b_2 \\
 \vdots \\
 b_{n_y-1} \\
 b_{n_y}
 \end{pmatrix}$$

It can be concluded that the value of $c_1, c_2, \dots, c_{n_y-2}$ should be set to zero to have the same results for both matrix-vector multiplications. Because we only need to store the first row of a block Toeplitz matrix, when a Toeplitz matrix is converted into a circulant matrix, we only need to store the first row of this circulant matrix as well as add $n - 2$ zero elements to the corresponding column vector. The size of the vector obtained using this circulant matrix vector multiplication is $2n_y - 2$ so that the last $n_y - 2$ elements of this vector should be removed to have an n_y -vector. We should perform the same procedure for the first row of each n_x Toeplitz matrices and column vectors that corresponds to these Toeplitz matrices. It should be noted that this block Toeplitz matrix makes a big Toeplitz matrix. Therefore, using the first row of a block Toeplitz matrix, we can do the same procedure for the other Toeplitz

matrices and find the final result.

Let's explain this using one example. Assume that the matrix W which is a block Toeplitz matrix with a size of $N \times N$ multiplies a column vector of length N . Further, assume that the size of each Toeplitz matrix is $n_y \times n_y$. For this matrix-vector multiplication, only the first N elements of this matrix are used. These first N elements correspond to the first row of the matrix W and are denoted by $W(1, :)$. Now, let's see how we can use the first row of this matrix, $W(1, :)$, to perform this matrix vector multiplication.

$$\begin{pmatrix} \text{Yellow} & \text{Red} & \text{Blue} & \text{Orange} & \text{Green} \\ \text{Red} & \text{Yellow} & \text{Red} & \text{Blue} & \text{Orange} \\ \text{Blue} & \text{Red} & \text{Yellow} & \text{Red} & \text{Blue} \\ \text{Orange} & \text{Blue} & \text{Red} & \text{Yellow} & \text{Red} \\ \text{Green} & \text{Orange} & \text{Blue} & \text{Red} & \text{Yellow} \end{pmatrix} \begin{pmatrix} \text{Pink} \\ \text{Pink} \\ \text{Pink} \\ \text{Pink} \\ \text{Pink} \end{pmatrix} = \begin{pmatrix} \text{Light Gray} \\ \text{Light Gray} \\ \text{Medium Gray} \\ \text{Dark Gray} \\ \text{Black} \end{pmatrix}$$

The first step corresponds to the case that the first n_y rows of the $N \times N$ matrix multiply a vector of size N as shown below. In this case, the first row of each of the following block Toeplitz matrices are known. We should add $n_y - 2$ elements (these additional elements are chosen based on the above explanation) to the first row of each Toeplitz matrices (for converting it to a circulant matrix) and add $n_y - 2$ zero elements to the corresponding column vector. Now, we can apply FFT multiplication. It should be noted that the size of the vector obtained from multiplication of each Toeplitz matrix with the corresponding column vector is a vector of length $(2n_y - 2)$. The last $n_y - 2$ elements of the results should be removed to have a column vector of length n_y . We should perform the same procedure for all the Toeplitz matrices which

are in the first n_y rows of $N \times N$ matrix. Therefore, the results of multiplication of each Toeplitz matrix with the corresponding column vector will be an n_y -vector. Finally, all these vectors of length n_y should be added.

$$\begin{pmatrix} \text{Yellow} & \text{Red} & \text{Blue} & \text{Orange} & \text{Green} \\ & & & & \\ & & & & \\ & & & & \\ & & & & \end{pmatrix} \begin{pmatrix} \text{Pink} \\ \text{Pink} \\ \text{Pink} \\ \text{Pink} \\ \text{Pink} \end{pmatrix} = \begin{pmatrix} \text{Grey} \\ \\ \\ \\ \end{pmatrix}$$

The second step corresponds to the case that the second n_y rows of the $N \times N$ matrix multiply an N -vector as shown below. It should be noted that we only have the first row of $N \times N$ matrix, $W(1, :)$. Now, let's see how can we use this information to find the results of the multiplication of the second n_y rows of $N \times N$ matrix by an N -vector. As can be seen this $N \times N$ matrix consists of some Toeplitz blocks and these Toeplitz blocks make a large Toeplitz matrix. Therefore, to find the first row of the second n_y rows of the $N \times N$ matrix, which is denoted by $W(n_y + 1, :)$, using the first row of $N \times N$ matrix, $W(1, :)$, we can use the properties of this large Toeplitz matrix. To this end, we need to remove the last n_y elements of $W(1, :)$ and then add the second n_y elements of the $W(1, :)$ as the first n_y elements to make $W(n_y + 1, :)$. Thus, we found the first row of the second n_y rows of the $N \times N$ matrix, $W(n_y + 1, :)$. Now, we should do the same procedure which is explained in the first step to perform

the matrix vector multiplication using the FFT method.

$$\begin{pmatrix} \color{red}{\square} & \color{yellow}{\square} & \color{red}{\square} & \color{blue}{\square} & \color{orange}{\square} \end{pmatrix} \begin{pmatrix} \color{pink}{\square} \\ \color{pink}{\square} \\ \color{pink}{\square} \\ \color{pink}{\square} \\ \color{pink}{\square} \end{pmatrix} = \begin{pmatrix} \color{gray}{\square} \end{pmatrix}$$

The third step corresponds to the case in which the third n_y rows of $N \times N$ matrix multiply an $N \times 1$ vector as shown below. Thus, similar to the previous step, we need to find the first row of this $n_y \times N$ matrix to use it for the FFT multiplication. To find this row denoted by $W(2n_y + 1, :)$, we need to use $W(1, :)$ and $W(n_y + 1, :)$. To this end, we should remove the last n_y elements of $W(n_y + 1, :)$ and then add the third n_y elements of $W(1, :)$ as the first n_y elements of $W(2n_y + 1, :)$. Therefore, all the elements of $W(2n_y + 1, :)$ are found and we can use this row to multiply this $n_y \times N$ with an N vector.

$$\begin{pmatrix} \color{blue}{\square} & \color{red}{\square} & \color{yellow}{\square} & \color{red}{\square} & \color{blue}{\square} \end{pmatrix} \begin{pmatrix} \color{pink}{\square} \\ \color{pink}{\square} \\ \color{pink}{\square} \\ \color{pink}{\square} \\ \color{pink}{\square} \end{pmatrix} = \begin{pmatrix} \color{gray}{\square} \end{pmatrix}$$

We should do the same procedure for all $n_y \times N$ matrices. It should be noted that

to find the first row of each of these $n_y \times N$ matrices, we only need to know the first row of the previous $n_y \times N$ matrix and $W(1, :)$.

4

Inverse Solver

Finding the quantitative acoustical properties of an object of interest (OI) is the goal in the UT inverse scattering problem. As has already been discussed, in this thesis we try to simultaneously reconstruct the contrast of compressibility and density profiles [6]. Having the quantitative profiles for these properties is useful for several applications: medical imaging for distinguishing between healthy tissues and malignant tissues, and industrial applications of non-destructive testing and evaluation [7, 35–37]. As shown in (2.69) and (3.2), UT can be mathematically formulated as an inverse scattering problem. This mathematical problem is non-linear and ill-posed. Mathematically speaking, non-linearity comes from the fact that the unknowns of this problem, *i.e.*, contrast profiles and the total pressure inside the domain, are nonlinearly related to the received pressure field which forms the data for the inverse problem. Physically speaking, non-linearity is due to multiple-scattering events within the OI. That is, ultrasound waves do not travel in straight lines within the OI; rather, they experience several scattering events while interrogating the OI. The ill-posedness of this problem will be addressed in the next chapter where regularization techniques are discussed.

To quantitatively solve this non-linear problem, various inversion algorithms have been proposed such as the Born Iterative Method (BIM) [6, 7, 18], the Distorted Born

iterative Method(DBIM) [19–22] and the Contrast Source inversion (CSI) algorithm [23]. To handle non-linearity, these algorithms are iterative. They try to deal with the multiple scattering within the OI by converging to a best estimate of multiple scattering events within the OI. Therefore, these algorithms provide more accurate reconstruction compared to linear (non-iterative) methods such as the Born and Rytov approximation methods (linear methods cannot model multiple scattering events). Therefore, linear methods introduce their own modelling error into the problem; *i.e.*, the discrepancy between the scattered field resulting from the OI and the numerical model of that field.

We choose to use a nonlinear method in this thesis wherein a cost function, which is related to the discrepancy between the measured and simulated data, is created and minimized. This cost function can be minimized using different types of optimization methods, but in this thesis, BIM is chosen as our non-linear inversion algorithm. The main reason for choosing this method is that BIM is more computationally efficient compared to CSI and DBIM [7]. This is due to the fact that as opposed to DBIM and CSI, BIM does not require the derivative of the cost function. However, the DBIM and CSI algorithms usually provide better reconstruction for high contrast objects compared to the BIM [7, 21]. However, in biomedical imaging application, tissues will typically have low contrast profiles, if the background medium (matching fluid) is chosen wisely [7]. Therefore, noting that we generally have more flexibility to choose an appropriate matching fluid, we can control the contrast of the OI to some extent. It should also be noted that when we have low contrast profiles, a greater proportion of the ultrasound wave energy will penetrate the OI (*i.e.*, more interrogation energy) providing more information about the OI. These considerations justify the use of BIM instead of DBIM and CSI for this application.

In Section 4.1, our formulation of the BIM equipped with balancing of the unknowns and the simultaneous use multiple-frequencies will be described. In Section 4.2, the two operators used in the data equation will be described and their adjoint will be derived. Section 4.3, addresses an efficient method to find the Green's function for the data operator. In Section 4.4, it will be explained how to formulate the data operator to simultaneously reconstruct both the contrast of compressibility and density profiles. Then, it will be shown how to numerically balance these two contrast profiles in the inversion algorithm. This balancing method plays an important role in better reconstruction of the contrast profiles. In Section 4.5, it will be shown how to simultaneously invert multiple-frequency data sets to reconstruct contrast profiles. The simultaneous inversion of multiple-frequency data sets provides better imaging results because more information about the OI is utilized.

4.1 Born Iterative Method (BIM)

We now explain how the BIM quantitatively solves this nonlinear ill-posed UT problem [6, 7, 16]. The steps of the BIM can be summarized as follows.

1. Use the incident pressure as the total pressure in the first iteration (this is the Born approximation). Note that in the case of multiple-frequency inversion (to be described), we will have different incident pressures for each frequency. Therefore, the number of incident field pressure vectors will be $nTx \times n_f$, each of these vector will have a length of N where nTx is the number of transmitters, n_f is the number of frequencies and N is the number of discretized elements in the imaging domain.
2. Linearize the associated integral equation by using the current approximate

value for the total pressure distribution within the imaging domain D and then solve for contrast profiles of OI. This requires the solution of a matrix equation. The matrix is the discretized form of the data operator, and the right-hand side is the measured scattered pressure. The conjugate gradient algorithm is applied to this matrix equation to solve the contrast profiles. The conjugate gradient algorithm requires the adjoint operators that we have already found. This step also takes advantage of the balancing method (to be described). Simultaneous frequency inversion is also incorporated into this step. To solve this matrix equation, care needs to be taken to handle the ill-posedness of this system of equations. This will need the use of an appropriate regularization technique, which will be discussed in the next chapter.

3. Calculate the total pressure inside the domain based on the contrast profiles predicted in the previous step. Now that we have newly predicted contrast profiles from the previous step, we can update the total pressure distribution within the imaging domain. In other words, in this step, we try to update our knowledge regarding the multiple scattering events within the object of interest. To this end, we need to run our forward solver $nT_x \times n_f$ times. As can be seen, this step is computationally expensive. Therefore, we have used a CG-FFT MoM in conjunction with the marching-on-in-source position technique as described in Chapter 3.
4. Find the simulated scattered pressure at the receiver locations using the predicted contrast profiles. Having the total pressure within the OI, we can now calculate the scattered pressure at the receiving sites using the data equation.
5. Find the residual between the measured and simulated scattered pressure. Hav-

ing the calculated scattered pressure from the previous step, we can find the discrepancy between the measured scattered pressure and the calculated (simulated) scattered pressure. This discrepancy tells us how close we are to the actual solution.

6. Go back to step 2, incorporate the newly calculated total pressure distribution, and continue iterations until the residual between the measured and simulated scattered pressure is sufficiently small.

4.2 Data Operator

The data operator takes a contrast profile and produces the scattered pressure at the specified receiver locations. For the UT case, this data operator is the sum of two different operators, one for each of the two contrast mechanisms in the UT problem. The first operator, which is denoted by \mathcal{G}_{1s} , operates on the complex contrast of compressibility. The second operator, denoted by \mathcal{G}_{2s} , operates on the contrast of inverse density.

According to (3.2), we can define these operators as

$$\mathcal{G}_{1s}(\cdot) \triangleq k_0^2 \int_D g(\mathbf{r}, \mathbf{r}')(\cdot)p(\mathbf{r}')d\mathbf{r}' \quad \mathbf{r} \notin D, \mathbf{r} \in S \quad (4.1)$$

$$\mathcal{G}_{2s}(\cdot) \triangleq \int_D g(\mathbf{r}, \mathbf{r}')\nabla \cdot [(\cdot)\nabla p(\mathbf{r}')]d\mathbf{r}' \quad \mathbf{r} \notin D, \mathbf{r} \in S \quad (4.2)$$

where subscript s denotes that the range of these two operators is in the measurement domain, S , *i.e.*, the domain containing the transceiver locations. When \mathcal{G}_{1s} and \mathcal{G}_{2s} operate on the contrast profiles, they map the properties within the imaging domain, $\mathbf{r}' \in D$, into pressure data outside the imaging domain, $\mathbf{r} \in S$. Note that these

operators are different from those operators which is explained in Chapter 3; *i.e.*, \mathcal{G}_1 and \mathcal{G}_2 . The operators \mathcal{G}_1 and \mathcal{G}_2 described in Chapter 3 are domain operators whose domain and range are both located within the imaging domain D .

The Scattered pressure can be found using these data operators by substituting (4.1) and (4.2) into (3.2) as

$$p^{scat}(\mathbf{r}) = \mathcal{G}_{1s}\{\chi_1^c(\mathbf{r}')\} + \mathcal{G}_{2s}\{\chi_2(\mathbf{r}')\} \quad (4.3)$$

The argument inside $\{\}$ is the argument in which the operator operates.

In several inversion algorithms, including the one utilized in this thesis, the adjoint of the data operators is required. Thus, the respective adjoint operators \mathcal{G}_{1s}^a and \mathcal{G}_{2s}^a need to be found. Using the definition of the adjoint operator, the adjoint \mathcal{G}_{1s}^a must satisfy the equation

$$\langle \mathcal{G}_{1s}\{\chi_1^c(\mathbf{r}')\}, \psi(\mathbf{r}) \rangle_S = \langle \chi_1^c(\mathbf{r}'), \mathcal{G}_{1s}^a\{\psi(\mathbf{r})\} \rangle_D \quad (4.4)$$

where $\langle \cdot, \cdot \rangle$ is the inner product and subscripts S and D denote the domain over which the inner products are taken. $\psi(\mathbf{r})$ is an arbitrary function over S . Thus, we see that \mathcal{G}_{1s}^a maps a function over S to one over D . According to the definition of the inner product, we can expand (4.4) as

$$\int_S \mathcal{G}_{1s}\{\chi_1^c(\mathbf{r}')\} \psi^*(\mathbf{r}) d\mathbf{r} = \int_D \chi_1^c(\mathbf{r}') [\mathcal{G}_{1s}^a\{\psi(\mathbf{r})\}]^* d\mathbf{r}' \quad (4.5)$$

where $*$ denotes the complex conjugate. Substituting (4.1) into the left side of (4.5),

we have

$$\begin{aligned}
W_1 &= \int_S \mathcal{G}_{1s}\{\chi_1^c(\mathbf{r}')\}\psi^*(\mathbf{r})d\mathbf{r} \\
&= \int_S k_0^2 \int_D g(\mathbf{r}, \mathbf{r}')\chi_1^c(\mathbf{r}')p(\mathbf{r}')d\mathbf{r}'\psi^*(\mathbf{r})d\mathbf{r} \\
&= \int_D k_0^2\chi_1^c(\mathbf{r}')p(\mathbf{r}') \int_S g(\mathbf{r}, \mathbf{r}')\psi^*(\mathbf{r})d\mathbf{r}d\mathbf{r}' \quad (4.6)
\end{aligned}$$

Comparing (4.6) with the right side of (4.5), it can be concluded that

$$[\mathcal{G}_{1s}^a\{\psi(\mathbf{r})\}]^* = k_0^2p(\mathbf{r}') \int_S g(\mathbf{r}, \mathbf{r}')\psi^*(\mathbf{r})d\mathbf{r} \quad (4.7)$$

Thus,

$$\mathcal{G}_{1s}^a\{\psi(\mathbf{r})\} = [k_0^2p(\mathbf{r}')]^* \int_S g^*(\mathbf{r}, \mathbf{r}')\psi(\mathbf{r})d\mathbf{r} \quad (4.8)$$

or in the general operator form:

$$\mathcal{G}_{1s}^a\{\cdot\} = [k_0^2p(\mathbf{r}')]^* \int_S g^*(\mathbf{r}, \mathbf{r}')(\cdot)d\mathbf{r} \quad (4.9)$$

We follow the same procedure to find \mathcal{G}_{2s}^a . Again the definition of the adjoint operator gives

$$\langle \mathcal{G}_{2s}\{\chi_2(\mathbf{r}')\}, \psi(\mathbf{r}) \rangle_S = \langle \chi_2(\mathbf{r}'), \mathcal{G}_{2s}^a\{\psi(\mathbf{r})\} \rangle_D \quad (4.10)$$

which can be expanded as the following form

$$\int_S \mathcal{G}_{2s}\{\chi_2(\mathbf{r}')\}\psi^*(\mathbf{r})d\mathbf{r} = \int_D \chi_2(\mathbf{r}')[\mathcal{G}_{2s}^a\{\psi(\mathbf{r})\}]^*d\mathbf{r}' \quad (4.11)$$

Substituting (4.2) into left side of (4.11), we have

$$\begin{aligned} W_2 &= \int_S \mathcal{G}_{2s}\{\chi_2(\mathbf{r}')\}\psi^*(\mathbf{r})d\mathbf{r} \\ &= \int_S \int_D g(\mathbf{r}, \mathbf{r}')\nabla' \cdot [\chi_2(\mathbf{r}')\nabla'p(\mathbf{r}')]d\mathbf{r}'\psi^*(\mathbf{r})d\mathbf{r} \end{aligned} \quad (4.12)$$

Using the identity

$$\nabla' \cdot [\chi_2(\mathbf{r}')\nabla'p(\mathbf{r}')] \equiv \nabla'\chi_2(\mathbf{r}') \cdot \nabla'p(\mathbf{r}') + \chi_2(\mathbf{r}')\nabla'^2p(\mathbf{r}') \quad (4.13)$$

we have

$$\begin{aligned} W_2 &= \int_S \int_D g(\mathbf{r}, \mathbf{r}')[\nabla'\chi_2(\mathbf{r}') \cdot \nabla'p(\mathbf{r}') + \chi_2(\mathbf{r}')\nabla'^2p(\mathbf{r}')]d\mathbf{r}'\psi^*(\mathbf{r})d\mathbf{r} \\ &= \int_S \int_D g(\mathbf{r}, \mathbf{r}')\nabla'\chi_2(\mathbf{r}') \cdot \nabla'p(\mathbf{r}')d\mathbf{r}'\psi^*(\mathbf{r})d\mathbf{r} \\ &+ \int_S \int_D g(\mathbf{r}, \mathbf{r}')\chi_2(\mathbf{r}')\nabla'^2p(\mathbf{r}')d\mathbf{r}'\psi^*(\mathbf{r})d\mathbf{r} \end{aligned} \quad (4.14)$$

For the simplicity in writing, we define $F(\mathbf{r}')$ as

$$F(\mathbf{r}') = \int_S g(\mathbf{r}, \mathbf{r}')\psi^*(\mathbf{r})d\mathbf{r} \quad (4.15)$$

to give

$$W_2 = \int_D F(\mathbf{r}')\nabla'\chi_2(\mathbf{r}') \cdot \nabla'p(\mathbf{r}')d\mathbf{r}' + \int_D F(\mathbf{r}')\chi_2(\mathbf{r}')\nabla'^2p(\mathbf{r}')d\mathbf{r}' \quad (4.16)$$

The first part of (4.16) can be expanded using the identity

$$\nabla'[F(\mathbf{r}')\chi_2(\mathbf{r}')] \equiv \chi_2(\mathbf{r}')\nabla'F(\mathbf{r}') + F(\mathbf{r}')\nabla'\chi_2(\mathbf{r}') \quad (4.17)$$

Therefore, the first part of (4.16) will be

$$\begin{aligned}
W_3 &= \int_D F(\mathbf{r}') \nabla' \chi_2(\mathbf{r}') \cdot \nabla' p(\mathbf{r}') d\mathbf{r}' \\
&= \int_D [\nabla' [F(\mathbf{r}') \chi_2(\mathbf{r}')] - \chi_2(\mathbf{r}') \nabla' F(\mathbf{r}')] \cdot \nabla' p(\mathbf{r}') d\mathbf{r}' \\
&= \int_D \nabla' [F(\mathbf{r}') \chi_2(\mathbf{r}')] \cdot \nabla' p(\mathbf{r}') d\mathbf{r}' - \int_D \chi_2(\mathbf{r}') \nabla' F(\mathbf{r}') \cdot \nabla' p(\mathbf{r}') d\mathbf{r}' \quad (4.18)
\end{aligned}$$

The first part of (4.18) can be expanded using (4.13) as

$$\begin{aligned}
W_4 &= \int_D \nabla' [F(\mathbf{r}') \chi_2(\mathbf{r}')] \cdot \nabla' p(\mathbf{r}') d\mathbf{r}' \\
&= \int_D [\nabla' \cdot [F(\mathbf{r}') \chi_2(\mathbf{r}') \nabla' p(\mathbf{r}')] - F(\mathbf{r}') \chi_2(\mathbf{r}') \nabla'^2 p(\mathbf{r}')] d\mathbf{r}' \\
&= \int_D \nabla' \cdot [F(\mathbf{r}') \chi_2(\mathbf{r}') \nabla' p(\mathbf{r}')] d\mathbf{r}' - \int_D F(\mathbf{r}') \chi_2(\mathbf{r}') \nabla'^2 p(\mathbf{r}') d\mathbf{r}' \\
&= \int_{\partial D} F(\mathbf{r}') \chi_2(\mathbf{r}') \nabla' p(\mathbf{r}') d\Gamma - \int_D F(\mathbf{r}') \chi_2(\mathbf{r}') \nabla'^2 p(\mathbf{r}') d\mathbf{r}' \quad (4.19)
\end{aligned}$$

where ∂D represents the integral over the boundary obtained using the divergence theorem. If we assume that the contrast of the inverse density is zero on the boundary, then the first term of W_4 will be zero. The second part of W_4 cancels with the second part of (4.16). Thus, W_2 can be written as

$$W_2 = - \int_D \chi_2(\mathbf{r}') \nabla' F(\mathbf{r}') \cdot \nabla' p(\mathbf{r}') d\mathbf{r}' \quad (4.20)$$

Comparing (4.20) with the right side of (4.11), we have

$$[\mathcal{G}_{2s}^a \{\psi(\mathbf{r})\}]^* = -\nabla' p(\mathbf{r}') \cdot \nabla' F(\mathbf{r}') \quad (4.21)$$

Substituting (4.15) into (4.21), we have

$$[\mathcal{G}_{2s}^a\{\psi(\mathbf{r})\}]^* = -\nabla' p(\mathbf{r}') \cdot \nabla' \int_S g(\mathbf{r}, \mathbf{r}') \psi^*(\mathbf{r}) d\mathbf{r} \quad (4.22)$$

Therefore, the adjoint we're looking for is

$$\mathcal{G}_{2s}^a\{\psi(\mathbf{r})\} = -\nabla' p^*(\mathbf{r}') \cdot \nabla' \int_S g^*(\mathbf{r}, \mathbf{r}') \psi(\mathbf{r}) d\mathbf{r} \quad (4.23)$$

or in the operator form:

$$\mathcal{G}_{2s}^a\{\cdot\} = -\nabla' p^*(\mathbf{r}') \cdot \nabla' \int_S g^*(\mathbf{r}, \mathbf{r}') (\cdot) d\mathbf{r} \quad (4.24)$$

The above adjoint operator is the same as the one used in [7]. This completes the derivation of the adjoint of the data operators needed by our inversion algorithm.

4.3 Efficient implementation of the data operator

This section deals with efficient implementation of the discretized data operator. The data operator is dependent on: (1) the Green's function value between a given point in the imaging domain and the receiver location, and (2) the total field pressure within the imaging domain due to the active transmitter. Therefore, the size of the matrix which represents the discretized data operator will be $(nTx \times nRx) \times N$ where nTx is the number of transmitters, nRx is the number of receivers per transmitter, and N is the number of discretized elements within the imaging domain.

As an example, let's assume that we have 60 transducer in a UT system. When one of these transducers is active as transmitter, the rest of the transducers work as receivers. Also, assume that the OI is discretized into 10000 pulse basis functions.

The size of the data operator will thus be 3540×10000 . That is, we need to calculate and store 3540×10000 complex values for each frequency.

An efficient method is used in this thesis wherein we only calculate and store $nA \times N$ complex numbers, where nA is the total number of receiving transducers. For example, in the above example, the total number of transducers is $nA = 60$. Therefore, 60×10000 complex numbers need to be calculated and stored which require 59 times less storage. This procedure is now explained.

As mentioned in Section 3.3.2, the Green's function for our 2D time-harmonic problem with $e^{+j\omega t}$ time-dependency is

$$g(\mathbf{r}, \mathbf{r}') = \frac{1}{4j} H_0^{(2)}(k_0 |\mathbf{r} - \mathbf{r}'|) \quad (4.25)$$

where k_0 is the wavenumber of the background medium neglecting attenuation and H_0^2 is the zeroth-order Hankel function of the second kind. It should be noted that in contrast to the domain equation, where both \mathbf{r} and \mathbf{r}' belong to the imaging domain ($\mathbf{r}, \mathbf{r}' \in D$), the data equation is used to find the scattered pressure at receivers locations outside of the imaging domain, $\mathbf{r} \notin D$. In the data equation, $\mathbf{r}' \in D, \mathbf{r} \in S$. For the data equation, we cannot take advantages of the properties of a Toeplitz block matrix as was the case for the domain equation. This is due to the fact that, \mathbf{r} and \mathbf{r}' belong to different domains.

In this thesis, we calculate and store the Green's function values between the receiver locations and the discretized elements within the imaging domain, independent of the active transmitter. This results in a matrix having the size of $nA \times N$. We also store the total pressure within the imaging domain per each transmitter in a different matrix having the size of $nTx \times N$. In other words as opposed to creating one matrix of the size $(nTx \times nRx) \times N$, we create two smaller matrices of sizes $nA \times N$ and

$nTx \times N$. Then these two matrices can be used to implement the data operator on the contrast profiles. In fact, this implementation does not explicitly construct the data operator matrix. It implements the “operation” of the data operator using two smaller matrices.

This technique is implemented using object oriented programming where we do not have the actual matrix of the data operator stored, but rather have a function which calculates the result of the operation of the data operator on contrast profiles. This method is especially useful for large-scale problems, such as 3D UT, in which the actual matrix for the data operator can be quite large. This method was originally used in microwave tomography [73], and here we apply it to the UT problem.

It should also be noted that the above discussion was for the case of single frequency. We have extended the above methods to the case of multiple frequencies. Although the implementation of the above method is more complicated for the multiple frequency case, it uses the same idea as presented above.

4.4 Balancing of the Contrasts

The contrast variables have different magnitudes and must be balanced in order for the BIM inversion to work well. It has already been shown shown in microwave tomography that this balancing can create enhanced reconstructions [74]. The idea behind this method is that if, for example, we have two unknowns but one unknown is much greater than the other, the numerical algorithm will tend to favour the reconstruction of the larger unknown. In microwave tomography, the real part of the permittivity profile is often larger than the imaginary part of the permittivity and without prior balancing, the resulting quantitative image of the real part of the permittivity is much more accurate than that of the imaginary part of the permittivity

profile.

To balance the unknowns, the expected range of the contrast profiles for the OI should be known. For example, if we want to apply a balancing method for breast imaging, we should know the range of values that can be expected for each of the contrast profiles for different breast tissues. This information is required for the proper balancing of the reconstruction of contrast profiles. In other words, balancing the unknowns needs some form of prior information about the OI. In practical situations, this prior information is usually available. For example, the expected range of compressibility and density for different breast tissues are known. Therefore, the ratio between the expected values for the compressibility and density values can be estimated and then used in the balancing algorithm.

Now, let's consider how this method can be applied to the UT problem. To this end, \mathcal{G}_{1s} , \mathcal{G}_{2s} and the contrast profiles should be split into the real and imaginary parts. This is due to the fact that the real and imaginary parts of compressibility and density profiles can have different ranges of value. When \mathcal{G}_{1s} operates on the complex contrast of compressibility, we have

$$\mathcal{G}_{1s}\{\chi_1^c\} = (\mathcal{G}_{1s_r} + j\mathcal{G}_{1s_i})\{\chi_{1r}^c + j\chi_{1i}^c\} \quad (4.26)$$

$$\mathcal{G}_{1s_r}\{\cdot\} \triangleq \text{Re}\left(\mathcal{G}_{1s}\{\cdot\}\right) \quad (4.27)$$

$$\mathcal{G}_{1s_i}\{\cdot\} \triangleq \text{Im}\left(\mathcal{G}_{1s}\{\cdot\}\right) \quad (4.28)$$

where \mathcal{G}_{1s_r} and \mathcal{G}_{1s_i} are the real and imaginary part of the operator \mathcal{G}_{1s} respectively. The real and imaginary parts of χ_1^c are denoted by χ_{1r}^c and χ_{1i}^c . The above equation

can be written in the following form

$$\mathcal{G}_{1s}\{\chi_1^c\} = \left[\mathcal{G}_{1s_r}\{\chi_{1r}^c\} - \mathcal{G}_{1s_i}\{\chi_{1i}^c\} \right] + j \left[\mathcal{G}_{1s_i}\{\chi_{1r}^c\} + \mathcal{G}_{1s_r}\{\chi_{1i}^c\} \right] \quad (4.29)$$

Symbolically, we can write the above equation as

$$\begin{pmatrix} \mathcal{G}_{1s_r} & -\mathcal{G}_{1s_i} \\ \mathcal{G}_{1s_i} & \mathcal{G}_{1s_r} \end{pmatrix} \begin{pmatrix} \chi_{1r}^c \\ \chi_{1i}^c \end{pmatrix} = \begin{pmatrix} \text{Re}(\mathcal{G}_{1s}\{\chi_1^c\}) \\ \text{Im}(\mathcal{G}_{1s}\{\chi_1^c\}) \end{pmatrix} \quad (4.30)$$

where $\text{Re}(\cdot)$ and $\text{Im}(\cdot)$ denote the real and imaginary parts of whatever is in the parentheses.

When \mathcal{G}_{2s} operates on the contrast of inverse density, we have

$$\mathcal{G}_{2s}\{\chi_2\} = (\mathcal{G}_{2s_r} + j\mathcal{G}_{2s_i})\{\chi_{2r} + j\chi_{2i}\} \quad (4.31)$$

$$\mathcal{G}_{2s_r}\{\cdot\} \triangleq \text{Re}\left(\mathcal{G}_{2s}\{\cdot\}\right) \quad (4.32)$$

$$\mathcal{G}_{2s_i}\{\cdot\} \triangleq \text{Im}\left(\mathcal{G}_{2s}\{\cdot\}\right) \quad (4.33)$$

where \mathcal{G}_{2s_r} and \mathcal{G}_{2s_i} are the real and imaginary parts of the operator \mathcal{G}_{2s} , respectively. The real and imaginary parts of χ_2 are denoted by χ_{2r} and χ_{2i} . We also know that χ_2 is real, that is $\chi_{2i} = 0$. Thus, we have

$$\mathcal{G}_{2s}\{\chi_2\} = \mathcal{G}_{2s_r}\{\chi_{2r}\} + j\mathcal{G}_{2s_i}\{\chi_{2r}\} \quad (4.34)$$

The above equation can be written as

$$\begin{pmatrix} \text{Re}(\mathcal{G}_{2s}\{\chi_2\}) \\ \text{Im}(\mathcal{G}_{2s}\{\chi_2\}) \end{pmatrix} = \begin{pmatrix} \mathcal{G}_{2s_r} \\ \mathcal{G}_{2s_i} \end{pmatrix} \chi_{2r} \quad (4.35)$$

The scattered pressure is written as

$$p^{scat} = \begin{pmatrix} \mathcal{G}_{1s} & \mathcal{G}_{2s} \end{pmatrix} \begin{pmatrix} \chi_1^c \\ \chi_2 \end{pmatrix} \quad (4.36)$$

Noting that when \mathcal{G}_{1s} and \mathcal{G}_{2s} operators, operate on the χ_1^c and χ_2 respectively, the result of each operation is a vector of length $nRx \times nTx$. It should be noted that χ_1^c and χ_2 correspond to the discretized form of $\chi_1^c(\mathbf{r})$ and $\chi_2(\mathbf{r})$ respectively. Expanding (4.30) and (4.35), we have

$$\begin{pmatrix} p_r^{scat} \\ p_i^{scat} \end{pmatrix} = \begin{pmatrix} \mathcal{G}_{1s_r} & -\mathcal{G}_{1s_i} & \mathcal{G}_{2s_r} \\ \mathcal{G}_{1s_i} & \mathcal{G}_{1s_r} & \mathcal{G}_{2s_i} \end{pmatrix} \begin{pmatrix} \chi_{1r}^c \\ \chi_{1i}^c \\ \chi_{2r} \end{pmatrix} \quad (4.37)$$

where p_r^{scat} and p_i^{scat} are the real and imaginary parts of scattered pressure. The size of each of these column vectors is $(nRx \times nTx)$. It should be noted that in (4.37), the contrast column vector consists of the real and imaginary parts of χ_1^c and the real part of χ_2 . Having all the contrast profiles in a single column vector is very useful because, in this thesis, the goal is to simultaneously reconstruct the contrast of compressibility and density profiles. Thus, this vector constitutes the unknowns of the inversion algorithm. This $3N$ vector is updated at each iteration of the inversion algorithm.

To apply the balancing method, we introduce scalar balancing coefficients Q_1, Q_2 ,

and Q_3 into (4.37) as follows

$$\begin{pmatrix} p_r^{scat} \\ p_i^{scat} \end{pmatrix} = \begin{pmatrix} \boxed{Q_1} \mathcal{G}_{1s_r} & \boxed{Q_2} -\mathcal{G}_{1s_i} & \boxed{Q_3} \mathcal{G}_{2s_r} \\ \boxed{Q_1} \mathcal{G}_{1s_i} & \boxed{Q_2} \mathcal{G}_{1s_r} & \boxed{Q_3} \mathcal{G}_{2s_i} \end{pmatrix} \begin{pmatrix} \boxed{Q_1^{-1}} \chi_{1r}^c \\ \boxed{Q_2^{-1}} \chi_{1i}^c \\ \boxed{Q_3^{-1}} \chi_{2r} \end{pmatrix} \quad (4.38)$$

Therefore, if we know the range of expected values for the contrast profiles, we can choose the scalars Q_1 , Q_2 and Q_3 so as to balance the values of the elements in these contrast profiles. In the following, we define new contrast profiles and consider the effect on the computations of including these balancing coefficients. New contrast profiles are defined as

$$\chi_{1r}^{cn} = \frac{\chi_{1r}^c}{Q_1} \quad (4.39)$$

$$\chi_{1i}^{cn} = \frac{\chi_{1i}^c}{Q_2} \quad (4.40)$$

$$\chi_{2r}^n = \frac{\chi_{2r}}{Q_3} \quad (4.41)$$

where the superscript n denotes that these are the normalized contrast vectors which are balanced using the balancing coefficients. Substituting these into (4.38), we have

$$\begin{pmatrix} p_r^{scat} \\ p_i^{scat} \end{pmatrix} = \begin{pmatrix} \boxed{Q_1} \mathcal{G}_{1s_r} & \boxed{Q_2} -\mathcal{G}_{1s_i} & \boxed{Q_3} \mathcal{G}_{2s_r} \\ \boxed{Q_1} \mathcal{G}_{1s_i} & \boxed{Q_2} \mathcal{G}_{1s_r} & \boxed{Q_3} \mathcal{G}_{2s_i} \end{pmatrix} \begin{pmatrix} \chi_{1r}^{cn} \\ \chi_{1i}^{cn} \\ \chi_{2r}^n \end{pmatrix} \quad (4.42)$$

According to (4.42), the real and imaginary parts of scattered pressure can be found as

$$p_r^{scat} = Q_1 \operatorname{Re} \left(\mathcal{G}_{1s} \{ \chi_{1r}^{cn} \} \right) - Q_2 \operatorname{Im} \left(\mathcal{G}_{1s} \{ \chi_{1i}^{cn} \} \right) + Q_3 \operatorname{Re} \left(\mathcal{G}_{2s} \{ \chi_{2r}^n \} \right) \quad (4.43)$$

$$p_i^{scat} = Q_1 \text{Im} \left(\mathcal{G}_{1s} \{ \chi_{1r}^{cn} \} \right) + Q_2 \text{Re} \left(\mathcal{G}_{1s} \{ \chi_{1i}^{cn} \} \right) + Q_3 \text{Im} \left(\mathcal{G}_{2s} \{ \chi_{2r}^n \} \right) \quad (4.44)$$

Now, we consider how these coefficients affect the adjoint operators. Now that we have introduced balancing coefficients, we need to incorporate these into the adjoint operators. The following explains how the adjoint operator are implemented when balancing coefficients are included. It should be noted that in the inversion algorithm, the adjoint operators operate on the results of applying the data operator to the contrast profiles, that is, the adjoint operators operate on the scattered pressure vector. Therefore, when \mathcal{G}_{1s}^a operates on the scattered pressure, we can split the adjoint operator and scattered pressure into its real and imaginary parts as

$$\mathcal{G}_{1s}^a \{ p^{scat} \} = (\mathcal{G}_{1s_r}^a + j \mathcal{G}_{1s_i}^a) \{ p_r^{scat} + j p_i^{scat} \} \quad (4.45)$$

$$\mathcal{G}_{1s_r}^a \{ \cdot \} \triangleq \text{Re} \left(\mathcal{G}_{1s}^a \{ \cdot \} \right) \quad (4.46)$$

$$\mathcal{G}_{1s_i}^a \{ \cdot \} \triangleq \text{Im} \left(\mathcal{G}_{1s}^a \{ \cdot \} \right) \quad (4.47)$$

where subscripts r and i denote the real and imaginary parts of \mathcal{G}_{1s}^a and p^{scat} . Thus, the real and imaginary parts of the result can be found as

$$\mathcal{G}_{1s}^a \{ p^{scat} \} = \left[\mathcal{G}_{1s_r}^a \{ p_r^{scat} \} + \mathcal{G}_{1s_r}^a \{ j p_i^{scat} \} \right] + j \left[\mathcal{G}_{1s_i}^a \{ p_r^{scat} \} + \mathcal{G}_{1s_i}^a \{ j p_i^{scat} \} \right] \quad (4.48)$$

The above equation can be written in matrix form as

$$\begin{pmatrix} \mathcal{G}_{1s_r}^a & \mathcal{G}_{1s_r}^a \\ \mathcal{G}_{1s_i}^a & \mathcal{G}_{1s_i}^a \end{pmatrix} \begin{pmatrix} p_r^{scat} \\ j p_i^{scat} \end{pmatrix} = \begin{pmatrix} \text{Re}(\mathcal{G}_{1s}^a \{ p^{scat} \}) \\ \text{Im}(\mathcal{G}_{1s}^a \{ p^{scat} \}) \end{pmatrix} \quad (4.49)$$

We perform the same procedure for \mathcal{G}_{2s}^a . Thus, we have

$$\mathcal{G}_{2s}^a \{p^{scat}\} = (\mathcal{G}_{2s_r}^a + j\mathcal{G}_{2s_i}^a) \{p_r^{scat} + jp_i^{scat}\} \quad (4.50)$$

$$\mathcal{G}_{2s_r}^a \{\cdot\} \triangleq \text{Re} \left(\mathcal{G}_{2s}^a \{\cdot\} \right) \quad (4.51)$$

$$\mathcal{G}_{2s_i}^a \{\cdot\} \triangleq \text{Im} \left(\mathcal{G}_{2s}^a \{\cdot\} \right) \quad (4.52)$$

The real and imaginary parts of $\mathcal{G}_{2s}^a \{p^{scat}\}$ can be written as

$$\mathcal{G}_{2s}^a \{p^{scat}\} = \left[\mathcal{G}_{2s_r}^a \{p_r^{scat}\} + \mathcal{G}_{2s_r}^a \{jp_i^{scat}\} \right] + j \left[\mathcal{G}_{2s_i}^a \{p_r^{scat}\} + \mathcal{G}_{2s_i}^a \{jp_i^{scat}\} \right] \quad (4.53)$$

Again, because the contrast of the inverse density, χ_2 , is real, the second part of (4.53) is zero. The matrix form of $\mathcal{G}_{2s}^a \{p^{scat}\}$ can be written as

$$\begin{pmatrix} \text{Re}(\mathcal{G}_{2s}^a \{p^{scat}\}) \\ \text{Im}(\mathcal{G}_{2s}^a \{p^{scat}\}) \end{pmatrix} = \begin{pmatrix} \mathcal{G}_{2s_r}^a & \mathcal{G}_{2s_r}^a \\ \mathcal{G}_{2s_i}^a & \mathcal{G}_{2s_i}^a \end{pmatrix} \begin{pmatrix} p_r^{scat} \\ jp_i^{scat} \end{pmatrix} \quad (4.54)$$

Using (4.49) and (4.54), we write the adjoint operator as

$$\begin{pmatrix} x_1 \\ x_2 \\ x_3 \end{pmatrix} = \begin{pmatrix} \mathcal{G}_{1s_r}^a & \mathcal{G}_{1s_r}^a \\ \mathcal{G}_{1s_i}^a & \mathcal{G}_{1s_i}^a \\ \mathcal{G}_{2s_r}^a & \mathcal{G}_{2s_r}^a \end{pmatrix} \begin{pmatrix} p_r^{scat} \\ jp_i^{scat} \end{pmatrix} \quad (4.55)$$

It should be noted that the size of each column vector x_1 , x_2 , and x_3 is N . We now apply balancing coefficients to the adjoint matrix. According to (4.38), we can

understand how these coefficients affect the above equation.

$$\begin{pmatrix} x_1 \\ x_2 \\ x_3 \end{pmatrix} = \begin{pmatrix} \boxed{Q_1} \mathcal{G}_{1s_r}^a & \boxed{Q_1} \mathcal{G}_{1s_r}^a \\ \boxed{Q_2} \mathcal{G}_{1s_i}^a & \boxed{Q_2} \mathcal{G}_{1s_i}^a \\ \boxed{Q_3} \mathcal{G}_{2s_r}^a & \boxed{Q_3} \mathcal{G}_{2s_r}^a \end{pmatrix} \begin{pmatrix} p_r^{scat} \\ jp_i^{scat} \end{pmatrix} \quad (4.56)$$

Thus, we have

$$x_1 = Q_1 \operatorname{Re} \left(\mathcal{G}_{1s}^a \{p_r^{scat}\} \right) + Q_1 \operatorname{Re} \left(\mathcal{G}_{1s}^a \{jp_i^{scat}\} \right) \quad (4.57)$$

$$x_2 = Q_2 \operatorname{Im} \left(\mathcal{G}_{1s}^a \{p_r^{scat}\} \right) + Q_2 \operatorname{Im} \left(\mathcal{G}_{1s}^a \{jp_i^{scat}\} \right) \quad (4.58)$$

$$x_3 = Q_3 \operatorname{Re} \left(\mathcal{G}_{2s}^a \{p_r^{scat}\} \right) + Q_3 \operatorname{Re} \left(\mathcal{G}_{2s}^a \{jp_i^{scat}\} \right) \quad (4.59)$$

It should be noted that x_1 , x_2 and x_3 correspond to χ_{1r}^{cn} , χ_{1i}^{cn} and χ_{2r}^n respectively. Therefore, if we use a balancing method in the inversion algorithm, a $3N$ vector is found at each iteration of the inversion algorithm. The first N elements correspond to χ_{1r}^{cn} , the next N elements correspond to χ_{1i}^{cn} , and the last N elements correspond to χ_{2r}^n . To find the actual values of the contrast profiles, each contrast profiles should be multiplied by its corresponding balancing coefficient.

4.5 Simultaneous frequency inversion

In UT, we are usually faced with a large domain problem in terms of the wavelength [7]. The number of unknowns is very large. As mentioned in Section 4.4, if we assume that the total number of pixels in the imaging domain is N , then the number of unknowns will be $3N$. These unknowns are the real and imaginary part of contrast of compressibility and the contrast of inverse density (each of them is an N vector).

For example, if we assume that the size of the domain is $20\lambda \times 20\lambda$ and we use 10 cells per wavelength, then the total number of cells in the imaging domain will be $N = 200 \times 200 = 40000$. The total number of unknowns will be $3N = 120000$. To successfully reconstruct this many unknowns requires that we obtain sufficient information about the OI. There are two well-known ways to get more information about the OI:

- Increasing the number of receivers and transmitters.
- Using multiple-frequency data sets instead of a single-frequency data set.

For any measurement system, we can usually only incorporate a limited number of transmitters and receivers. Therefore, the only way to compensate for this imbalance between the number of data and the number of unknowns is to perform our measurements at multiple frequencies, thus generating more information about the OI.

Two different methods are proposed to invert a multiple-frequency data set: (1) a frequency hopping technique, and (2) a simultaneous frequency inversion technique. In the frequency hopping technique, the inversion is first applied to the lowest frequency data set. The converged image will be given as the initial guess to the inversion algorithm when applied to the next higher frequency data set. This process continues until all frequency data sets have been used. In other words, the frequency hopping technique attempts to first reconstruct low resolution information about the OI. As we use higher frequency data sets, the algorithm will provide higher resolution information about the OI [8, 9, 19].

In the second method, the data sets for all the frequencies are used simultaneously to reconstruct the OI [6, 10–13]. The simultaneous frequency inversion method is much more complicated in terms of the code development compared to the frequency

hopping technique. However, the results obtained using this method are usually much better than the frequency hopping technique. In this thesis, simultaneous frequency inversion is used.

To implement simultaneous frequency inversion, scattered pressure values for all the, say n_f , frequencies are concatenated and stored in a single vector. The matrix form of the data operator for these simultaneous frequencies can then be written as

$$\begin{pmatrix}
 \begin{array}{ccc}
 Q_1 \mathcal{G}_{1s_r, f_1} & -Q_2 \mathcal{G}_{1s_i, f_1} & Q_3 \mathcal{G}_{2s_r, f_1} \\
 Q_1 \mathcal{G}_{1s_i, f_1} & Q_2 \mathcal{G}_{1s_r, f_1} & Q_3 \mathcal{G}_{2s_i, f_1}
 \end{array} \\
 \begin{array}{ccc}
 Q_1 \mathcal{G}_{1s_r, f_2} & -Q_2 \mathcal{G}_{1s_i, f_2} & Q_3 \mathcal{G}_{2s_r, f_2} \\
 Q_1 \mathcal{G}_{1s_i, f_2} & Q_2 \mathcal{G}_{1s_r, f_2} & Q_3 \mathcal{G}_{2s_i, f_2}
 \end{array} \\
 \vdots & \vdots & \vdots \\
 \begin{array}{ccc}
 Q_1 \mathcal{G}_{1s_r, f_{n_f-1}} & -Q_2 \mathcal{G}_{1s_i, f_{n_f-1}} & Q_3 \mathcal{G}_{2s_r, f_{n_f-1}} \\
 Q_1 \mathcal{G}_{1s_i, f_{n_f-1}} & Q_2 \mathcal{G}_{1s_r, f_{n_f-1}} & Q_3 \mathcal{G}_{2s_i, f_{n_f-1}}
 \end{array} \\
 \begin{array}{ccc}
 Q_1 \mathcal{G}_{1s_r, f_{n_f}} & -Q_2 \mathcal{G}_{1s_i, f_{n_f}} & Q_3 \mathcal{G}_{2s_r, f_{n_f}} \\
 Q_1 \mathcal{G}_{1s_i, f_{n_f}} & Q_2 \mathcal{G}_{1s_r, f_{n_f}} & Q_3 \mathcal{G}_{2s_i, f_{n_f}}
 \end{array}
 \end{pmatrix}
 \begin{pmatrix}
 \chi_{1r}^{cn} \\
 \chi_{1i}^{cn} \\
 \vdots \\
 \chi_{2r}^n
 \end{pmatrix}
 =
 \begin{pmatrix}
 \begin{array}{c}
 p_{r, f_1}^{scat} \\
 p_{i, f_1}^{scat}
 \end{array} \\
 \begin{array}{c}
 p_{r, f_2}^{scat} \\
 p_{i, f_2}^{scat}
 \end{array} \\
 \vdots \\
 \begin{array}{c}
 p_{r, f_{n_f-1}}^{scat} \\
 p_{i, f_{n_f-1}}^{scat}
 \end{array} \\
 \begin{array}{c}
 p_{r, f_{n_f}}^{scat} \\
 p_{i, f_{n_f}}^{scat}
 \end{array}
 \end{pmatrix}
 \quad (4.60)$$

where f_1, f_2, \dots, f_{n_f} denote the n_f data sets. Each block in the data operator matrix corresponds to the data operator at a specific frequency. When the data operator for each frequency operates on the contrast profiles, the scattered pressure corresponding to that frequency is found. For example, when the yellow block in the data operator matrix, which corresponds to the data operator for frequency f_1 , operates on the contrast profiles vector, the scattered pressure due to the first frequency is found. We also use the yellow block for this scattered pressure to indicate that this scattered

pressure corresponds to f_1 . It should be noted that the size of the scattered pressure vector for each frequency is $(2 \times nRx \times nTx)$ where the first $nRx \times nTx$ elements correspond to the real part of scattered pressure and the second $nRx \times nTx$ elements correspond to the imaginary part of scattered pressure at that frequency. Thus, the size of scattered pressure vector in (4.60) will be $(2 \times nRx \times nTx \times n_f)$.

Now consider how the adjoint of the data operator works for simultaneous frequency inversion. The adjoint of the data operator for a single frequency is shown in (4.56). The expansion of (4.56) for simultaneous frequency inversion is shown in (4.61). As shown in (4.61), when the adjoint operator for each frequency operates on the vector that is related to scattered pressure at that frequency, a $3N \times 1$ vector is obtained. To indicate the results of each frequency, the subscripts f_1, f_2, \dots, f_{n_f} are used and we also use a specific colour for each frequency to distinguish the components of each frequency. For example, when the green block which corresponds to the first frequency operates on the scattered pressure for that frequency, we can find x_1, x_2 and x_3 for that frequency. Each of them is a column vector of length N . We also put the results in a block of the same colour to indicate that it corresponds to that

frequency.

$$\begin{pmatrix}
 \begin{matrix} Q_1 \mathcal{G}_{1s_r, f_1}^a & Q_1 \mathcal{G}_{1s_r, f_1}^a \\ Q_2 \mathcal{G}_{1s_i, f_1}^a & Q_2 \mathcal{G}_{1s_i, f_1}^a \\ Q_3 \mathcal{G}_{2s_r, f_1}^a & Q_3 \mathcal{G}_{2s_r, f_1}^a \end{matrix} &
 \begin{matrix} Q_1 \mathcal{G}_{1s_r, f_2}^a & Q_1 \mathcal{G}_{1s_r, f_2}^a \\ Q_2 \mathcal{G}_{1s_i, f_2}^a & Q_2 \mathcal{G}_{1s_i, f_2}^a \\ Q_3 \mathcal{G}_{2s_r, f_2}^a & Q_3 \mathcal{G}_{2s_r, f_2}^a \end{matrix} &
 \cdots &
 \begin{matrix} Q_1 \mathcal{G}_{1s_r, f_{n_f}}^a & Q_1 \mathcal{G}_{1s_r, f_{n_f}}^a \\ Q_2 \mathcal{G}_{1s_i, f_{n_f}}^a & Q_2 \mathcal{G}_{1s_i, f_{n_f}}^a \\ Q_3 \mathcal{G}_{2s_r, f_{n_f}}^a & Q_3 \mathcal{G}_{2s_r, f_{n_f}}^a \end{matrix}
 \end{pmatrix} \times
 \begin{pmatrix}
 \begin{matrix} p_{r, f_1}^{\text{scat}} \\ j p_{i, f_1}^{\text{scat}} \end{matrix} \\
 \begin{matrix} p_{r, f_2}^{\text{scat}} \\ j p_{i, f_2}^{\text{scat}} \end{matrix} \\
 \vdots \\
 \begin{matrix} p_{r, f_{n_f}}^{\text{scat}} \\ j p_{i, f_{n_f}}^{\text{scat}} \end{matrix}
 \end{pmatrix}
 =
 \begin{pmatrix}
 \begin{matrix} x_{1, f_1} \\ x_{2, f_1} \\ x_{3, f_1} \end{matrix} +
 \begin{matrix} x_{1, f_2} \\ x_{2, f_2} \\ x_{3, f_2} \end{matrix} +
 \cdots +
 \begin{matrix} x_{1, f_{n_f}} \\ x_{2, f_{n_f}} \\ x_{3, f_{n_f}} \end{matrix}
 \end{pmatrix}
 \tag{4.61}$$

5

Regularization Methods

The fact that the UT problem is ill-posed means that a small change in the measured pressure data can lead to a huge change in the predicted contrast profiles. Therefore, regularization methods, such as the Truncated Singular Value Decomposition (TSVD) [27, 75], the standard Tikhonov [22, 26–28], various type of Multiplicative [30, 31], the Conjugate Gradient Least Squares (CGLS) [24, 25, 27] or the L_1 -norm Tikhonov methods [32, 33], should be applied to handle the ill-posedness of this problem. In this thesis, the CGLS regularization technique is chosen because it is computationally efficient, requiring only a few matrix-vector multiplications [6, 24, 25]. In contrast to some other regularization techniques such as the TSVD method, the CGLS regularization method does not require the full storage of the ill-posed matrix. Noting that in UT we are usually faced with a large domain problem due to the small operating wavelength, the CGLS regularization method is a reasonable choice.

In this chapter, the ill-posedness of the inverse problem is described. The concept of regularization is then explained using the idea of singular value decomposition (SVD). Finally, some regularization methods, including the one used in this thesis, will be explained.

5.1 Why do we need a regularization?

According to Hadamard's definition, a well-posed problem must satisfy the following three criteria [17, 76]:

1. The solution must exist.
2. The solution must be unique.
3. The solution must be stable.

In our UT problem, we know that a solution exists because there is an object to be imaged in the measurement system. Regarding the uniqueness of the solution, it cannot be generally guaranteed for the UT problem. In fact, several acoustical profiles might result in the same scattered pressure data. However, there is generally a remedy for having multiple solutions: collecting more data. That is, as we collect more data (e.g., by having more transducers or more frequencies, etc) we reduce the number of possible solutions. In fact, in electromagnetic imaging, it has been shown that under some conditions, the electromagnetic inverse scattering problem can have a unique solution [77, 78]. On the other hand, the instability of the solution with respect to a small change in the measured data is always present due to the mathematical formulation of this problem. Therefore, the main effort of regularization techniques is to handle this instability. Note that small changes in the measured data cannot be controlled due to measurement noise. Thus, regularization techniques mainly try to handle the instability of the inverse problem.

We now look at the UT mathematical formulation to explain the ill-posedness of this problem. The data equation in the UT problem is ill-posed because it is a Fredholm integral equation of the first kind where all the unknowns of the problem are

inside the integral and the Green's function of this integral (Kernel) has no singularity [79, 80]. The general form of a Fredholm integral equation of the first kind is

$$\int_a^b K(\mathbf{r}, \mathbf{r}')q(\mathbf{r}')d\mathbf{r}' = w(\mathbf{r}) \quad (5.1)$$

where $K(\mathbf{r}, \mathbf{r}')$ is the Kernel function, $w(\mathbf{r})$ represents the measurement results and $q(\mathbf{r}')$ is the unknown of this problem which resides inside the integral. For imaging problems, the observation point, \mathbf{r} , is outside the domain of integration. The fact that \mathbf{r} and \mathbf{r}' cannot be the same means that the Kernel of this integral equation does not have a singularity. That is the Kernel is smooth [80]. One of the issues in this type of Fredholm integral equation of the first kind is that $w(\mathbf{r})$ is smoother than $q(\mathbf{r}')$ [27, 80, 81]. This means that the integral operation of the kernel on the unknown results in some loss of high-spatial frequency information. The integral operator act as a low-pass filter, passing low-spatial frequency components, and suppressing the high-spatial frequency components. Noting that high-spatial frequency components might be lost in the noise, the integral operator might develop a numerical nullspace [79, 82]. Having a numerical nullspace, we may be faced with a set of solutions (*i.e.*, a non uniqueness of the solution).

5.2 The Singular Value Decomposition

The discrete form of the data operator shown in (4.60) can be considered as a matrix equation $Ax = b$ where the matrix A represents the discrete form of the data operator, the vector b stores the measured scattered pressure at the receiving sites, and the vector x is the vector of unknowns. Using the singular value decomposition,

A can be written as [27, 75, 80]

$$A = U\Sigma V^H \quad (5.2)$$

where $U = (u_1, u_2, \dots, u_m)$ and $V = (v_1, v_2, \dots, v_m)$ are orthonormal matrices that contain the left and right singular vectors of the matrix A , respectively [27]. The superscript H denotes the Hermitian operator. The diagonal matrix Σ contains the singular values of the matrix A [27, 75, 80]:

$$\Sigma = \begin{pmatrix} \sigma_1 & 0 & \cdots & 0 & 0 \\ 0 & \sigma_2 & 0 & \cdots & 0 \\ \vdots & 0 & \sigma_3 & \ddots & \vdots \\ 0 & \ddots & \ddots & \ddots & 0 \\ 0 & 0 & \cdots & 0 & \sigma_m \end{pmatrix}, \quad 0 \leq \sigma_m \leq \cdots \leq \sigma_3 \leq \sigma_2 \leq \sigma_1 \quad (5.3)$$

Note that the diagonal elements of the matrix Σ are ordered starting with the largest singular value. In general, the largest singular value of an ill-posed operator is much larger than its smallest singular value. Thus, the condition number of an ill-posed operator, defined as the ratio of the maximum singular value to the minimum singular value, can be extremely large [27, 80]. It should also be noted that [27]

$$\text{If } A \in \mathbb{C}^{n \times m} \implies \begin{cases} U \in \mathbb{C}^{n \times m} \\ \Sigma \in \mathbb{R}^{m \times m} \\ V \in \mathbb{C}^{m \times m} \end{cases} \quad (5.4)$$

Introducing (5.2) into $Ax = b$, we have

$$U\Sigma V^H x = b \quad (5.5)$$

Multiplying both sides of (5.5) with U^H , we have

$$U^H U \Sigma V^H x = U^H b \quad \xrightarrow[\substack{U \text{ is orthonormal matrix} \\ U^H U = U U^H = I}]{\quad} \Sigma V^H x = U^H b \quad (5.6)$$

Multiplying with the inverse of Σ gives

$$\Sigma^{-1} \Sigma V^H x = \Sigma^{-1} U^H b \quad \xrightarrow{\Sigma^{-1} \Sigma = \Sigma \Sigma^{-1} = I} \quad V^H x = \Sigma^{-1} U^H b \quad (5.7)$$

Finally, if we multiply both sides of (5.7) with V , we find x as

$$V V^H x = V \Sigma^{-1} U^H b \quad \xrightarrow[\substack{V \text{ is orthonormal matrix} \\ V^H V = V V^H = I}]{\quad} \quad x = V \Sigma^{-1} U^H b \quad (5.8)$$

Noting that the Σ is a diagonal matrix, the inverse of this matrix will be

$$\Sigma^{-1} = \begin{pmatrix} \frac{1}{\sigma_1} & 0 & \cdots & 0 & 0 \\ 0 & \frac{1}{\sigma_2} & 0 & \cdots & 0 \\ \vdots & 0 & \frac{1}{\sigma_3} & \ddots & \vdots \\ 0 & \ddots & \ddots & \ddots & 0 \\ 0 & 0 & \cdots & 0 & \frac{1}{\sigma_m} \end{pmatrix} \quad (5.9)$$

Therefore, (5.8) can be written as [27, 80]

$$x = \sum_{i=1}^m \frac{u_i^H b}{\sigma_i} v_i \quad (5.10)$$

The above equation shows that the solution x is the superposition of the right singular vectors, each of which is weighted by weighting coefficients. The weighting coefficients are dependent on the left singular vectors, the measured data vector b ,

and the singular values. It should be noted that the measured data vector b consists of two parts: (1) the true value (noiseless) of the measured data, and (2) the error due to the measurement noise and the numerical noise (round-off error). These two parts, the true value and the noise term, are not separable. We just assume that they are separable to explain the concept of regularization. Thus, the measured data vector can be written as

$$b = b^{\text{exact}} + e \quad (5.11)$$

where b^{exact} is the true value (noiseless) of the measurements and e is the error due to the measurement noise or numerical error. Substituting (5.11) into (5.10), we have

$$x = \sum_{i=1}^m \frac{u_i^H b^{\text{exact}}}{\sigma_i} v_i + \sum_{i=1}^m \frac{u_i^H e}{\sigma_i} v_i \quad (5.12)$$

Note that the denominator in both of these summations goes to zero or is very small for large values of the summation index i . However, the numerator of the first term in (5.12), i.e., $u_i^H b^{\text{exact}}$, goes to zero faster than its denominator [27, 75]. This is usually referred to as the discrete Picard condition [27, 80, 83]. Therefore, there is no stability problem with the first summation term of (5.12). However, in the second term of (5.12), the numerator value does not change significantly as the summation index i increases. This can be understood by thinking of e as white noise and $u_i^H e$ can be thought of as different spatial frequencies of the white noise, which should be the constant [83]. Thus, the numerator of the second term does not change that much. On the other hand, the denominator of the second summation term becomes smaller and smaller when i increases. This results in the "blow-up" of the second summation term, which ultimately results in the "blow-up" of the solution x . This explains why a small change in the measured data, in this case due to the noise e , can result in a

huge change in the solution. In what follows, regularization methods to handle this instability issue are described. If implemented correctly, these regularization methods can stabilize the solution and aid its convergence.

5.3 Truncated Singular value Decomposition

One way to handle the stability problem is to not include all of the singular values in the SVD of A . To this end, we truncate the summation in (5.12) to filter out small singular values that make the denominator go to zero faster than the numerator. Thus, instead of using m in (5.12), we choose k as the truncation index [27, 75, 80]. Thus, we have

$$x = \sum_{i=1}^k \frac{u_i^H b^{\text{exact}}}{\sigma_i} v_i + \sum_{i=1}^k \frac{u_i^H e}{\sigma_i} v_i \quad 1 \leq k < m \quad (5.13)$$

and the method is called TSVD. The choice of k plays an important role in regularization; it becomes the regularization parameter. This is due to the fact that if k is chosen to be a large number, close to m , then the denominator can go to zero faster than the numerator, blowing up the solution. On the other hand, if k is chosen to be small, the denominator doesn't go to zero but the solution will be overly smooth and we lose resolution. Therefore, k needs to be chosen in such a way that we have a proper balance between these two situations.

5.4 Tikhonov Regularization

Tikhonov regularization [22, 26–29] is probably the most popular regularization method. We will now explain how this regularization method works, and compare it with the TSVD method. First, note that x , the solution of $Ax = b$, can be found

using the following minimization [79]:

$$x = \arg \min_x \{ \|Ax - b\|_2^2 \} \quad (5.14)$$

However, due to the ill-posedness of the operator A , such an approach will be unstable and lead to the wrong answer. Tikhonov regularization adds one more terms to the cost functional, the two-norm of the solution [27, 28]. This term is usually called the penalty term or the regularization term [30]. Thus, we now have the following regularized cost functional

$$x_\lambda^{\text{tikhonov}} = \arg \min_x \{ \|Ax - b\|_2^2 + \lambda^2 \|Lx\|_2^2 \} \quad (5.15)$$

where $\lambda \in \mathbb{R}^+$ is a regularization parameter and L is a matrix that operates on x . $x_\lambda^{\text{tikhonov}}$ is the solution using Tikhonov regularization for the regularization parameter λ . The Tikhonov cost functional, C^{Tikhonov} , is the summation of the data misfit cost functional $\|Ax - b\|_2^2$ and a regularization term with an appropriate weight λ^2 ; i.e.,

$$C^{\text{Tikhonov}} \triangleq \|Ax - b\|_2^2 + \lambda^2 \|Lx\|_2^2 \quad (5.16)$$

To solve (5.15), we may write it in the following equivalent form [84]

$$x_\lambda^{\text{tikhonov}} = \arg \min_x \left\{ \left\| \begin{pmatrix} A \\ \lambda L \end{pmatrix} x - \begin{pmatrix} b \\ \underline{0} \end{pmatrix} \right\|_2^2 \right\} \quad (5.17)$$

where $\underline{0}$ is the zero vector of appropriate size. (This equivalent form is sometimes referred to as the damped least squares problem [85, 86].) The minimization shown

in (5.17) is equivalent to the following equation.

$$\begin{pmatrix} A \\ \lambda L \end{pmatrix} x = \begin{pmatrix} b \\ \underline{0} \end{pmatrix} \quad (5.18)$$

Multiplying both sides of (5.18) with the Hermitian of the first term, we will have

$$\begin{pmatrix} A \\ \lambda L \end{pmatrix}^H \begin{pmatrix} A \\ \lambda L \end{pmatrix} x = \begin{pmatrix} A \\ \lambda L \end{pmatrix}^H \begin{pmatrix} b \\ \underline{0} \end{pmatrix} \quad (5.19)$$

or

$$\begin{pmatrix} A^H & \lambda L^H \end{pmatrix} \begin{pmatrix} A \\ \lambda L \end{pmatrix} x = \begin{pmatrix} A^H & \lambda L^H \end{pmatrix} \begin{pmatrix} b \\ \underline{0} \end{pmatrix} \quad (5.20)$$

Thus, we have

$$(A^H A + \lambda^2 L^H L)x = A^H b \quad (5.21)$$

In Tikhonov regularization, L is usually chosen to be the identity matrix ($L = I$) [27].

If we assume that $L = I$, then (5.21) will be

$$(A^H A + \lambda^2 I)x = A^H b \quad (5.22)$$

Therefore, in Tikhonov regularization, we effectively solve the above equation instead of solving $Ax = b$. The diagonal elements of $A^H A$ are modified by adding λ^2 to all of them. This will produce a regularized (stable) solution for our problem. As can be seen if $\lambda \rightarrow 0$, the Tikhonov solution will be least square solution of $Ax = b$.

Now the main challenge is how to choose the regularization parameter. In practice, it is usually chosen using either ad hoc techniques or more sophisticated regularization parameter choice methods such as the generalized cross validation [27,55] and L-curve

methods [27, 80, 87].

We now show how the Tikhonov regularization can stabilize the solution. To this end, take the SVD of A and A^H [27, 75, 80]. The SVD of A^H can be found as

$$A^H = \left(U \Sigma V^H \right)^H = V \Sigma^H U^H \xrightarrow[\text{diagonal matrix}]{\Sigma \text{ is a real}} A^H = V \Sigma U^H \quad (5.23)$$

Therefore, (5.22) can be written as

$$[V \Sigma U^H U \Sigma V^H + \lambda^2 I] x = V \Sigma U^H b \quad (5.24)$$

or

$$[V \Sigma I \Sigma V^H + V \text{diag}(\lambda^2) V^H] x = V \Sigma U^H b \quad (5.25)$$

where $\text{diag}(\lambda^2)$ is a diagonal matrix having the square of the regularization parameter as its diagonal elements. Factoring the V on the left and right sides of (5.25), we have

$$V \text{diag}(\sigma_i^2 + \lambda^2) V^H x = V \Sigma U^H b \quad (5.26)$$

Therefore, x can be found as

$$x = V \text{diag}\left(\frac{\sigma_i}{\sigma_i^2 + \lambda^2}\right) U^H b \quad (5.27)$$

or, more informatively, as [27, 75]

$$x = \sum_{i=1}^m \frac{\sigma_i}{\sigma_i^2 + \lambda^2} u_i^H b v_i = \sum_{i=1}^m \frac{\sigma_i^2}{\sigma_i^2 + \lambda^2} \frac{u_i^H b}{\sigma_i} v_i \quad (5.28)$$

Comparing (5.28) with the first term of (5.12), it can be seen that we have an extra multiplicative factor. This new multiplicative factor has a similar role as k in the

TSVD method. To understand this, let's have a closer look at this factor. For small values of i , the corresponding singular values are larger than the regularization parameter (i.e., $\lambda \ll \sigma_i$). Therefore [27, 75],

$$\frac{\sigma_i^2}{\sigma_i^2 + \lambda^2} \xrightarrow[\lambda \ll \sigma_i]{\text{for the small } i} \frac{\sigma_i^2}{\sigma_i^2 + \lambda^2} \approx 1 \quad (5.29)$$

Therefore, when i is small, this extra multiplicative term is approximately one, and thus has no effect. As i increases, the corresponding singular values become smaller and smaller (i.e., $\sigma_i \rightarrow 0$) as shown in (5.3). Therefore, eventually, $\sigma_i \ll \lambda$, and the multiplicative term in (5.28) goes to zero, effectively truncating the summation. Concisely, we can write [27, 75]

$$\frac{\sigma_i^2}{\sigma_i^2 + \lambda^2} \xrightarrow[\sigma_i \ll \lambda]{i \nearrow} \frac{\sigma_i^2}{\sigma_i^2 + \lambda^2} \approx 0 \quad (5.30)$$

Comparing Tikhonov regularization with the TSVD, we see that whereas TSVD truncates the summation at a chosen k to prevent the blow-up of the solution, Tikhonov regularization method uses the extra multiplicative term $\sigma_i^2/(\sigma_i^2 + \lambda^2)$ to handle the instability. This extra multiplicative factor filters out the high spatial frequency information which corresponds to small singular values. As can be seen, both Tikhonov and TSVD regularization are almost doing the same thing: they both dampen the high spatial frequency information to prevent instability.

Now, the main question is that if they are the same in terms of effect, why would one use Tikhonov regularization. The reason is that Tikhonov regularization is computationally more efficient than the TSVD method for two reasons: (1) Tikhonov regularization does not require one to calculate the SVD of the matrix A whereas the TSVD method does. In Tikhonov regularization, we simply solve (5.18) using an

iterative technique such as the conjugate gradient algorithm. This is important as the computational complexity of the conjugate gradient algorithm is $\mathcal{O}(n^2)$ whereas the computational complexity of the SVD is $\mathcal{O}(n^3)$. (2) Tikhonov regularization does not need the full storage of the matrix A , it just needs the operation of A and A^H on vectors of appropriate size whereas the TSVD method requires the full storage of the matrix A in order to find its SVD.

It should be noted that the choice of λ is crucial for Tikhonov regularization. This is due to the fact that when λ is too big (it is equivalent to using a small k in TSVD), we are far from the exact solution because too much information will be lost. Thus, the residual error ($Ax_\lambda^{\text{tikhonov}} = b$) will be large. However, if λ is too small (it is equivalent to using a large k in TSVD), the residual error will be a small number but there is chance that before $\sigma_i^2/(\sigma_i^2 + \lambda^2) \rightarrow 0$, the denominator goes to zero and the solution blows up; thus, having an extremely large value for $\|x\|_2^2$. Therefore, a good choice of λ is really important in Tikhonov regularization. Several techniques are proposed to find the regularization parameter such as the L-curve method [27, 87], or Generalized Cross Validation (GCV) [55].

5.5 CGLS Regularization

Krylov subspace methods, such as conjugate gradients for least squares (CGLS), least squares with QR factorization (LSQR), and the general minimum residual method (GMRES), solve the least squares problem by iteratively projecting the solution into the Krylov subspace. To see how they work, we first define the Krylov subspace. Assume we have a matrix $A \in \mathbb{R}^{n \times n}$ and a vector $b \in \mathbb{R}^n$, then the Krylov subspace of order k ($k \leq n$) associated with this matrix and vector, denoted by

$\mathcal{K}_k(A, b)$, is equal to [27, 88]

$$\mathcal{K}_k(A, b) = \text{span} \{b, Ab, A^2b, \dots, A^{k-1}b\} \quad (5.31)$$

That is, the Krylov subspace of order k is the space that can be spanned by vectors $b, Ab, \dots, A^{k-1}b$.

Now, assume that we want to solve $Ax = b$ using the CGLS method which is a Krylov subspace method. At each iteration of the CGLS algorithm, the solution is projected into a Krylov subspace constructed by A and b . In early iterations of the CGLS, the order of the subspace is small; however, as the number of CGLS iterations increases the order of the Krylov subspace increases. For example, in an early CGLS iteration, the solution might be projected into $\text{span} \{b, Ab, A^2b\}$. However, after a few more iterations, the solution is now projected on to $\text{span} \{b, Ab, A^2b, A^3b, A^4b, A^5b\}$. As the CGLS iteration number increases, the order of the Krylov subspace increases until the final solution is sufficiently accurate. At that point, the CGLS method is terminated.

Note that our current discussion is in the framework of solving $Ax = b$ when A is a well-posed matrix. The discussion on how to use this method as a regularizer will come later. The other thing that needs to be addressed is what happens if the matrix is not square, for example when $A \in \mathbb{R}^{m \times n}$ and $b \in \mathbb{R}^m$. In this case the Krylov subspace associated with this pair will span [83, 88]

$$\mathcal{K}_k(A^T A, A^T b) = \text{span} \{A^T b, (A^T A)A^T b, (A^T A)^2 A^T b, \dots, (A^T A)^{k-1} A^T b\} \quad (5.32)$$

Now, let's see what is the concept behind the Krylov subspace methods. When the order of the Krylov subspace is small, it is only spanned by vectors containing

low spatial frequencies. However, as the order of Krylov subspace increases, it is spanned by vectors containing high spatial frequencies. That is, when applying a Krylov subspace method such as the CGLS method to $Ax = b$ to solve for x , the method first constructs the low spatial frequency components of x . As the CGLS iterations continue, higher spatial frequency components of x will be constructed. After sufficient spatial frequency components of x have been constructed, the solution x will be said to have sufficient accuracy, and the CGLS method is terminated.

Given this basic concept of how the Krylov subspace method solves $Ax = b$ for a well-posed matrix A , we describe a regularization scheme to solve $Ax = b$ when A is an ill-posed matrix. Recall that in the TSVD method, the solution is projected onto a set of right singular vectors, but not all of the right singular vectors are used. In fact, we terminated the expansion of the solution in terms of right singular vectors at an appropriate index k . This was based on the fact that the singular vectors corresponding to the larger singular values contain low spatial frequency information, however as the index of right singular vectors increases, they contain more high spatial frequency information [89]. This is very similar to the methodology of a Krylov subspace method. As in TSVD we will need to truncate the Krylov subspace method before reaching high spatial frequency components which will make the solution unstable. Recall that the TSVD regularized solution is expanded in terms of the right singular vectors, v_i , as

$$x = \sum_{i=1}^k \frac{u_i^H b}{\sigma_i} v_i \quad (5.33)$$

with coefficients given by the inner-product of the corresponding left singular vector with the RHS divided by singular value. As can be seen, the summation is truncated at the index k . That is, we do not allow our regularized solution x to be spanned by right singular vectors $v_{i>k}$. In other words, the TSVD regularized solution is spanned

by

$$x_{TSVD} = \text{span} \{v_1, v_2, \dots, v_k\} \quad (5.34)$$

Now, we can do the same thing using the Krylov subspace method. The whole idea is that we need to terminate the Krylov subspace method, for example, the CGLS method, before $\|Ax - b\|$ is minimized so that the solution remains stable. To achieve this regularized solution, we minimize $\|Ax - b\|$ under the constraint $x \in \mathcal{K}_k(A^T A, A^T b)$. Limiting the solution to lie within $\mathcal{K}_k(A^T A, A^T b)$ produces the regularized solution of the problem to order k . The challenge with this method is how to choose an appropriate k (Krylov subspace order). This is similar to the challenge that we have in finding the termination index of the TSVD method.

This CGLS regularization technique has been used for microwave tomography applications [24, 25]. To apply this technique to the UT problem considered herein, we use the *ad hoc* method of finding k proposed in [24]. In this *ad hoc* method, the termination index is chosen to be small in the early iterations of the BIM, and as the BIM gets closer to the solution, the termination index k increases. This is consistent with the concept of adaptive regularization [90] for nonlinear ill-posed problems. In adaptive regularization, the regularization weight is changed at each iteration of the optimization algorithm. It is chosen to be large in early iterations of the optimization algorithm, and is reduced as one gets closer to the solution. In our case, the termination index acts as the regularization weight: the smaller the Krylov subspace, and therefore, the larger the regularization effect.

The CGLS algorithm is shown as Algorithm 5.1 [91]. In this algorithm, the contrast profile vector, x , is a real column vector of length $3N$ where the first N elements correspond to the real part of the contrast of compressibility after applying a balancing method (χ_{1r}^{cn}). The second N elements of this vector correspond to the imaginary

part of the contrast of compressibility after applying the balancing method (χ_{1i}^{cn}), and the last N elements correspond to the contrast of inverse density after applying the balancing method (χ_{2r}^n). In the single frequency case, when operator A operates on this real $3N$ contrast profile vector, the results of this operation will be a real vector of size $2 \times nRx \times nTx$ where the first $nRx \times nTx$ elements of this real vector correspond to the real part of the scattered field and the next $nRx \times nTx$ elements correspond to the imaginary part of the scattered pressure. Thus, in the single frequency case, when operator A operates on the contrast profile, the first $nRx \times nTx$ elements of the resulting vector, which correspond to the real part of the scattered pressure, are found using (4.43). The next $nRx \times nTx$ elements of the resulting vector, which correspond to the imaginary part of the scattered pressure, are found using (4.44).

This procedure can be easily extended to the multiple-frequency case. In the multiple-frequency case, we have several A operators, each of which corresponds to one specific frequency. When each of these operates on an appropriate vector of length $3N$, the result will be a real vector of length $2 \times nRx \times nTx$. For simultaneous frequency inversion, we use the information of all frequencies at the same time. Therefore, after the corresponding operator for each frequency operates on an appropriate vector, the n_f resulting vectors, each being real vector of length $2 \times nRx \times nTx$, are concatenated into a single real vector of length $2 \times nRx \times nTx \times n_f$.

The adjoint operator, A^a , operates on a real $2 \times nRx \times nTx$ vector in the single-frequency case. The result of this operation is a real vector of length $3N$. The first, second and third set of N elements of this vector can be found using (4.57), (4.58), and (4.59) respectively. In the multiple-frequency case, when the adjoint operator operates on a real vector of length $2 \times nRx \times nTx \times n_f$, the result obtained by this operation is a real vector of length $3N$. Now let's consider how we can find the result,

a $3N$ -vector, of the operation of multi-frequency adjoint operator on a real vector of length $2 \times nRx \times nTx \times n_f$. To this end, A^a corresponding to the first frequency operates on the first $2 \times nRx \times nTx$ elements of the $2 \times nRx \times nTx \times n_f$ vector. The results of this operation using (4.57), (4.58), and (4.59) is a real $3N$ -vector. Then, A^a corresponding to the second frequency operates on the second $2 \times nRx \times nTx$ elements of the $2 \times nRx \times nTx \times n_f$ vector and the result of this operation using (4.57), (4.58), and (4.59) is another real $3N$ -vector. We continue this procedure for all the frequencies to find n_f different real vectors of length $3N$. These $3N$ -vectors are added to find the result of the operation of the multi-frequency adjoint operator.

It should be noted that the result, x , in Algorithm 5.1, obtained with the last iteration of the CGLS regularization method is a real $3N$ -vector where the first N elements correspond to the balanced version of the real part of the compressibility contrast profile, the second set of N elements to the balanced version of the imaginary part of the compressibility, and the last set of N elements to the balanced version of the inverse density contrast profile. To find the actual contrast values, the reciprocal of the balancing coefficients must be multiplied to each of these balanced profiles.

The procedure utilized in this thesis to find the contrast profiles, which is based on the BIM in conjunction with the CGLS regularization algorithm and the MoM forward solver, is shown in Appendix E.

Algorithm 5.1 CGLS Algorithm

Input: A , A^a , and b are known in $Ax = b$

Output: Finding x in $Ax = b$ using CGLS [91]

```

1:  $x^{(0)} = 0$  (starting vector)
2:  $r^{(0)} = b - Ax^{(0)}$ 
3:  $d^{(0)} = A^a r^{(0)}$ 
4: for  $k = 1, 2, \dots, K$  do ( $K$  is the number of CGLS iterations)
5:    $\alpha_k = \|A^a r^{(k-1)}\|_2^2 / \|Ad^{(k-1)}\|_2^2$  ( $\alpha_k$  is scalar)
6:    $x^{(k)} = x^{(k-1)} + \alpha_k d^{(k-1)}$ 
7:    $r^{(k)} = r^{(k-1)} - \alpha_k Ad^{(k-1)}$ 
8:    $\beta_k = \|A^a r^{(k)}\|_2^2 / \|A^a r^{(k-1)}\|_2^2$  ( $\beta_k$  is scalar)
9:    $d^{(k)} = A^a r^{(k)} + \beta_k d^{(k-1)}$ 
10: end for

```

6

Results

In this section, the inversions of noisy synthetic and measured data are obtained using the BIM in conjunction with the CGLS regularization method. As explained in the previous chapters, the goal in this thesis is to simultaneously reconstruct the real part of the complex contrast of compressibility (χ_{1r}^c), the imaginary part of the complex contrast of compressibility (χ_{1i}^c), and the contrast of inverse density (χ_2) from time-harmonic scattered pressure data. The effects of the balancing method in the reconstruction algorithm and the use of multiple-frequency data sets, both of which are utilized to improve the reconstruction results, are also discussed.

6.1 Synthetic Results

In this section, we use synthetic measured scattered data with added noise to reconstruct the contrast profiles of various OIs. We attempt to reconstruct different types of OIs such as a cylinder, two cylinders having the same contrast profiles, two cylinders with different contrast profiles and a breast model. It should be noted that these examples represent the so-called large-domain inverse problems as the size of the imaging domain is large compared to the wavelength of operation. Also, the discretization mesh used to obtain the synthetic scattered pressure is different from

the meshes used in the inversion algorithm in all the examples so as to avoid the so-called inverse crime. In all the following examples, the background medium (matching fluid) is chosen to be water. Therefore, the background density and the background speed of the sound are set to $\rho_b = 1000[\frac{\text{kg}}{\text{m}^3}]$ and $c_b = 1483[\frac{\text{m}}{\text{s}}]$, respectively. The choice of water as a background medium for ultrasound biomedical tomography is appropriate as it is easily available, non-toxic, and makes the OI have a relatively low-contrast with respect to the background. This also means that more energy will be coupled into the OI.

6.1.1 Reconstruction of a cylinder

In this example, a cylinder with a radius of $1.7\lambda_{\min}$, and the contrasts of $\chi_1^c = 0.3 - j0.1$, and $\chi_2 = 0.1$ is enclosed by a $10\lambda_{\min} \times 10\lambda_{\min}$ imaging domain as shown in Fig 6.1. The number of receivers, nRx , and number of transmitters, nTx , used to reconstruct the contrast profiles are 80. To have more information about the OI, the scattering data are collected at multiple frequencies. The number of frequencies, n_f , and their exact values are

$$n_f = 6, \quad f = [250, 280, 310, 330, 360, 390] \text{ kHz}$$

We also add three percent noise to the synthetic data set (synthetic scattered pressure) using the following equation

$$p_{noisy}^{scat} = p_{simulated}^{scat} + (\text{Average value}) \times (\text{Noise Percentage}/\sqrt{2}) \times (\text{Random Vector}) \quad (6.1)$$

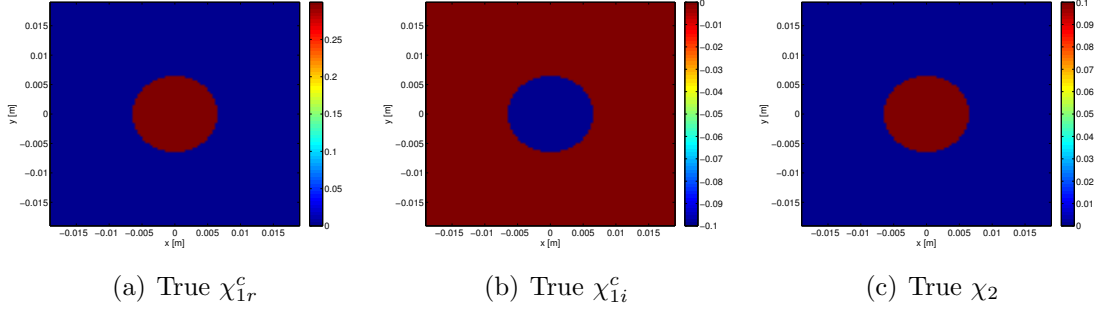


Figure 6.1: True contrast profiles: (a) the real part of compressibility contrast, (b) the imaginary part of compressibility contrast, and (c) the contrast of inverse density.

where

$$\text{Average value} = \overline{|p_{simulated}^{scat}|} \quad (6.2)$$

$$-1 < \text{Random Vector} < 1 \quad (6.3)$$

It is this noisy synthetic data set that our inversion algorithm inverts.

In this example, the BIM inversion algorithm took only 8 iterations to converge. The termination of the code is mainly based on having a data misfit cost function less than a specified number and having the difference between two successive data misfit cost function values less than a specified number. Also the number of the CGLS regularization iterations at each iteration of the BIM inversion algorithm has been chosen as 2, 4, 8, 18, 30, 50, 70, and 80 respectively. (Note that as we get closer to the solution, the number of CGLS iterations increases.) The data misfit at each iteration of the BIM inversion algorithm is shown in Table 6.1. The data misfit is defined as

$$\text{Data misfit} \triangleq \frac{\|p_{measured}^{scat} - p_{simulated}^{scat}\|_2}{\|p_{measured}^{scat}\|_2} \quad (6.4)$$

The results of the reconstruction of contrast profiles for the first, second, fourth,

Table 6.1: Data misfit for different iterations of the BIM inversion algorithm for the cylinder with a radius of $1.7\lambda_{min}$.

BIM Iteration Number	Number of CGLS Iterations	Data misfit
1	2	0.5837
2	4	0.1496
3	8	0.0533
4	18	0.0254
5	30	0.0202
6	50	0.0176
7	70	0.0148
8	80	0.0125

sixth, and eighth BIM iterations is shown in Fig 6.2. It should also be noted that the balancing factors in this example are all chosen to be unity: $Q_1 = Q_2 = Q_3 = 1$

It is instructive to compare the reconstruction result at the first BIM iteration with that at the last BIM iterations. The first iteration of the BIM represents the Born approximation, which is one of the most common linear inversion methods. Although the reconstruction result for the first BIM iteration provides a qualitative image of the OI, it totally fails at quantitatively estimating the acoustical properties of the OI. For example, the true value of χ_{1r}^c is 0.3. The reconstruction at the first BIM iteration estimates this to be about 0.07. On the other hand, the last iteration of the BIM, which represents a nonlinear inversion of this data set, estimates this value to be about 0.25.

6.1.2 Reconstruction of two cylinders

We now consider two cylinders each with a radius of $1.2\lambda_{min}$, and the contrast profiles of $\chi_1^c = 0.2 - j0.01$ and $\chi_2 = 0.05$ enclosed within a $10\lambda_{min} \times 10\lambda_{min}$ imaging domains as shown in Fig 6.3. The number of transmitters and receivers used in this example are 80. Six frequencies of operation, $f = [250, 280, 300, 320, 340, 360]$

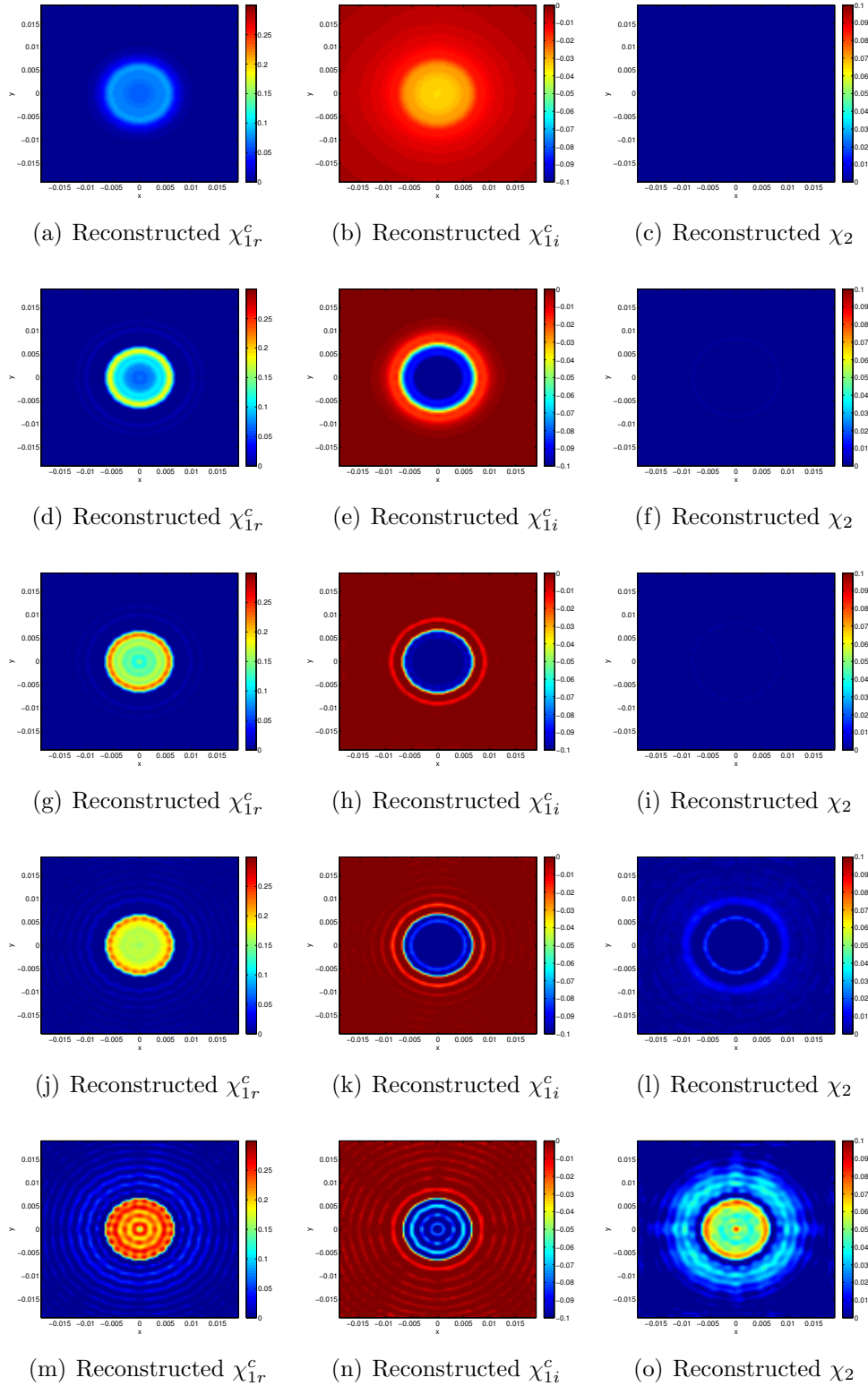


Figure 6.2: Simultaneous reconstruction of χ_{1r}^c and χ_2 for the cylinder data set with three percent noise. The first, second, third, fourth and fifth rows correspond to the reconstruction of the contrast profiles at the 1st, 2nd, 4th, 6th, and 8th iterations of the BIM respectively.

kHz, are used for the simultaneous frequencies inversion method. Note that the contrast profiles of this object are not within the same numerical range. Therefore, the balancing method is utilized to enhance the reconstruction. The balancing coefficients for this example are chosen to be

$$Q_1 = 1, \quad Q_2 = 0.1, \quad Q_3 = 0.2$$

Similar to the previous data set, three percent noise is added to the synthetic sim-

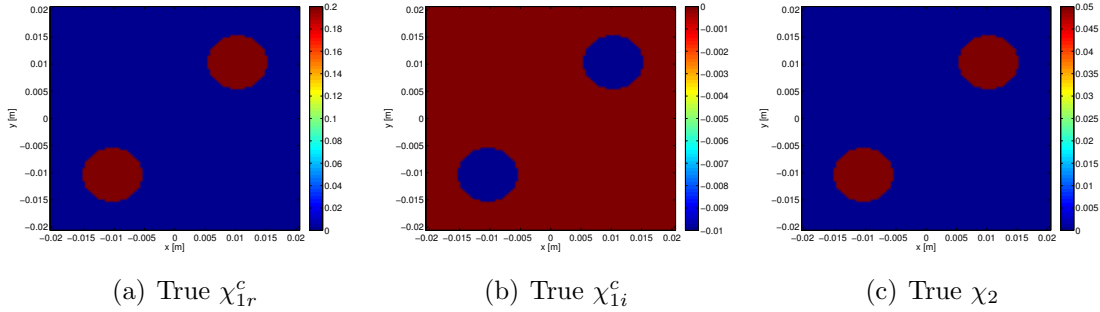


Figure 6.3: True value of contrast profiles for two identical cylinders. The size of the domain is $10\lambda_{\min} \times 10\lambda_{\min}$. (a) the real part of the contrast of compressibility (b) the imaginary part of contrast of compressibility and (c) the contrast of inverse density.

ulated data using (6.1). For this example, the BIM converged at the 11th iteration. The number of CGLS iterations at each iteration of the BIM inversion algorithm was set to 2, 4, 18, 30, 50, 60, 80, 100, 120, 140, and 160 respectively. As for the first data set, note that the number of CGLS iterations is allowed to increase as we get closer to the solution. The data misfit at each iteration of the BIM is shown in Table 6.2. The results of the reconstruction of the contrast profiles for the 1st, 3rd, 5th, 7th and 11th iteration of the BIM are shown in Fig 6.4.

Again the linear inversion method, i.e., the first iteration of the BIM, provides a reasonable qualitative reconstruction but totally fails to provide a reasonable quanti-

tative reconstruction for the OI. For example, the linear inversion estimates the value of χ_{1r}^c to be about 0.09 whereas the nonlinear inversion estimates the same value to be about 0.18. As the true value is 0.20, it can be seen that nonlinear inversion outperforms the linear inversion at the cost of requiring more computation. The other thing that needs to be emphasized here is that it is usually stated that linear inversion is sufficient for low contrast profiles. But, as can be seen in this low contrast example, linear inversion is not successful at accurately reconstructing the quantitative information. This is due to the fact that the size of the object is large compared to the wavelength. Noting that the wavelength in UT is usually very small, most OIs will be large objects compared to the wavelength of operation.

If we add more noise to the data set, we will require more regularization to prevent the blow-up of the solution. That is, for example, k should be chosen a smaller number in the TSVD method, λ should be chosen a larger number in the Tikhonov regularization method, and the number of CGLS iterations should be decreased. One way to add more noise to the data set is to add three percent noise using the maximum value instead of the average value in (6.1). The reconstruction results of the contrast profiles for this higher noise case are shown in Fig 6.5. In this case, the BIM converges after only four iterations. As can be seen, with more noise added, the BIM converges with fewer iterations. The number of CGLS iterations used at each iteration of the BIM was 2, 4, 18, 30. In this case the number of CGLS iterations were fewer as compared to that lower noise case. Note that adding more noise adversely affects the quality of the reconstruction of the inverse density compared to the contrast of compressibility. It was generally found that the density contrast was more difficult to reconstruct.

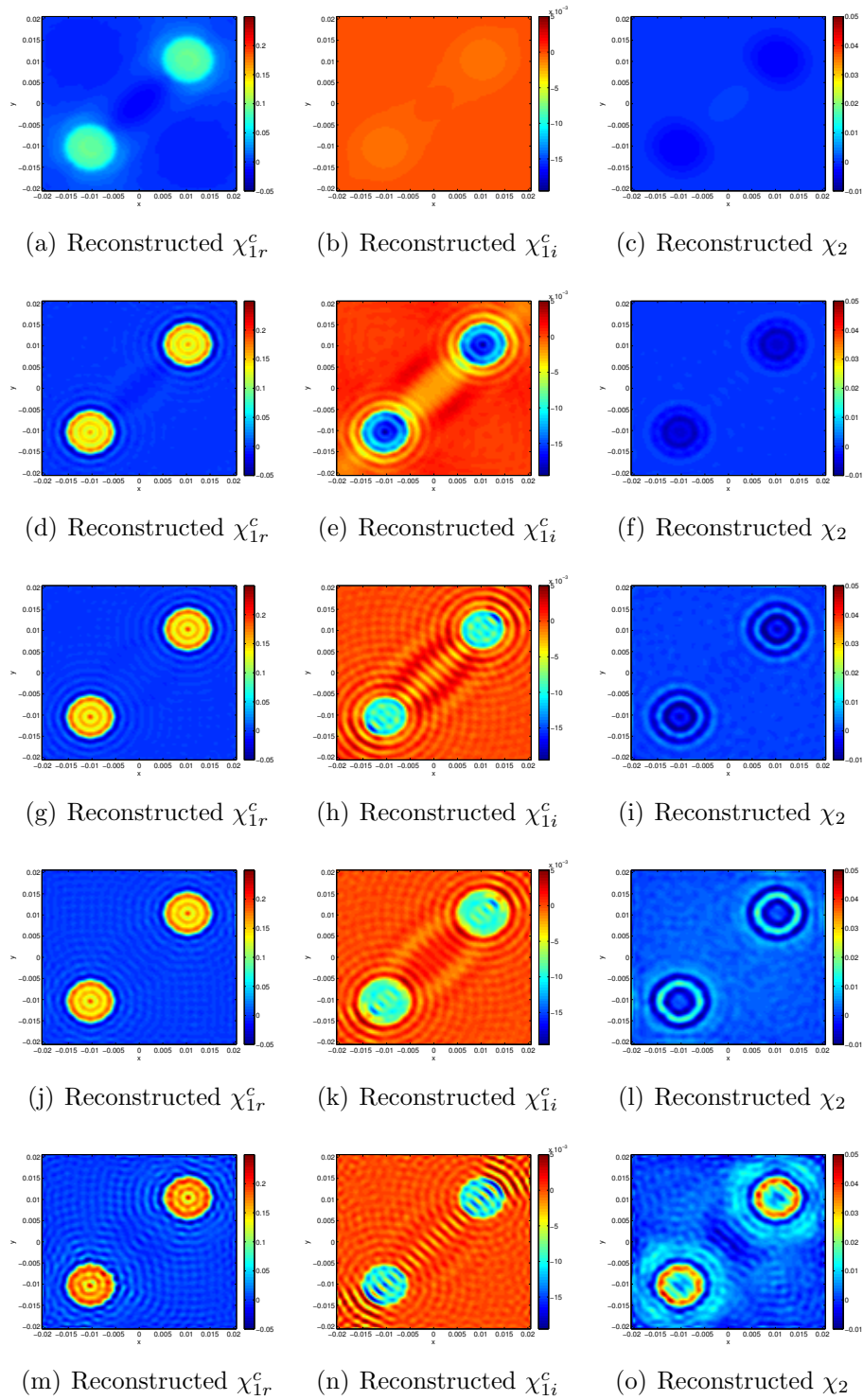


Figure 6.4: Simultaneous reconstruction of χ_1^c and χ_2 for the two cylinder data set with 3% noise based on the average value. The first, second, third, fourth and fifth rows correspond to the reconstruction of contrast profiles for the 1st, 3rd, 5th, 7th and 11th iterations of the BIM inversion algorithm respectively.

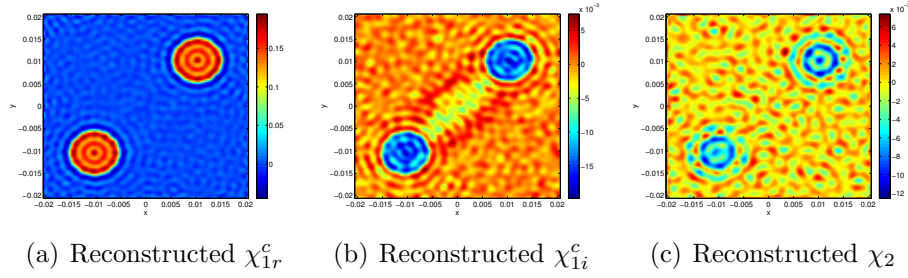


Figure 6.5: Simultaneous reconstruction of χ_1^c and χ_2 for the two cylinder data set with three percent noise using the maximum value.

Table 6.2: Data misfit for different iterations of the BIM inversion algorithm for the case that the OI is two cylinders with the same contrast profiles. Three percent noise is added and also balancing coefficients are applied.

BIM Iteration Number	Number of CGLS Iterations	Data misfit
1	2	0.0392
2	4	0.0188
3	18	0.0152
4	30	0.0137
5	50	0.0121
6	60	0.0112
7	80	0.0107
8	100	0.0104
9	120	0.0103
10	140	0.0101
11	160	0.0102

Table 6.3: Data misfit for different iterations of the BIM inversion algorithm for two cylinders without applying a balancing method.

BIM Iteration Number	Number of CGLS Iterations	Data misfit
1	2	0.389
2	4	0.1268
3	18	0.0471
4	30	0.0355
5	50	0.0229
6	80	0.0167
7	110	0.0127
8	130	0.0101
9	150	0.0112

6.1.3 Two Cylinders Without Applying Balancing Method

To have a better understanding of the effect of the balancing method on the reconstruction of the contrast profiles, the reconstruction of the previous target was performed without applying the balancing method. That is the balancing factors were set to $Q_1 = Q_2 = Q_3 = 1$.

The data misfit for different iterations of the BIM is shown in Table 6.3. The true solution is shown in Fig 6.3. The results of the reconstruction of the contrast profiles for the 1st, 3rd, 5th, 6th and 9th iteration of the BIM are shown in Fig 6.6. Comparing to Fig 6.4, it can be concluded that when the contrast profiles are not in the same range, we will only have a good reconstruction for the dominant contrast profile. That is, contrast profiles which are very small compared to the dominant contrast profile are difficult to reconstruct without applying a balancing method. In this example, χ_{1i}^c and χ_2 are more difficult to reconstruct due to this imbalance. Applying a balancing method normalizes all the contrast profiles to be within the same numerical range and a better reconstruction for all the contrast profiles is obtained.

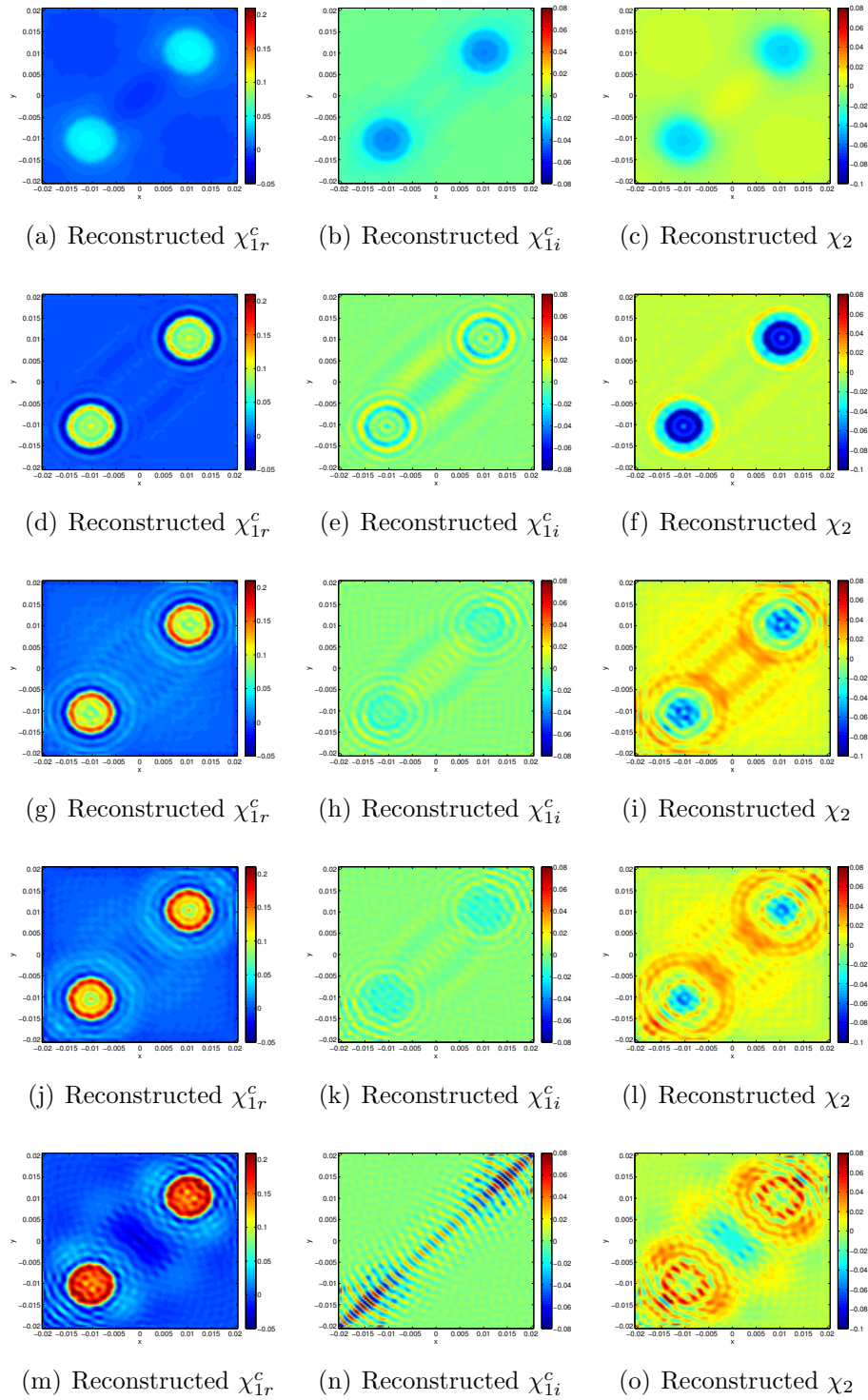


Figure 6.6: Simultaneous reconstruction of χ_1^c and χ_2 for two cylinders without applying the balancing method. The first, second, third, fourth and fifth rows correspond to the reconstruction of contrast profiles for the 1st, 3rd, 5th, 6th and 9th iterations of the BIM, respectively.

6.1.4 Two-cylinders reconstruction with reduced information

In this section, we show the importance of having sufficient information about the OI for the reconstruction of the contrast profiles. To this end, we show the reconstruction of the two cylinders shown in Fig 6.3 using less information as compared to those reconstructions reported in Fig 6.4. As a reminder, this example considers two cylinders with a radius of 1.2λ , $\chi_1^c = 0.2 - j0.01$, and $\chi_2 = 0.05$ within a $10\lambda \times 10\lambda$ imaging domain. The balancing coefficients have been chosen to be

$$Q_1 = 1, \quad Q_2 = 0.1, \quad Q_3 = 0.2$$

As already explained in the previous chapters, there are two common ways to have more information about the OI: (1) increasing the number of transmitters and receivers, and (2) using multiple frequency data sets. Thus, to reduce the amount of information about the OI in this example, only a single frequency ($f = 250\text{kHz}$) is used and also the number of transmitters and receivers have been reduced to 30. BIM converges after six iterations; the number of CGLS iterations at each iteration is 2, 4, 18, 30, 50, 80. The data misfit for different iterations of the BIM is shown in Table 6.4. The reconstruction of χ_{1r}^c , χ_{1i}^c , and χ_2 for the first, second, third, fifth and sixth iterations of the BIM inversion algorithm are shown in Fig 6.7. As can be seen in Fig 6.7, we have poor reconstruction of the contrast profiles compared to the results obtained using multiple frequency data shown in Fig 6.4. This is expected as the amount of information about the OI used for the reconstruction is much smaller than the total number of unknowns.

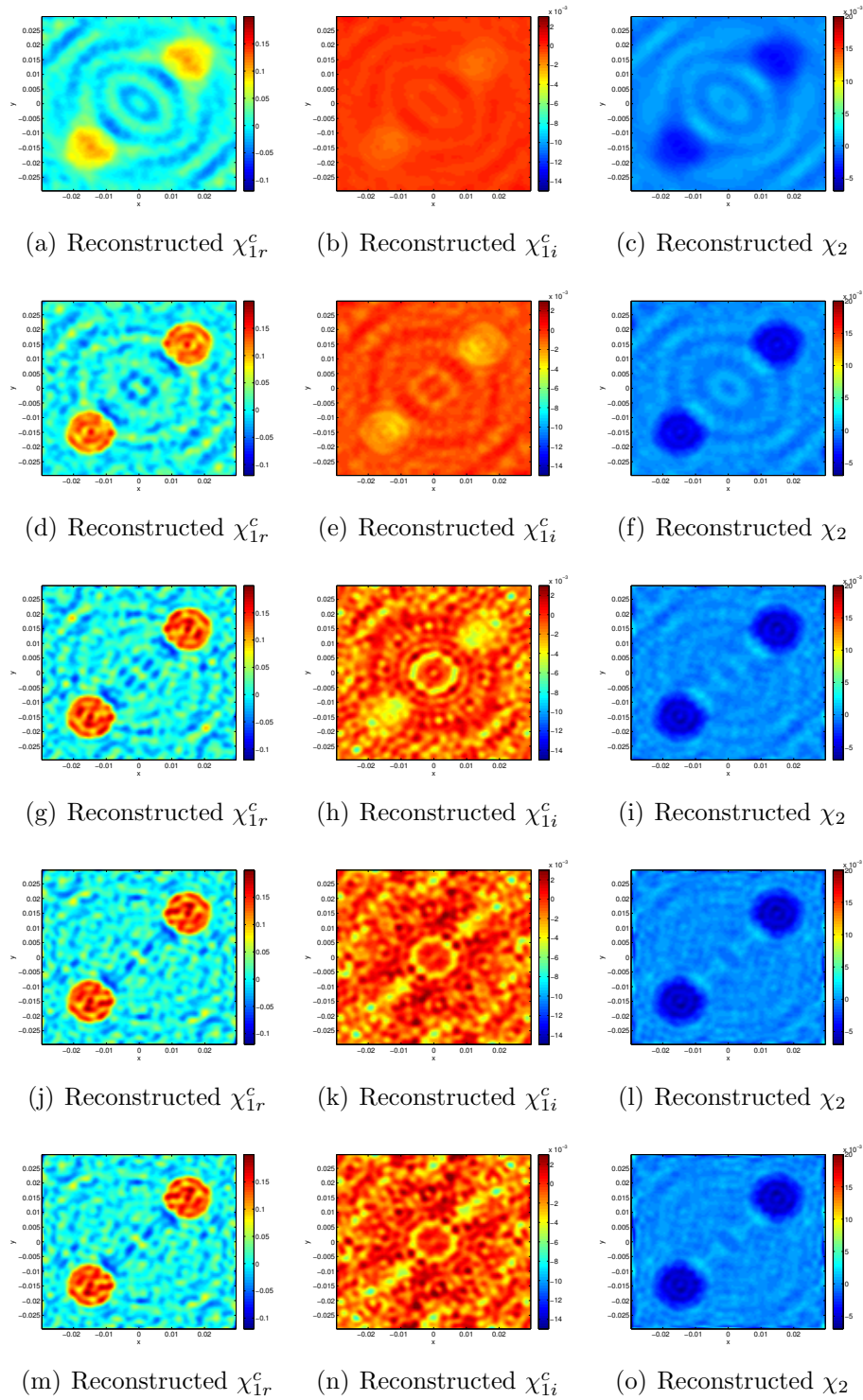


Figure 6.7: Simultaneous reconstruction of χ_1^c and χ_2 for two cylinders using a single-frequency data set. The first, second, third, fourth, and fifth rows correspond to the reconstruction of contrast profiles for the 1st, 2nd, 3rd, 5th and 6th iterations of the BIM, respectively.

Table 6.4: Data misfit for different iterations of the BIM inversion algorithm for two cylinders using a single frequency.

BIM Iteration Number	Number of CGLS Iterations	Data misfit
1	2	0.5
2	4	0.1276
3	18	0.0257
4	30	0.0098
5	50	0.0039
6	80	0.0016

6.1.5 Two cylinders with different contrast profiles

In this example, two cylinders with different contrast profiles are enclosed within a $10\lambda_{\min} \times 10\lambda_{\min}$ imaging domain. The number of transmitters and receivers used in this example are 90. Six frequencies between 250 kHz and 360 kHz are used with the simultaneous frequency inversion method. The simulated scattered pressure is contaminated with three percent (average) noise using (6.1). The following balancing factors are used

$$Q_1 = 1, \quad Q_2 = 0.1, \quad Q_3 = 0.2$$

The true contrast profiles are shown in the first row of Fig 6.8. The reconstruction of the contrast profiles for the first, fourth and eleventh iterations of the BIM are shown in the second, third and fourth row of Fig 6.8 respectively. The number of CGLS iterations in the first, fourth and eleventh iterations of the BIM are 2, 40 and 250 respectively.

The results of the comparison between the exact value of contrast profiles with the reconstructed contrast profiles for the elements on the antidiagonal from the bottom left corner to the top right containing both cylinders are shown in Fig 6.9. The first, second and third row of Fig 6.9 correspond to the first, fourth and eleventh iterations of the BIM. Note that since the discretization mesh for the true profiles and the

Table 6.5: Residual error for each contrast profile with respect to the exact value of contrast profile for the case that the OI is two cylinders with different contrast profiles. These values for each iteration of the BIM are shown below.

BIM Iteration	$\ \chi_{1r}^c(\text{Exact}) - \chi_{1r}^c(\text{Simu})\ _2$	$\ \chi_{1i}^c(\text{Exact}) - \chi_{1i}^c(\text{Simu})\ _2$	$\ \chi^2(\text{Exact}) - \chi^2(\text{Simu})\ _2$
	$\ \chi_{1r}^c(\text{Exact})\ _2$	$\ \chi_{1i}^c(\text{Exact})\ _2$	$\ \chi^2(\text{Exact})\ _2$
1	0.6429	0.9776	1.0533
2	0.3918	0.9082	1.0819
3	0.3601	0.3754	1.0785
4	0.3332	0.2414	1.0655
5	0.3187	0.2194	1.0027
6	0.3047	0.2188	0.8753
7	0.3012	0.2193	0.7950
8	0.2943	0.2148	0.6832
9	0.2970	0.2133	0.6070
10	0.3021	0.2204	0.5484
11	0.3167	0.2192	0.4915

reconstructed profiles are different, we need to use an interpolation scheme to compare the reconstructed profiles with the true profiles. Herein, a linear interpolation scheme is used for this purpose. The error of each contrast profile with respect to the exact contrast profiles for different BIM iterations are shown in Table 6.5. This example confirms that the BIM is able to quantitatively reconstruct OIs with different contrast profiles.

6.1.6 Simple Synthetic Breast Model

In this section, we apply the inversion algorithm to a simple numerical breast model to reconstruct its contrast profiles. To this end, we assume that the background medium is water. The attenuation of the background medium for different frequencies is tabulated in [92]. In this example, it is assumed that the background attenuation

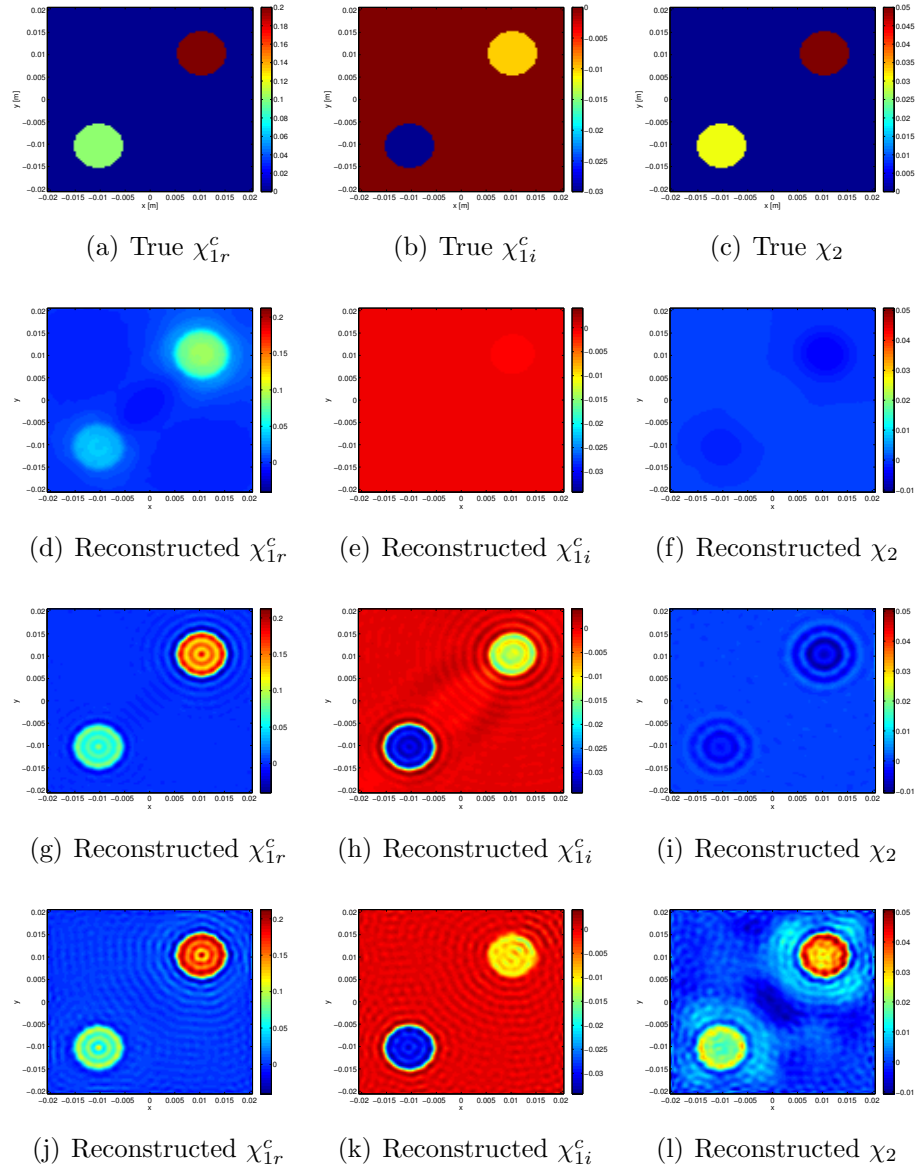


Figure 6.8: Simultaneous reconstruction of χ_1^c and χ_2 for two cylinders with different contrast profiles. The first row is the true value of the contrast profiles. The second, third and fourth rows correspond to the reconstruction of contrast profiles for the 1st, 4th and 11th iterations of the BIM respectively.

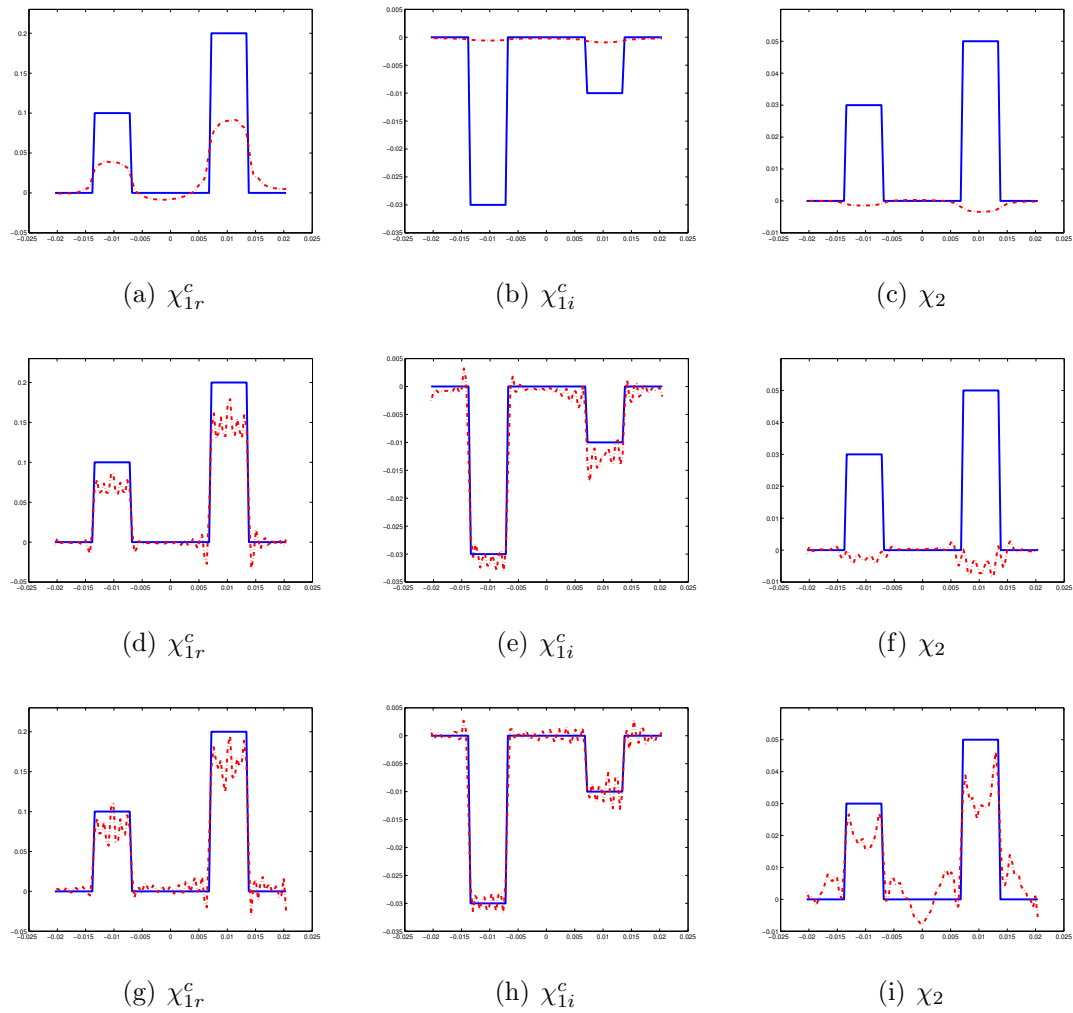


Figure 6.9: Antidiagonal cut from the bottom left corner to the top right for the case that the OI is two cylinders with different contrast profiles. The first, second and third rows correspond to the first, fourth and eleventh iterations of the BIM. The solid blue line corresponds to the actual contrast profiles and the dashed red line corresponds to the reconstructed contrast profiles

of the water is

$$\alpha_0 = 0.0022 \frac{\text{dB}}{\text{cm}}$$

It should be noted that the speed of the sound in water is dependent on the temperature of the water [93]. If the temperature of water is increased, the speed of the sound in the water will be increased [93]. If we assume that the temperature of the water in our model is 22°C , then the speed of sound in this background medium will be

$$c_b \simeq 1483 \frac{\text{m}}{\text{s}}$$

We also know that the density of the background is $\rho_b = 1000 \left[\frac{\text{kg}}{\text{m}^3}\right]$. Therefore, using (2.30), the compressibility of the background can be found. Thus, we have all the information about the background medium. We only need to know the acoustical properties of breast tissues to set the contrasts of compressibility and inverse density for a numerical breast model. The properties used in this example are based on those reported in [94] and are listed in Table 6.6. These properties of the breast, as well as for other biomedical tissues, are also discussed in [14, 62, 64, 94–97]. Thus, using Table 6.6 and the properties of the water background medium, the contrast profiles for breast tissues can be found as shown in Table 6.7. It should be noted that the value of the attenuation used in this work is for 1 MHz. As can be seen, the numerical range of the contrast profiles varies considerably. Therefore, the following balancing coefficient are applied to this problem

$$Q_1 = 0.1, \quad Q_2 = 0.01, \quad Q_3 = 0.1$$

Table 6.6: Ultrasound properties for breast tissue at 22°C

Tissue	c (m/s)	ρ (kg/m ³)	α (dB cm ⁻¹ MHz ⁻¹)
Fibroadenoma	1557	1010	0.09
Glandular	1511	970	0.22
Cancer	1533	990	0.13
fat	1492	950	0.35

Table 6.7: χ_1^c and χ_2 for breast tissues at 22°C

Tissue	χ_{1r}^c	χ_{1i}^c	χ_2
Fibroadenoma	-0.1	-0.005	-0.01
Glandular	-0.006	-0.003	0.03
Cancer	-0.05	-0.007	0.01
fat	0.04	-0.002	0.05

Breast Model within a $12\lambda_{\min} \times 12\lambda_{\min}$ imaging domain

The reconstruction results for the contrast profiles of a numerical breast model within a $12\lambda_{\min} \times 12\lambda_{\min}$ imaging domain are considered in this section. The breast model along with the true contrast profiles are shown in Fig 6.10. The number of transmitters and receivers used in this example is 90 ($nRx = 90$ and $nTx = 90$). The number of frequencies and the actual frequencies used are

$$n_f = 6, \quad f = [250, 280, 300, 320, 340, 360] \text{ kHz}$$

Similar to the previous section, 3% noise (based on the average value) was added to the synthetic data set collected from this numerical breast model. In the following, the results of the reconstruction of the contrast profiles for two different cases will be shown.

The first case provides a balanced reconstruction for this multiple-frequency synthetic data set. The BIM converged after 8 iterations. The number of CGLS iterations for different iterations of the BIM is 2, 4, 18, 40, 80, 120, 150 and 180 respectively.

The reconstruction of the contrast profiles for the first, third, fifth, sixth and eighth iterations of the BIM is shown in Fig 6.11. The results of the comparison between the exact value of the contrast profiles with the reconstructed contrast profiles for the elements on the diagonal from the top left corner to the bottom right corner are shown in Fig 6.12. The first, second, third, fourth and fifth rows of Fig 6.12 correspond to the first, third, fifth, sixth and eighth iterations of the BIM. Note that since the discretization mesh for the true profiles and the reconstructed profiles are different, we need to use an interpolation scheme to compare the reconstructed profiles with the true profiles. Herein, a linear interpolation scheme is used for this purpose. The error of each contrast profiles with respect to the exact contrast profiles and data misfit for different BIM iterations are shown in Table 6.8.

The second case shows the reconstruction of this same numerical breast model for a single-frequency data set without the use of the balancing method. The single frequency of the operation is 360 kHz. BIM converged after 8 iterations, and the number of CGLS iterations at each iteration of the BIM was 4, 18, 30, 60, 100, 130, 160, 180, respectively. The results of the reconstruction of the contrast profiles for the first, second, fourth, sixth and eighth BIM iteration are shown in Fig 6.13. Comparing Fig 6.13 and Fig 6.11, it can be concluded that the multiple frequency method and balancing method significantly improve the reconstruction of the contrast profiles. This is due to the fact that (1) we use more information about the OI when using multiple frequencies method, and (2) balancing the contrast profiles brings all the contrast profiles within a similar range.

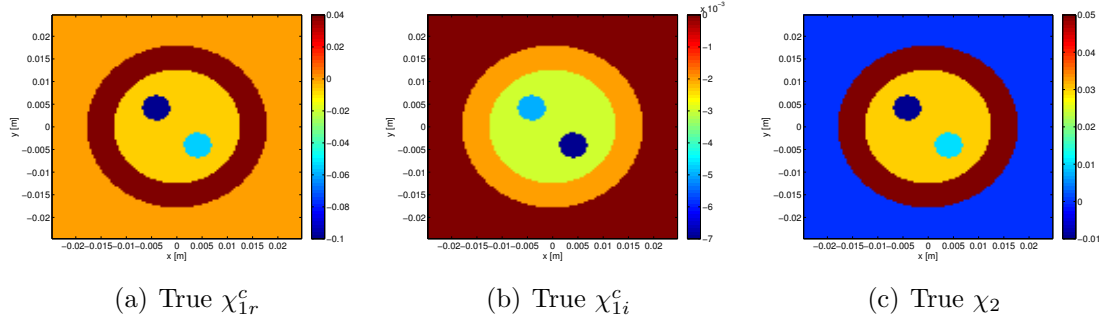


Figure 6.10: True value of χ_1^c and χ_2 for breast tissues for the case that the size of imaging domain is $12\lambda_{\min} \times 12\lambda_{\min}$.

Table 6.8: Residual error and data misfit for the breast model within a $12\lambda_{\min} \times 12\lambda_{\min}$ imaging domain. These values for each iteration of the BIM are shown below.

BIM Iteration	$\ \chi_{1r}^c(\text{Exact}) - \chi_{1r}^c(\text{Simu})\ _2$	$\ \chi_{1i}^c(\text{Exact}) - \chi_{1i}^c(\text{Simu})\ _2$	$\ \chi_2(\text{Exact}) - \chi_2(\text{Simu})\ _2$	Data misfit
	$\ \chi_{1r}^c(\text{Exact})\ _2$	$\ \chi_{1i}^c(\text{Exact})\ _2$	$\ \chi_2(\text{Exact})\ _2$	
1	1.0297	0.9498	0.8463	0.4173
2	0.9297	0.7957	0.8805	0.1397
3	0.8913	0.2746	0.8285	0.0293
4	0.7313	0.2208	0.6749	0.0141
5	0.6309	0.1781	0.5768	0.009
6	0.5280	0.1783	0.4663	0.0082
7	0.4414	0.2106	0.3825	0.0083
8	0.4023	0.1885	0.3337	0.008

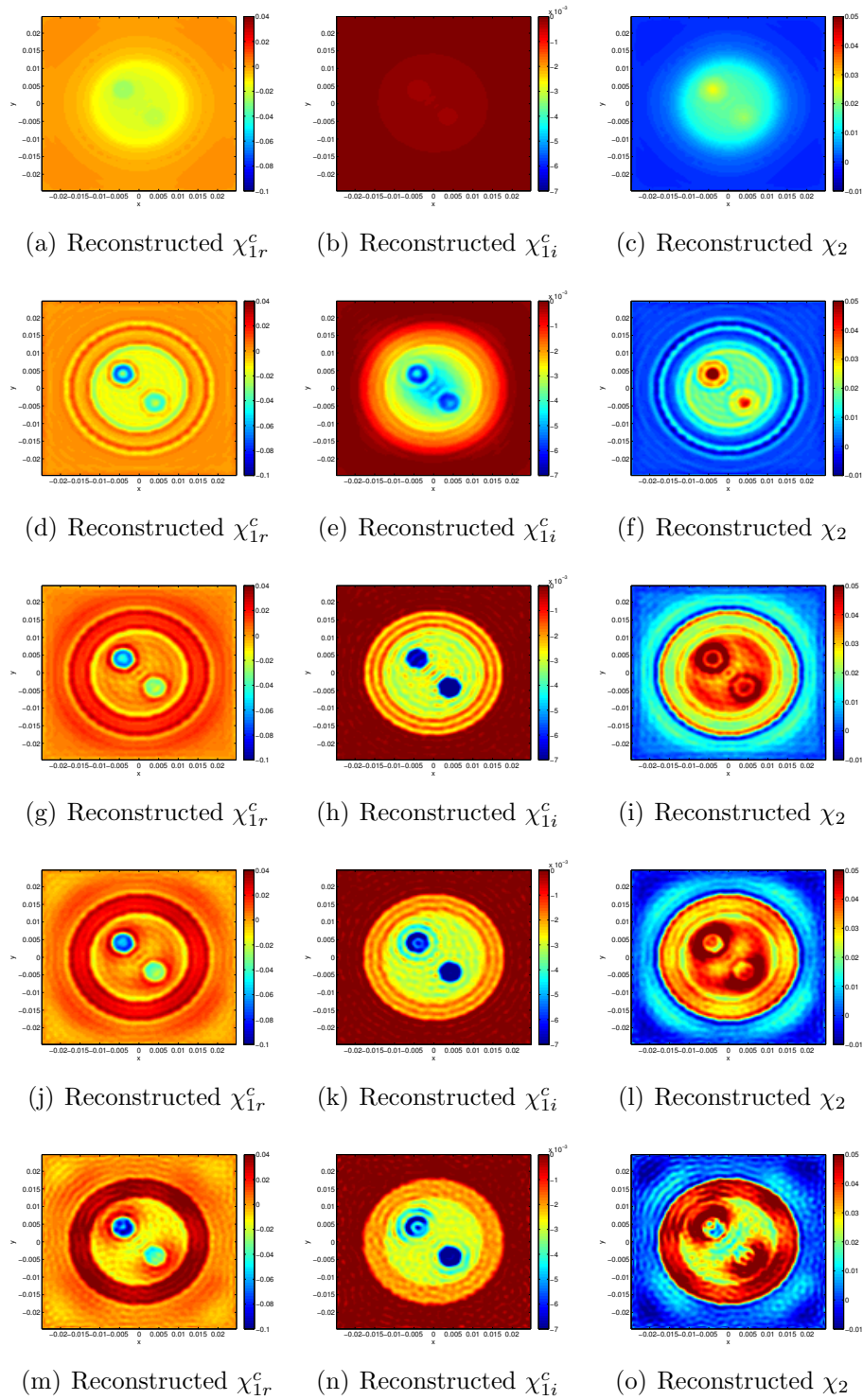


Figure 6.11: Reconstruction of χ_1^c and χ_2 for the breast model within a $12\lambda_{\min} \times 12\lambda_{\min}$ imaging domain. The first, second, third, fourth, and fifth rows correspond to the reconstruction of the contrast profiles for the 1st, 3rd, 5th, 6th, and 8th iteration of the BIM, respectively.

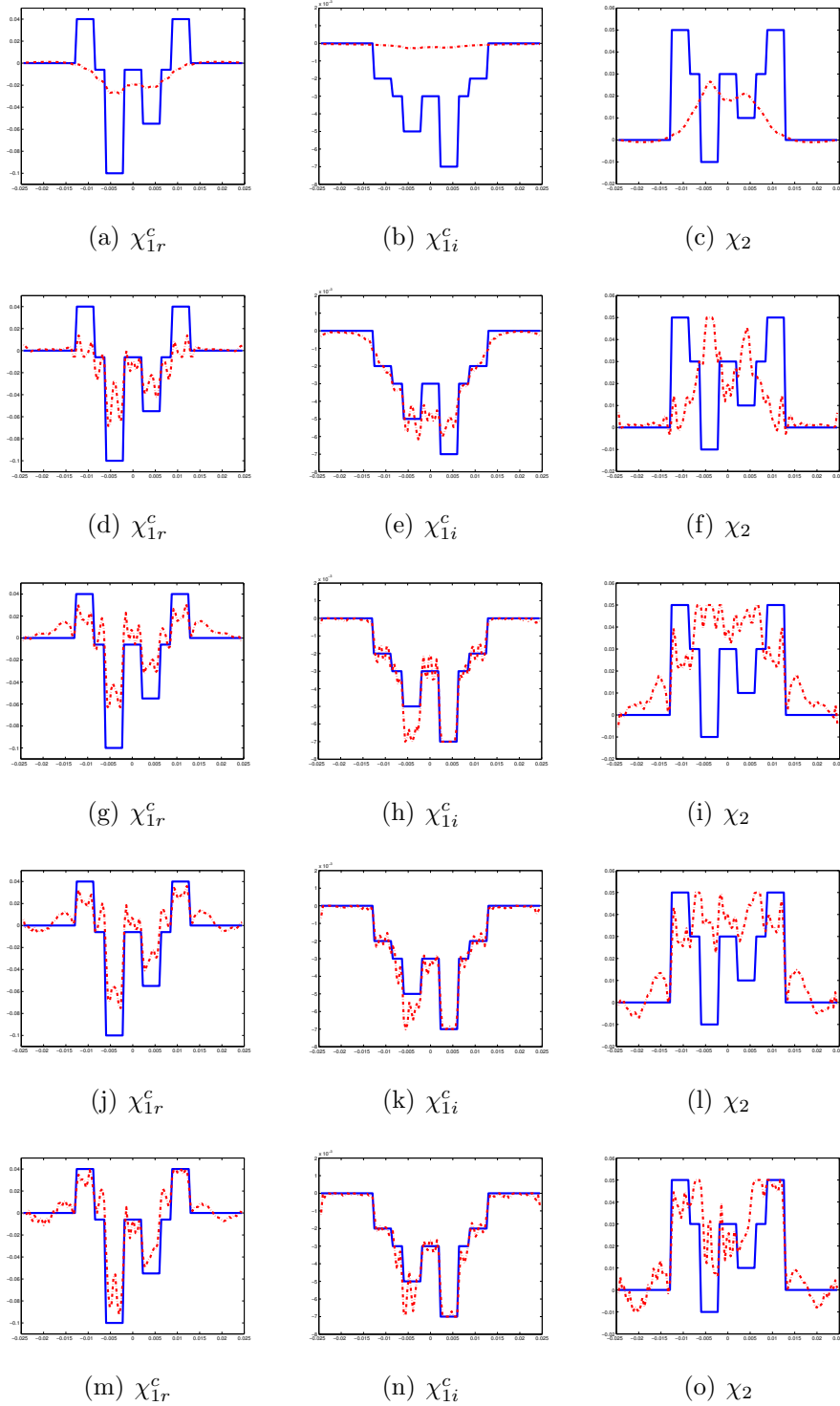


Figure 6.12: Diagonal cut from the top left corner to the bottom right for the breast model within a $12\lambda_{\min} \times 12\lambda_{\min}$ imaging domain. The first, second, third, fourth and fifth rows correspond to the first, third, fifth, sixth and eighth iterations of the BIM. The solid blue line corresponds to the actual contrast profiles and the dashed red line corresponds to the reconstructed contrast profiles

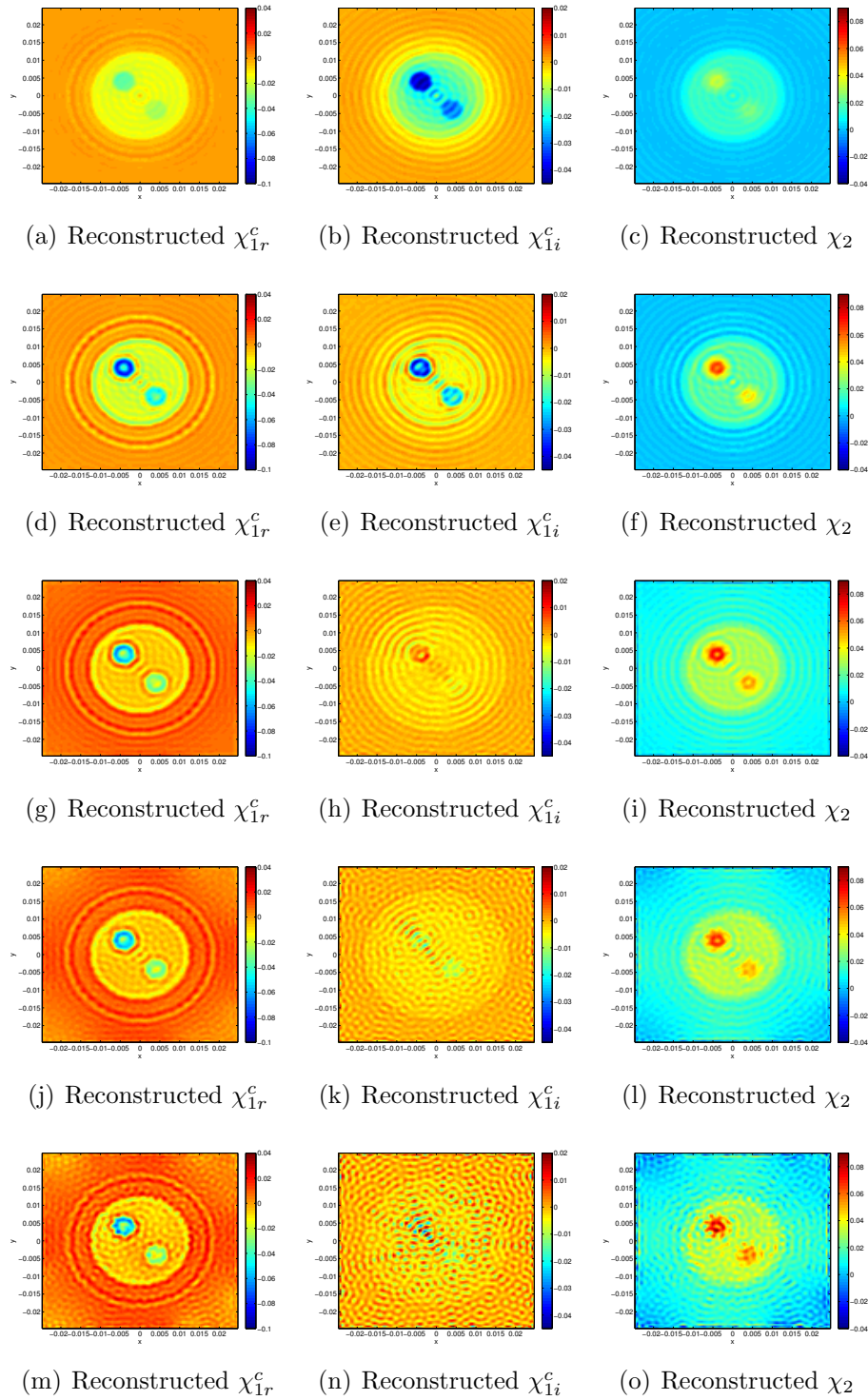


Figure 6.13: Reconstruction of χ_1^c and χ_2 for the breast model within a $12\lambda_{\min} \times 12\lambda_{\min}$ imaging domain and three percent noise is added. A single frequency is used and the balancing method is not applied. The first, second, third, fourth, and fifth row correspond to the reconstruction of the contrast profiles for the 1th, 2th, 4th, 6th, and 8th iterations of the BIM inversion algorithm respectively.

Breast Model within a $22\lambda_{\min} \times 22\lambda_{\min}$ imaging domain

In this example, we increase the size of the imaging domain as well as the size of the breast model, to be closer to reality. The size of the imaging domain is $22\lambda_{\min} \times 22\lambda_{\min}$ which in this case is 11.6 cm by 11.6 cm. Similar to the previous targets, the scattered simulated data is contaminated by three percent noise using (6.1). Seven frequencies between 250 kHz and 280 kHz are used for the multiple-frequency inversion method. The number of transmitters and receivers used in this example are 120. Only four BIM iterations are used and the number of CGLS series in each iteration is 4, 18, 50 and 80. The balancing coefficients that have been chosen for this example are the same as for the smaller model:

$$Q_1 = 0.1, \quad Q_2 = 0.01, \quad Q_3 = 0.1$$

It should be noted that in this case we truncated the BIM after only four iterations due to the fact that this large domain problem is very computationally expensive (it takes on the order of days). The results of the reconstruction of the contrast profiles for different BIM iterations are shown in Fig 6.14.

6.2 Measurement Results

The UT measurement system which has been developed in the Electromagnetic Imaging Laboratory at the University of Manitoba is shown in Fig 6.15. This system consists of eight rows of transceivers. Each row consists of 32 transducers. The frequency range for this system is between 0.7 MHz and 1.3 MHz. More information about the system and the different types of calibration techniques which have been used for the time-domain pulse data obtained from this system are explained in [1].

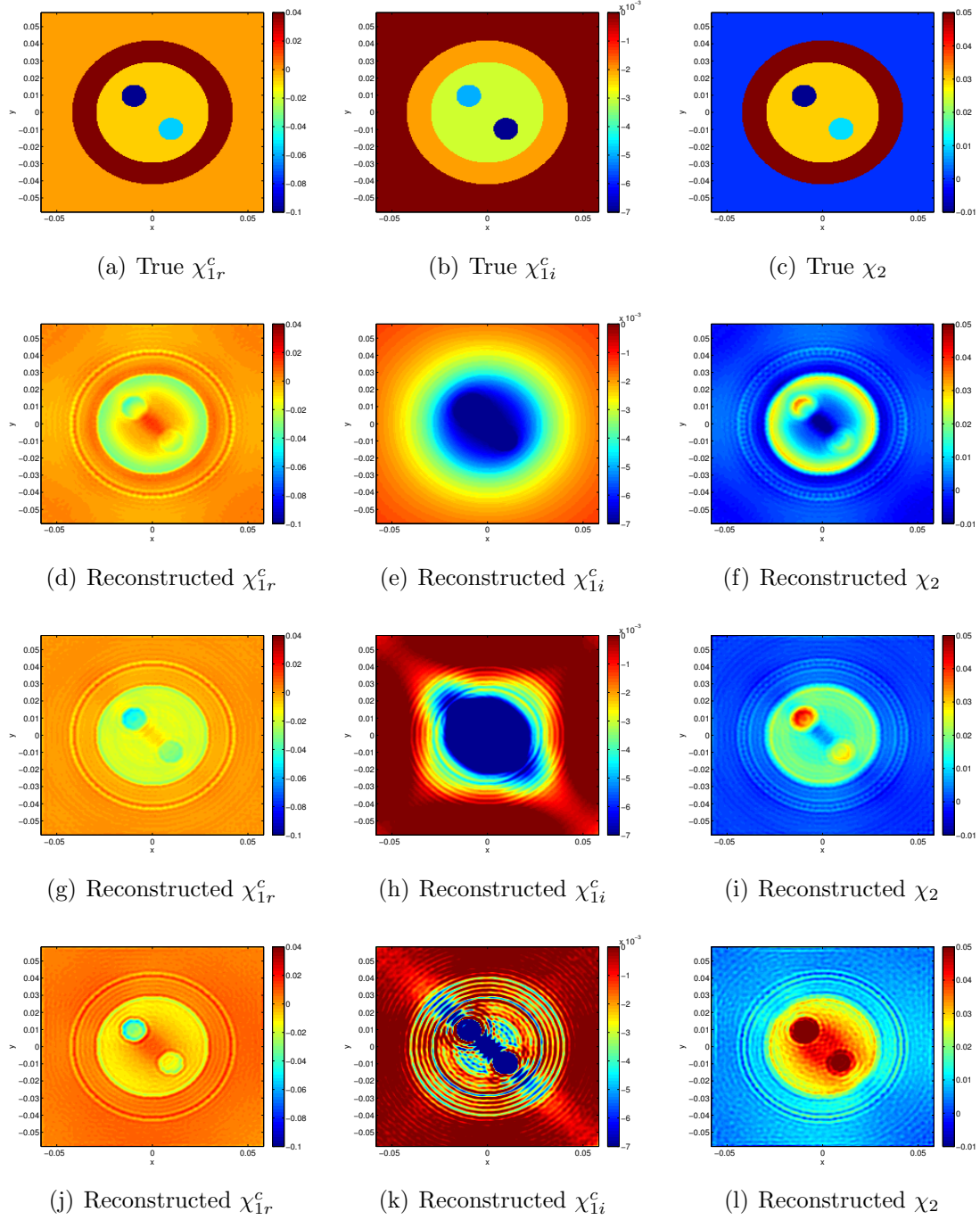


Figure 6.14: Simultaneous reconstruction of χ_1^c and χ_2 for the realistic numerical breast model. The size of the domain is 11.6 cm by 11.6 cm ($22\lambda \times 22\lambda$). $nRx, nTx = 120$, $n_f = 7$ and $250\text{KHz} \leq f \leq 280\text{KHz}$. Four BIM iterations are used. The number CGLS iterations used in this example are 4, 18, 50 and 80.

In the following, the reconstruction results of the contrast profiles for two OIs will be shown.

The first measurements correspond to the case that the OI consists of two wires as shown in Fig 6.16 (a). For reconstruction of this object, 32 transmitters and 5 receivers per transmitter are used ($nTx = 32, nRx = 5$). Also, 26 frequencies between 1.1 MHz and 1.3 MHz are used for the multiple-frequency inversion method. The measured data is calibrated using the incident field calibration [1]. The BIM is then applied to the calibrated measured data. The reconstruction results of the contrast profiles are shown in the second row of Fig 6.16.

The second measurements correspond to the case that the OI consists of three wires as shown in Fig 6.17 (a). In this example, 32 transmitters and 5 receivers per transmitter were used. The number of frequencies and the range of the frequency used in this example are

$$n_f = 26, \quad 1.1\text{MHz} \leq f \leq 1.3\text{MHz}$$

The reconstructions of the contrast profiles for this OI using the incident field calibration, are shown in the second row of Fig 6.17. It should be noted that the amount of information obtained about the OI is very much smaller than the number of unknowns in this example. That is, the amount of information obtained about the OI is

$$\text{Amount of information} = nRx \times nTx \times n_f = 32 \times 5 \times 26 = 4160$$

At the highest frequency of $f = 1.3$ MHz, the wavelength is

$$\lambda_{\min} = \frac{c}{f_{\max}} = \frac{1483}{1.3 \text{ MHz}} = 0.0011\text{m} \simeq 1\text{mm}$$

Therefore, if the size of imaging domain is $10 \text{ mm} \times 10 \text{ mm}$ this is equivalent to $10\lambda_{\min} \times 10\lambda_{\min}$ (the size that is needed for imaging this 3 wire object), then the number of discretized elements in the x and y axes will be

$$n_x = 100, \quad n_y = 100$$

where 10 cells per wavelength are assumed to sufficiently resolve the acoustic wave problem. Therefore, the total number of discretized elements in the imaging domain is

$$N = n_x \times n_y = 10000$$

In this inversion algorithm, we simultaneously reconstruct the contrast of compressibility and inverse density. We also know that the contrast of compressibility is a complex value which counts for two unknowns in each cell. Therefore, the total number of unknowns in this problem is

$$\text{Total Number of unknowns} = 3N = 30000$$

As can be seen, the total number of unknowns is much larger than the number of data points (*i.e.*, the information). In addition to this large discrepancy between the number of unknowns and the number of data points, the level of noise is high in this imaging system (low signal-to-noise ratio). Thus, we don't expect to have a good reconstruction of the OI in terms of quantitative imaging. However, we can distinguish the three wires from each other; thus, having some qualitative information about the OI. The fact that we can somehow distinguish these three wires shows the high resolution capability of UT.

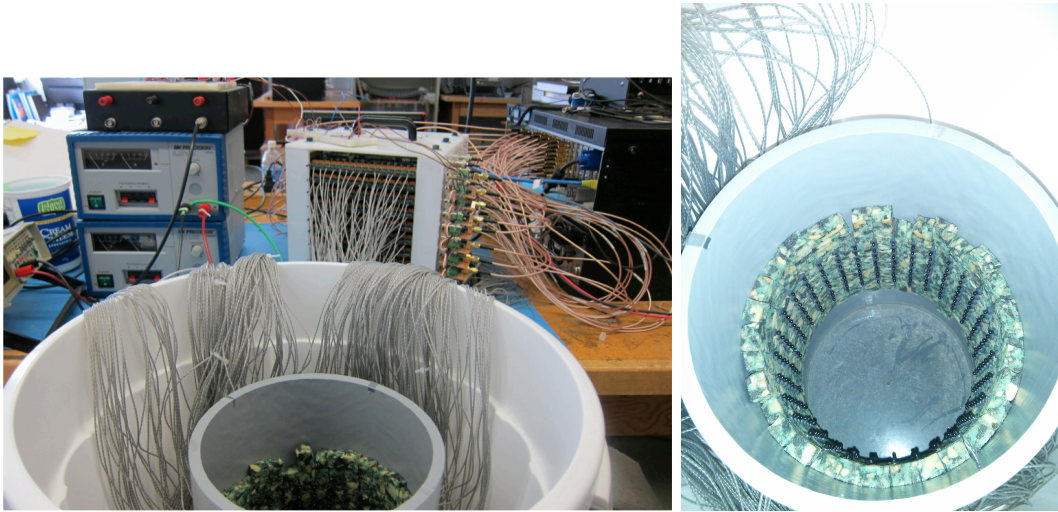
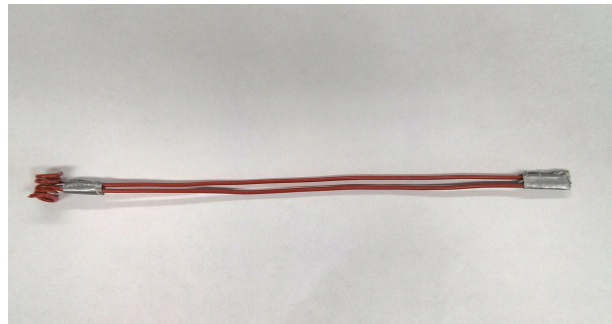
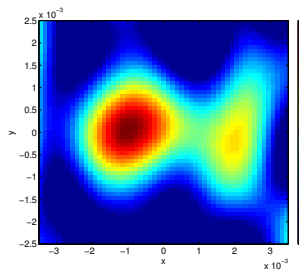


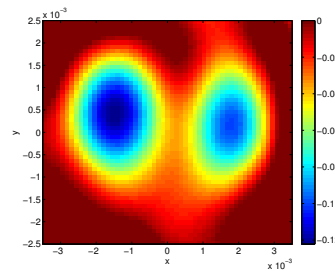
Figure 6.15: The ultrasound measurement system at the Electromagnetic Imaging Laboratory at the University of Manitoba.



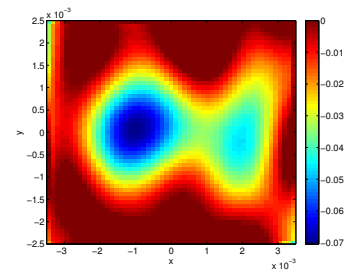
(a) Two wires



(b) Reconstructed χ_{1r}^c

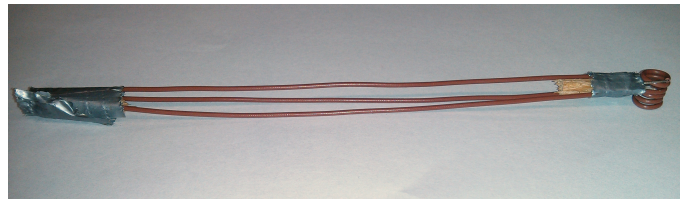


(c) Reconstructed χ_{1i}^c

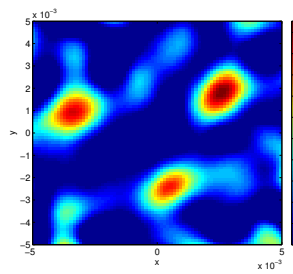
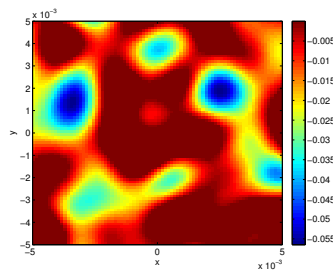
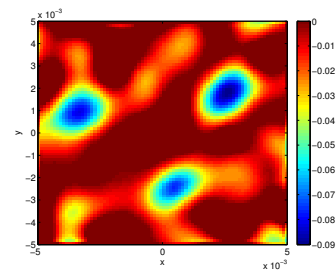


(d) Reconstructed χ_2

Figure 6.16: Simultaneous reconstruction of χ_1^c and χ_2 for two wires.



(a) Three wires

(b) Reconstructed χ_{1r}^c (c) Reconstructed χ_{1i}^c (d) Reconstructed χ_2 Figure 6.17: Simultaneous reconstruction of χ_1^c and χ_2 for three wires.

7

Summary, Conclusions and Future Work

7.1 Summary and Conclusions

In this dissertation, the Ultrasound Tomography (UT) problem was formulated based on a two-dimensional (2D) inverse scattering model. This results in a quantitative imaging modality which can open up new industrial and biomedical applications. In terms of biomedical applications, it can be very useful because in addition to safe ultrasound energy, it can potentially identify tissues based on their acoustic properties. Noting its ability to quantify tissue properties as well as its high resolution, due to its small wavelength, it may be possible to distinguish between benign and malignant tissues at an early stage of disease development. The following is a summary and conclusion of the presented work:

- The UT problem was cast in the framework of inverse scattering. The mathematical formulation associated with this inverse scattering problem was derived. This mathematical formulation was based on two important integral equations: data and domain equation.
- The ultrasound properties of the object of interest (OI) are its density and compressibility. To the best of the author's knowledge, most of the published

work in this area assumes that the density profile is constant. That is, they assume that density does not vary within the OI. However, in this thesis, both compressibility and density profiles were taken as unknown and reconstructed. This is important because experimental results show that the density profile is not constant in human tissues. Therefore, the formulation in this thesis can potentially provide more accurate images compared to images obtained by assuming a constant density profile.

- The first step toward creating the inversion algorithm to deal with this problem was to develop an appropriate forward solver. A forward solver based on the Neumann series was implemented. This forward solver has the limitation that the OI must be low contrast and small compared to the operating wavelength. This limitation can be serious for UT as the objects, e.g., a human breast, can be considerably larger than the ultrasound wavelength.
- Due to the limitations of the Neumann series forward solver, an efficient MoM forward solver, based on the CG algorithm, was implemented to handle OIs which are large compared to the wavelength. To use this forward solver, an appropriate operator and its adjoint for the acoustic case were developed. These were derived and used in the implementation of the MoM forward solver.
- To make this MoM faster and more efficient, extra features were developed. The first feature used a marching-on-source technique to find a better initial guess for the CG algorithm so as to converge in less iterations. The second feature used the properties of block Toeplitz matrices to save on memory storage. The third feature utilized the FFT-based matrix-vector multiplication so as to reduce the computational complexity. Using this fast and efficient forward MoM forward

solver, domains as large as $22\lambda \times 22\lambda$ were simulated.

- The inversion algorithm that was utilized in this thesis was the Born Iterative Method (BIM). The BIM is an iterative inversion algorithm which requires calling the forward solver at each iteration. The MoM forward solver was incorporated into the BIM for the UT problem. As the BIM also requires a regularization technique at each of its iterations, the CGLS method was used as a regularization algorithm because it is one of the fastest available regularization techniques.
- The developed inversion algorithm simultaneously reconstructs the compressibility and density profiles. To make this inversion algorithm more capable, the ability to simultaneously invert multiple-frequency data sets was added to the algorithm. Also, a balancing method was added to the inversion algorithm to result in more accurate quantitative images.
- This inversion algorithm was applied to synthetically-collected as well as measured data. The results obtained show that having quantitative images from this technique is possible. However, the accuracy of the reconstructed images was not always good especially for the density profile when a significant amount of noise was added.
- It was also shown in this thesis that the use of multiple-frequency data sets is crucial to obtaining sufficient information about the object of interest. Using a single-frequency data set often results in large imbalances between the number data points and the number of unknowns to be reconstructed.
- It was also shown that when the contrast profiles to be found are not numerically in the same range, the dominant one is often reconstructed with more accuracy.

It was also shown that the use of a balancing method can improve the overall reconstruction accuracy for all the contrasts. The use of this balancing method requires prior information about the existence and approximate ratio of the imbalance.

In summary, the ultrasound inverse scattering algorithm implemented in this thesis is capable of providing three quantitative images of the object being imaged. These three quantitative images provide information about the object. However, in its current state of development, this algorithm sometimes fails to provide accurate images. In such situations, the reconstruction of the real and imaginary parts of the compressibility profile is relatively accurate; but, that of the density profile contains oscillatory artifacts.

7.2 Future Work

Several suggestions to improve the developed UT inversion algorithm are as follows.

- Making the code parallel so as to be able to invert larger domains.
- Using a regularization method that has an edge preserving feature such as the multiplicative weighted L_2 -norm total variation regularizer or the L_1 -norm additive regularizer. This may improve reconstruction results. The multiplicative weighted L_2 -norm total variation regularizer is explained in Appendix C and the concept of L_1 -norm additive regularizer is explained in Appendix D.
- In cases in which we do not need to know the compressibility and density contrast values independently, it might be more efficient to reconstruct the speed of sound within the tissue. This is due to the fact that the speed of sound is

dependent on both the compressibility and the density. Therefore, the variations of compressibility and density profiles will be reflected in the variation of the speed of sound profile. The advantage of using this method compared to what was done in this thesis is that in this case we would only have one contrast. Therefore, the number of unknowns decreases so that this method is computationally more efficient, and fewer data points would need to be collected. In addition, it is this author's opinion that this method would require a fewer number of CGLS iterations.

- The 2D inversion algorithm could be extended to a 3D inversion algorithm.
- The Time of Flight tomography (TFT) approach can be combined with the UT inversion algorithm. TFT is computationally more efficient than the inversion algorithm presented here, because instead of solving the full wave equation which is computationally expensive, the geometrical acoustic ray approximation is used. Thus, one would apply TFT to reconstruct qualitative images of the OI and then use this information as a prior information for the UT inversion algorithm to reconstruct the quantitative images of the OI.

A

Discretization of the Forward Model

In this thesis, the imaging domain is discretized into square cells and the Method of Moments (MoM) algorithm is based on the Richmond's method [98]. Noting that we are concerned with 2D ultrasound tomography, we only need to discretize the imaging domain along the x and y axes. The number of discretized elements in the x and y axis is denoted by n_x and n_y . Thus, the total number of discretized elements (cells) in the imaging domain will be

$$N = n_x \times n_y \tag{A.1}$$

The discretized imaging domain is shown in Fig A.2. In this figure, the red dashed circle is the location of the transducers. This measurement domain is outside the imaging domain.

Similar to Richmond's paper, it is assumed that in each square cell the pressure is uniform [98]. Thus, the size of each square cell must be small enough for this assumption to hold [98]. Therefore, we only need to find the pressure at the centre of each cell [98].

We now discretize the operator on this square cell mesh. As shown in (3.1), the

total pressure can be found as

$$\begin{aligned}
 p(\mathbf{r}) &= p^{inc}(\mathbf{r}) + k_0^2 \int g(\mathbf{r}, \mathbf{r}') \chi_1^c(\mathbf{r}') p(\mathbf{r}') d\mathbf{r}' \\
 &+ \int g(\mathbf{r}, \mathbf{r}') \nabla \cdot [\chi_2(\mathbf{r}') \nabla p(\mathbf{r}')] d\mathbf{r}'
 \end{aligned} \tag{A.2}$$

where $g(\mathbf{r}, \mathbf{r}')$ is the Green's function.

The contrast profiles, χ_1^c and χ_2 , are discretized using pulse basis functions. That is, it is assumed that within each discretization cell, the value of the contrast profile is constant. A finite difference method is used to find the gradient and divergence in this thesis [99]. For example, the gradient of the pressure for the two-dimensional case at the position (i, j) as shown in Fig A.1 can be found as

$$\nabla p_{i,j} = \frac{p_{i+1,j} - p_{i-1,j}}{2\Delta x} \hat{a}_x + \frac{p_{i,j+1} - p_{i,j-1}}{2\Delta y} \hat{a}_y \tag{A.3}$$

where $p_{i,j}$ is the pressure at the position (i, j) . Δx and Δy are the distance between the two successive discretized elements in the x and y axes respectively. As can be seen in (A.3), the central difference is used to find the gradient of the pressure [99]. This is due to the fact that both the backward and forward points around the centre are used [99].

In this thesis, the incident pressure in the imaging domain, is assumed to be that of a point source. That is, we place a point source at the position of each transmitter and then we find the pressure in the imaging domain due to that point source. Thus, the incident field is the pressure due to a point source which is given as

$$\frac{1}{4j} H_0^2(k_0 |\mathbf{r} - \mathbf{r}'|) \tag{A.4}$$

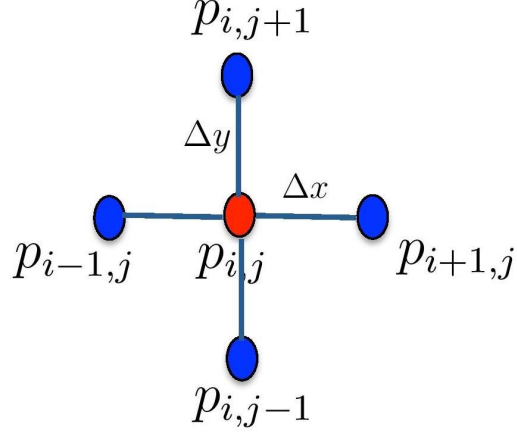


Figure A.1: Calculation of $\nabla p_{i,j}$ for the 2D case using the central finite difference approximation.

where \mathbf{r} is the position of the transmitter and \mathbf{r}' corresponds to the position of the centre of each discretized imaging domain. Thus, for each transmitter, the size of the incident pressure vector in the imaging domain will be N . We construct such as incident pressure vector for all transmitters and frequencies, and this represents the information about the incident pressure. It should be noted that in this case the position of \mathbf{r} and \mathbf{r}' are always different because the transmitter is outside the imaging domain.

As can be seen in (A.2), the Green's function is the common part in both integrals. This Green's function for the 2D time-harmonic problem (assuming a $e^{+j\omega t}$ time dependency) is

$$g(\mathbf{r}, \mathbf{r}') = \frac{1}{4j} H_0^2(k_0 |\mathbf{r} - \mathbf{r}'|) \quad (\text{A.5})$$

Thus,

$$k_0^2 \int_D g(\mathbf{r}, \mathbf{r}') d\mathbf{r}' = \frac{k_0^2}{4j} \int_D H_0^2(k_0 |\mathbf{r} - \mathbf{r}'|) d\mathbf{r}' \quad (\text{A.6})$$

To find the total pressure in the imaging domain \mathcal{D} , the domain equation is used. In the domain equation, both \mathbf{r} and \mathbf{r}' belong to the imaging domain ($\mathbf{r}, \mathbf{r}' \in \mathcal{D}$). It should be noted that in this case we are faced with a singularity when the observation point is at one of the locations, \mathbf{r}' , within D where the integration is taken. Say this is the centre of cell n [98]. To handle this singularity, the following method is used (based on [98]):

$$\frac{k_0^2}{4j} \int H_0^2(k_0|\mathbf{r} - \mathbf{r}'|)d\mathbf{r}' = \begin{cases} \frac{-j}{2} [\pi k_0 a H_1^{(2)}(k_0 a) - 2j] & \text{if } m = n \\ (\frac{-j\pi k_0 a}{2}) J_1(k_0 a) H_0^{(2)}(k_0|\mathbf{r}_m - \mathbf{r}_n|) & \text{if } m \neq n \end{cases} \quad (\text{A.7})$$

where m is the cell of the observation point and n identifies a cell in the imaging domain. The position vectors \mathbf{r}_m and \mathbf{r}_n are the position vectors for the centre of these cells. The parameter a denotes the radius of a circle which has the same area as the square cell. That is,

$$\pi a^2 = d_x \times d_y \quad \implies \quad a = \sqrt{\frac{d_x \times d_y}{\pi}} \quad (\text{A.8})$$

where d_x and d_y denote the length of each side of the square cell (in our case, $d_x = d_y$).

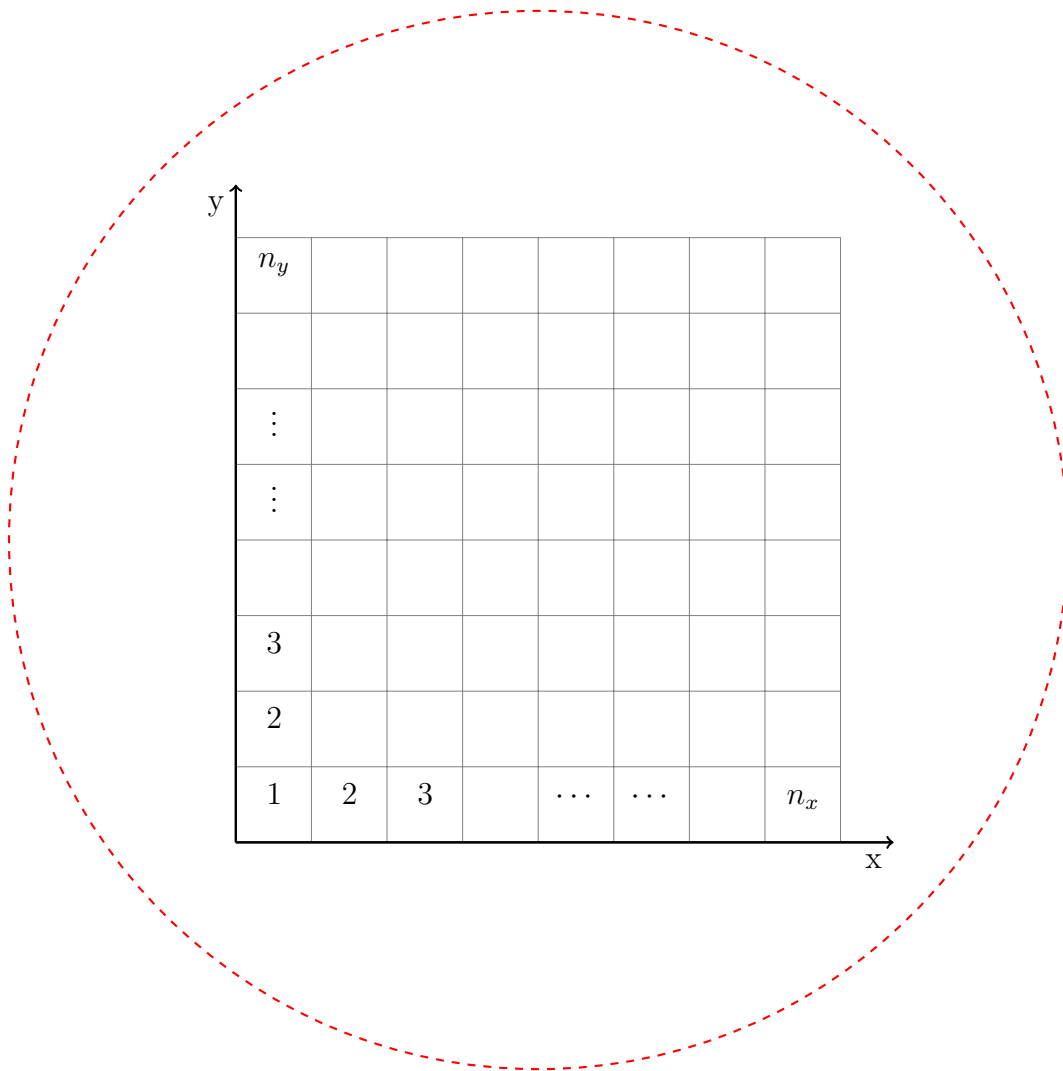


Figure A.2: The discretization of the imaging domain using square cells is shown in this figure. n_x and n_y are the number of elements in the x and y axis. The red dashed circle represents the location of the transducers.

B

Conjugate Gradient Method

In this Appendix, we will explain how to use the CG method to find x in $Ax = b$. As explained before, x , the solution of $Ax = b$ can be found using the following minimization [79]:

$$x = \arg \min_x \{ \|Ax - b\|_2^2 \} \quad (\text{B.1})$$

where $\|Ax - b\|_2^2$ is called the cost functional and is denoted by C . The CG method is an iterative method where x is updated in each iteration as [30, 79, 100, 101]

$$x^{(n+1)} = x^{(n)} + \alpha^{(n)} s^{(n)} \quad (\text{B.2})$$

where $x^{(n+1)}$ and $x^{(n)}$ are the x for $(n+1)^{\text{th}}$ and n^{th} iterations respectively. $s^{(n)}$ is the search direction for the n^{th} iteration and $\alpha^{(n)}$ is the weighting parameter that controls the size of search direction. In this method, the search direction can be found as [30, 79, 100, 101]

$$s^{(n)} = g^{(n)} + \beta^{(n)} s^{(n-1)} \quad (\text{B.3})$$

where $g^{(n)}$ is the gradient of the cost function for the i^{th} iteration. The coefficient β is a scalar parameter. There are different methods to find this coefficient such as the classical form and Polak-Ribiere formula [79]. In the classical conjugate gradient

method, β can be found as [30, 79]

$$\beta = \frac{\|g^{(n)}\|_2^2}{\|g^{(n-1)}\|_2^2} \quad (\text{B.4})$$

It should be noted that β is zero in the first iteration. The gradient of the cost function can be found as

$$\begin{aligned} \left. \frac{\partial C(x)}{\partial x} \right|_{x=x_n} (\psi) &= \lim_{\epsilon \rightarrow 0} \frac{\|A(x + \epsilon\psi) - b\|_2^2 - \|Ax - b\|_2^2}{\epsilon} \\ &= \lim_{\epsilon \rightarrow 0} \left(\frac{\|Ax - b\|_2^2 + \epsilon^2 \|A\psi\|_2^2}{\epsilon} \right. \\ &\quad \left. + \frac{2\epsilon \operatorname{Re} \langle Ax - b, A\psi \rangle - \|Ax - b\|_2^2}{\epsilon} \right) \\ &= 2\operatorname{Re} \langle Ax - b, A\psi \rangle \\ &= 2\operatorname{Re} \langle A^H(Ax - b), \psi \rangle \end{aligned} \quad (\text{B.5})$$

Thus, the gradient of the cost function is

$$g = A^H(Ax - b) \quad (\text{B.6})$$

$\alpha^{(n)}$ should be chosen in such a way that minimizes the cost function [30, 101]. Therefore, we will have

$$\left. \frac{\partial C}{\partial \alpha} \right|_{x=x^{(n+1)}} = 0 \quad (\text{B.7})$$

The cost function for multiplicative regularization at $x = x^{(n+1)}$ is

$$\begin{aligned} C(x = x^{(n+1)}) &= \|Ax^{(n+1)} - b\|_2^2 = \|A(x^{(n)} + \alpha^{(n)} s^{(n)}) - b\|_2^2 \\ &= \|(Ax^{(n)} - b) + A\alpha^{(n)} s^{(n)}\|_2^2 \end{aligned} \quad (\text{B.8})$$

or

$$C(x = x^{(n+1)}) = \left(\|Ax^{(n)} - b\|_2^2 + [\alpha^{(n)}]^2 \|As^{(n)}\|_2^2 + 2\alpha^{(n)} \text{Re} \langle Ax^{(n)} - b, As^{(n)} \rangle \right) \quad (\text{B.9})$$

Therefore, the gradient of the cost function with respect to $\alpha^{(n)}$ can be found as

$$\left. \frac{\partial C}{\partial \alpha^{(n)}} \right|_{x=x^{(n+1)}} = 2\alpha^{(n)} \|As^{(n)}\|_2^2 + 2\text{Re} \langle Ax^{(n)} - b, As^{(n)} \rangle = 0 \quad (\text{B.10})$$

Therefore, $\alpha^{(n)}$ can be found as

$$\alpha^{(n)} = \frac{-\text{Re} \langle Ax^{(n)} - b, As^{(n)} \rangle}{\|As^{(n)}\|_2^2} \quad (\text{B.11})$$

C

Multiplicative Regularization

A Multiplicative regularization [30, 102–105] is one of the most important and powerful regularization methods. In this method, instead of adding one term to the cost function explained in Section 5.4, we multiply the cost function by a regularization term. One form of the multiplicative regularizer which has received lots of attention is the weighted L_2 -norm total variation multiplicative regularizer. In this method, we will have the following minimization to solve $Ax = b$ [30, 102, 105]

$$x^{\text{multiplicative}} = \arg \min_x \left\{ \frac{\|Ax - b\|_2^2}{\|b\|_2^2} \int d_n^2 [|\nabla x|^2 + \delta_n^2] ds \right\} \quad (\text{C.1})$$

The above minimization is usually performed iteratively using the CG method. The parameter δ_n^2 is a positive parameter at the n^{th} iteration of the CG algorithm. This parameter controls the strength of regularization [30]. Thus, this parameter is sometimes referred to as the steering parameter. Also, d_n is defined as [30, 102]

$$d_n \triangleq \frac{1}{\sqrt{\text{Area}(|\nabla x_{n-1}|^2 + \delta_{n-1}^2)}} \quad (\text{C.2})$$

where x_{n-1} is the predicted x at the $(n - 1)^{\text{th}}$ iteration of the CG algorithm. Note that as opposed to Tikhonov regularization, the cost function to be minimized in this method is changing. This is due to the fact that the parameters δ_n and d_n which define

the cost function change at each iteration of the CG algorithm. In fact, according to (C.1), the cost function of multiplicative regularization will be

$$C_n(x) = \frac{\|Ax - b\|_2^2}{\|b\|_2^2} \int d_n^2(\mathbf{r}) \left[|\nabla x|^2 + \delta_n^2 \right] d\mathbf{s} \quad (\text{C.3})$$

where the cost function is dependent on the number of iteration n . Note that this cost function consists of two parts: (1) the first part of the cost function corresponds to the least square solution and it is denoted by C^{LS} (independent of n), (2) the second part of the cost function corresponds to the multiplicative regularization term and it is denoted by C_n^{MR} (changing with n). Thus,

$$C^{LS}(x) \triangleq \frac{\|Ax - b\|_2^2}{\|b\|_2^2} \quad (\text{C.4})$$

$$C_n^{MR}(x) \triangleq \int d_n^2 \left[|\nabla x|^2 + \delta_n^2 \right] d\mathbf{s} \quad (\text{C.5})$$

Thus, the cost function can be written as [30, 102, 103]

$$C_n(x) = C^{LS}(x) C_n^{MR}(x) \quad (\text{C.6})$$

As noted above, this multiplicatively regularized cost function can be minimized by the CG method. To use the CG method, we need to know what the gradient of the cost function is. In the following, it will be explained how to find the gradient of the cost function at the n^{th} iteration of the CG algorithm.

$$\left. \frac{\partial C_n}{\partial x} \right|_{x=x_n} = \left. \frac{\partial C^{LS}(x)}{\partial x} \right|_{x=x_n} + C^{LS}(x) \left. \frac{\partial C_n^{MR}(x)}{\partial x} \right|_{x=x_n} \quad (\text{C.7})$$

Noting that $C_n^{MR}(x = x_n)$ is equal to one. The gradient of C^{LS} and C_n^{MR} can be found as

$$\begin{aligned}
\left. \frac{\partial C^{LS}(x)}{\partial x} \right|_{x=x_n}(\psi) &= \frac{1}{\|b\|_2^2} \lim_{\epsilon \rightarrow 0} \frac{\|A(x + \epsilon\psi) - b\|_2^2 - \|Ax - b\|_2^2}{\epsilon} \\
&= \frac{1}{\|b\|_2^2} \lim_{\epsilon \rightarrow 0} \left(\frac{\|Ax - b\|_2^2 + \epsilon^2 \|A\psi\|_2^2}{\epsilon} \right. \\
&\quad \left. + \frac{2\epsilon \operatorname{Re} \langle Ax - b, A\psi \rangle - \|Ax - b\|_2^2}{\epsilon} \right) \\
&= \frac{2}{\|b\|_2^2} \operatorname{Re} \langle Ax - b, A\psi \rangle \\
&= \frac{2}{\|b\|_2^2} \operatorname{Re} \langle A^H(Ax - b), \psi \rangle
\end{aligned} \tag{C.8}$$

It should be noted that C_n^{MR} can be written as [30]

$$\begin{aligned}
C_n^{MR}(x) &= \int d_n^2 [|\nabla x|^2 + \delta_n^2] \, ds \\
&= \|d_n \nabla x\|_2^2 + \|d_n(\mathbf{r}) \delta_n\|_2^2 \\
&= \|d_n \nabla x\|_2^2 + \delta_n^2 \|d_n\|_2^2
\end{aligned} \tag{C.9}$$

If we do the same procedure shown in (C.8), we can find that [30, 105]

$$\left. \frac{\partial C_n^{MR}(x)}{\partial x} \right|_{x=x_n}(\psi) = 2 \operatorname{Re} \langle -\nabla \cdot (d_n^2 \nabla x), \psi \rangle \tag{C.10}$$

Therefore, the gradient of the cost function for multiplicative regularization will be [30]

$$\left. \frac{\partial C_n}{\partial x} \right|_{x=x_n} = \frac{1}{\|b\|_2^2} A^H(Ax - b) + \frac{\|Ax - b\|_2^2}{\|b\|_2^2} \left[-\nabla \cdot (d_n^2 \nabla x) \right] \tag{C.11}$$

Note that in the above expression, we have removed the coefficient 2 and also the real-part operator Re . This is based on the Wirtinger calculus which deals with finding

the derivative of a real-valued cost function (in our case, C_n) with respect to complex function (in our case, x).

It should be noted that we can multiply an arbitrary real number to the above gradient given in (C.11). This is due to the fact that this gradient will be eventually multiplied by the value of the step-length in the CG algorithm. Now, for example, if we multiply this gradient by $\|b\|_2^2$, the corresponding step-length will be divided by $\|b\|_2^2$. Therefore, we can write this gradient as

$$\frac{\partial C_n}{\partial x} = A^H(Ax - b) + \|Ax_{n-1} - b\|_2^2 \left[-\nabla \cdot (d_n^2 \nabla x) \right] \quad (\text{C.12})$$

Now let's compare the effect of this multiplicative regularization with Tikhonov regularization. To this end, if we assume that L in (5.16) is the Laplacian operator (i.e., $L = \nabla^2$), then the cost function for Tikhonov regularization will be

$$C^{Tikhonov} = \|Ax - b\|_2^2 + \lambda^2 \|\nabla^2 x\|_2^2 \quad (\text{C.13})$$

The gradient of the above cost function can be found as

$$\frac{\partial C^{Tikhonov}}{\partial x} = A^H(Ax - b) + \lambda^2 (-\nabla^2 x) \quad (\text{C.14})$$

Comparing the gradient of the cost function of multiplicative and Tikhonov regularization in (C.12) and (C.14), we can conclude the following (a similar comparison has been also pointed out in [30])

1. The norm of the residual error ($\|Ax - b\|_2^2$) is somehow used as a regularization parameter in multiplicative regularization instead of λ^2 in Tikhonov regularization. Let's see how this two-norm works as a regularization parameter in

multiplicative regularization. $\|Ax - b\|_2^2$ is a large number for early iterations. This is due to the fact that at early iterations x is far from the true solution. As the algorithm goes on with more iterations, x will become closer to the true solution. Thus, the residual error (regularization parameter in multiplicative regularization) becomes smaller. Therefore, it can be concluded that one of the advantages of multiplicative regularization compared to Tikhonov regularization is that it automatically finds the regularization parameter at each iteration of the algorithm [30, 102]. This feature of multiplicative regularization has an important role in terms of computational time.

2. The regularization parameter is multiplied with $-\nabla \cdot (d_n^2 \nabla x)$ [105] and $-\nabla^2 x$ in multiplicative and Tikhonov regularization respectively as shown in (C.12) and (C.14). It should be noted that the Laplacian operator (∇^2) has a smoothing effect on the solution [105]. However, the gradient operator (∇) can preserve the edges of the OI. In Tikhonov regularization L is usually chosen either the identity matrix or Laplacian operator. This is due to the fact that if $L = \nabla$, then the gradient operator contributes in all iterations (i.e., early BIM and final BIM iterations). Now, it should be noted that an edge-preserving regularization needs to be used in later iterations of the BIM when the predicted solution is sufficiently close to the true solution. Therefore, if $L = \nabla$ is used with Tikhonov regularization, there is a chance to reconstruct an error as an edge of the OI. However, multiplicative regularization method has both smoothing and edge-preserving effects [102, 103, 105]. In fact, in early BIM iterations, it more acts as a smoothing regularizer, but in later iterations of the BIM, it more acts as an edge-preserving regularizer. Now, let's see how multiplicative regularization has both of these features. As already explained, the following

term is multiplied with the regularization parameter in the gradient of the cost function in multiplicative regularization [105].

$$-\nabla \cdot (d_n^2 \nabla x) \quad (\text{C.15})$$

where d_n^2 can be found as

$$d_n^2 = \frac{1}{\text{Area} \left[|\nabla x_{n-1}|^2 + \delta_{n-1}^2 \right]} \quad (\text{C.16})$$

δ_n^2 is usually chosen as [30]

$$\delta_n^2 = \frac{1}{2} \frac{\|d_n \nabla x_{n-1}\|_2^2}{\|d_n\|_2^2} \quad (\text{C.17})$$

In the early iterations, we are far from the exact solution and therefore the residual error is a large number. However, $|\nabla x|$ is small. For example, in the first iteration, Born approximation is used and it is assumed that the total pressure in the imaging domain is equal to the incident pressure. It means that we assume that there is no object in the imaging domain. Therefore, the contrast profiles will be zero. Thus, it can be concluded that in the early iterations of multiplicative regularization, we have [103]

$$|\nabla x|^2 \ll \delta_{n-1}^2 \implies d_n \simeq \text{constant} \implies -\nabla \cdot (d_n^2 \nabla x) = -d_n^2 \nabla^2 x \quad (\text{C.18})$$

Therefore, multiplicative regularization in early BIM iterations has essentially the same effect as the Laplacian regularizer (smoothing effect). As the algorithm goes with more iterations, we will get closer to the true solution. There-

fore, the residual error ($\|Ax - b\|_2^2$) will be small, and we will face with two different situations. Let's explain these two situations in an example. In this example, it is assumed that we are close to the last iteration of the BIM (i.e., we are close to the true solution). Let's also assume that the true solution is the one shown in Figure C.1. As can be seen in this figure, the first situation is the situation in which we have a transition between two different homogeneous media. In other words, in this situation, we have an edge (sharp transition). This situation is denoted by ① in Figure C.1. The second situation the situation in which we are in a homogeneous medium. For example, this situation is denoted by ② and ③ in Figure C.1. In the first situation, the gradient of the contrast is not zero. This is due to the fact that two different media have two different contrast profiles. Therefore, the gradient of the contrast profile is not zero. Thus, we have

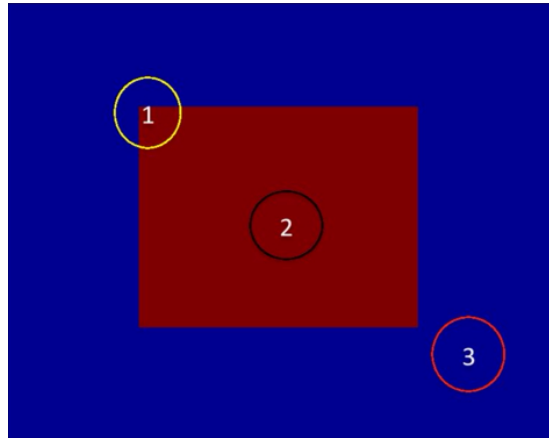
$$|\nabla x| \neq 0 \implies d_n \neq \text{constant} \implies -\nabla \cdot (d_n^2 \nabla x) \quad (\text{C.19})$$

Therefore, the gradient operator which preserve the edges is maintained in the first situation.

Now, let's see how the second situation works. In the second situation, the region is homogeneous. Therefore, we can conclude that the $|\nabla x|$ should be close to zero (i.e., no edge exists). Thus,

$$|\nabla x| \simeq 0 \implies d_n = \text{constant} \implies -\nabla \cdot (d_n^2 \nabla x) = -d_n^2 \nabla^2 x \quad (\text{C.20})$$

Therefore, this operator becomes equivalent to the Laplacian operator which has a smoothing effect. In this case, the region has no edges so that a smoothing



(a) The object containing two different media illustrated by red and blue colours.

Figure C.1: circle 1 is the inhomogeneous region. circle 2 and circle 3 are the homogeneous region.

effect on the solution can be more useful.

Therefore, multiplicative regularization is very efficient regularization because (1) the regularization parameter is automatically updated in each iteration [30, 102, 103], (2) the Laplacian operator which has a smoothing effect is applied at the early iterations of the BIM in which the predicted contrast is not sufficiently accurate for edge-preserving reconstruction, and (3) as the MR algorithms goes on with more iterations, the operator $-\nabla \cdot (d_n^2 \nabla)$ alternates between the Laplacian operator and edge-preserving operator in which edge preserving is only applied to the region containing edges and for the other regions the Laplacian operator is applied.

As already explained, the CG method [30, 79, 100, 101] is applied to minimize the multiplicatively regularized cost function. In the CG method, we have the following update for x [30, 79, 100, 101]

$$x^{(n+1)} = x^{(n)} + \alpha^{(n)} s^{(n)} \quad (\text{C.21})$$

where $x^{(n+1)}$ and $x^{(n)}$ are the x for $(n+1)^{\text{th}}$ and n^{th} iterations respectively. $s^{(n)}$ is the search direction for the n^{th} iteration and $\alpha^{(n)}$ is the weighting parameter that controls the size of search direction. In this method, the search direction can be found as [30, 79, 100, 101]

$$s^{(n)} = g^{(n)} + \beta^{(n)} s^{(n-1)} \quad (\text{C.22})$$

where $g^{(n)}$ is the gradient of the cost function for the i^{th} iteration. The coefficient β is a scalar parameter. There are different methods to find this coefficient such as the classical form and Polak-Ribiere formula [79]. In the classical conjugate gradient method, β can be found as [30, 79]

$$\beta = \frac{\|g^{(n)}\|_2^2}{\|g^{(n-1)}\|_2^2} \quad (\text{C.23})$$

It should be noted that β is zero in the first iteration. The gradient of the cost function is shown in (C.11). The only unknown parameter for the CG is $\alpha^{(n)}$. It should be noted that $\alpha^{(n)}$ should be chosen in such a way that minimizes the cost function [30, 101]. Therefore, we will have

$$\left. \frac{\partial C_n}{\partial \alpha} \right|_{x=x^{(n+1)}} = 0 \quad (\text{C.24})$$

The cost function for the multiplicative regularization at $x = x^{(n+1)}$ is

$$C_n(x = x^{(n+1)}) = \|Ax^{(n+1)} - b\|_2^2 \left(\|d_n \nabla x^{(n+1)}\|_2^2 + \delta_n^2 \|d_n\|_2^2 \right) \quad (\text{C.25})$$

Substituting (C.21) into (C.25), we have

$$\begin{aligned}
C_n|_{x^{(n+1)}} &= \|A(x^{(n)} + \alpha^{(n)}s^{(n)}) - b\|_2^2 \left(\|d_n \nabla(x^{(n)} + \alpha^{(n)}s^{(n)})\| + \delta_n^2 \|d_n\|_2^2 \right) \\
&= \|(Ax^{(n)} - b) + A\alpha^{(n)}s^{(n)}\|_2^2 \left(\|d_n \nabla x^{(n)} + d_n \alpha^{(n)} \nabla s^{(n)}\|_2^2 + \delta_n^2 \|d_n\|_2^2 \right)
\end{aligned} \tag{C.26}$$

or it can be written as

$$\begin{aligned}
C_n|_{x^{(n+1)}} &= \left(\|Ax^{(n)} - b\|_2^2 + [\alpha^{(n)}]^2 \|As^{(n)}\|_2^2 + 2\alpha^{(n)} \text{Re} \langle Ax^{(n)} - b, As^{(n)} \rangle \right) \\
&\quad \times \left(\|d_n \nabla x^{(n)}\|_2^2 + \delta_n^2 \|d_n\|_2^2 + [\alpha^{(n)}]^2 \|d_n \nabla s^{(n)}\|_2^2 + 2\alpha^{(n)} \text{Re} \langle d_n \nabla x^{(n)}, d_n \nabla s^{(n)} \rangle \right)
\end{aligned} \tag{C.27}$$

For the simplicity in writing, we define the following parameters.

$$T_1 \triangleq \|Ax^{(n)} - b\|_2^2 \tag{C.28}$$

$$T_2 \triangleq \|As^{(n)}\|_2^2 \tag{C.29}$$

$$T_3 \triangleq 2\text{Re} \langle Ax^{(n)} - b, As^{(n)} \rangle \tag{C.30}$$

$$T_4 \triangleq \|d_n \nabla x^{(n)}\|_2^2 + \delta_n^2 \|d_n\|_2^2 \tag{C.31}$$

$$T_5 \triangleq \|d_n \nabla s^{(n)}\|_2^2 \tag{C.32}$$

$$T_6 \triangleq 2\text{Re} \langle d_n \nabla x^{(n)}, d_n \nabla s^{(n)} \rangle \tag{C.33}$$

Using the above parameters, (C.27) can be written as

$$C_n|_{x=x^{(n+1)}} = \left[T_1 + [\alpha^{(n)}]^2 T_2 + \alpha^{(n)} T_3 \right] \times \left[T_4 + [\alpha^{(n)}]^2 T_5 + \alpha^{(n)} T_6 \right] \tag{C.34}$$

Therefore, the gradient of the cost function with respect to $\alpha^{(n)}$ can be found as

$$\begin{aligned}
\left. \frac{\partial C_n}{\partial \alpha^{(n)}} \right|_{x=x^{(n+1)}} &= \left(2\alpha^{(n)}T_2 + T_3 \right) \left(T_4 + [\alpha^{(n)}]^2T_5 + \alpha^{(n)}T_6 \right) \\
&+ \left(T_1 + [\alpha^{(n)}]^2T_2 + \alpha^{(n)}T_3 \right) \left(2\alpha^{(n)}T_5 + T_6 \right) \\
&= (4T_2T_5)[\alpha^{(n)}]^3 + 3(T_2T_6 + T_3T_5)[\alpha^{(n)}]^2 \\
&+ 2(T_2T_4 + T_3T_6 + T_1T_5)\alpha^{(n)} \\
&+ (T_3T_4 + T_1T_6) = 0
\end{aligned} \tag{C.35}$$

Thus, $\alpha^{(n)}$ can be found by solving (C.35).

D

L_1 -norm Regularization

L_1 -norm [32,33,81,106] is one type of additive regularization method in which the penalty term is the first-norm of the solution. Therefore, the cost function for this type of regularization method will be [33,107]

$$C^{L_1} = \|Ax - b\|_2^2 + \alpha \|x\|_1 \quad (\text{D.1})$$

where α is a regularization parameter and C^{L_1} is denoted for the L_1 regularization cost function. As can be seen in (D.1), the cost function consists of two parts. The first part corresponds to the least square solution and two-norm is used for this part. The second part corresponds to the penalty term and the first-norm is used in this part. Sometimes, instead of using the first-norm of solution as a penalty term, the first norm of the gradient of the solution can be used [81,106]. This term is called the total variation of the solution [106]. Thus, the total variation of x is defined as [106]

$$TV(x) = \|\nabla x\|_1 \quad (\text{D.2})$$

Therefore, we can also have the following cost function for the L_1 regularization.

$$C^{L_1} = \|Ax - b\|_2^2 + \alpha \|\nabla x\|_1 \quad (\text{D.3})$$

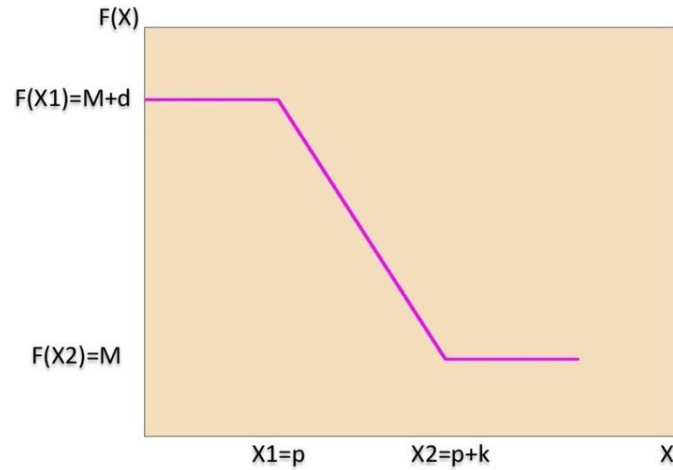


Figure D.1: A linear function used to compare the penalty term for L_1 -norm with Tikhonov regularization.

This regularization is very good in terms of finding the edges of the OI [30, 32]. However, it is computationally expensive (minimization of the cost function requires nonlinear optimization methods) and also it is difficult to find the regularization parameter [30]. To have a better understanding of how L_1 -norm has an edge preserving effect on the solution, we use an example to compare the penalty term in Tikhonov and L_1 -norm regularization [81]. Let's assume that we have the function shown in Figure D.1 [81]. In this case, the m -norm of the gradient of $F(x)$ can be found as (The following discussion is based on [81].)

$$\begin{aligned}
 \|\nabla F(x)\|_m &= \left[\int_{-\infty}^{\infty} |F'(x)|^m dx \right]^{\frac{1}{m}} = \left[\int_{x_1=p}^{x_2=p+k} \left(\frac{-d}{k} \right)^m dx \right]^{\frac{1}{m}} \\
 &= - \left[d^m k^{1-m} \right]^{\frac{1}{m}} = -dk^{\frac{1-m}{m}}
 \end{aligned} \tag{D.4}$$

Therefore, the first and second norm of $\nabla F(x)$ will be

$$\left\{ \begin{array}{ll} \|\nabla F(x)\|_{m=1} = -d & \text{First-norm} \\ \|\nabla F(x)\|_{m=2} = -\frac{d}{\sqrt{k}} & \text{Second-norm} \end{array} \right. \quad (\text{D.5})$$

According to above equation, the variation of k doesn't affect $\|\nabla F(x)\|_1$. However, it affects the second-norm. For example, the variation of $\|\nabla F(x)\|_2$ for the small and large values of k is:

$$\left\{ \begin{array}{ll} \text{If } k \text{ is too small } (k \rightarrow 0) & \text{Then } \|\nabla F(x)\|_2 \rightarrow \infty \\ \text{If } k \text{ is too large } (k \rightarrow \infty) & \text{Then } \|\nabla F(x)\|_2 \rightarrow 0 \end{array} \right.$$

Therefore, as explained above when we have a rapid change (i.e., having a small k value, which corresponds to an edge), the penalty term for Tikhonov regularization (second-norm) will be a large quantity [81]. Thus, the cost function will be dominated by the penalty term. Due to this, the residual error ($\|Ax - b\|_2^2$) will not be sufficiently minimized. Thus, the final solution will have a large data misfit error; i.e., it will be far from the true solution. Therefore, the Tikhonov regularization method which utilizes the second-norm has some issues for reconstruction of edges. On the other hand, the penalty term for L_1 -norm regularization method is independent of k . Therefore, for a rapid change, the penalty term doesn't go to infinity. Therefore, we can maintain a good balance between the data misfit error and the regularization term. Thus, we can reach a reasonable solution while reconstructing the edges of the OI.

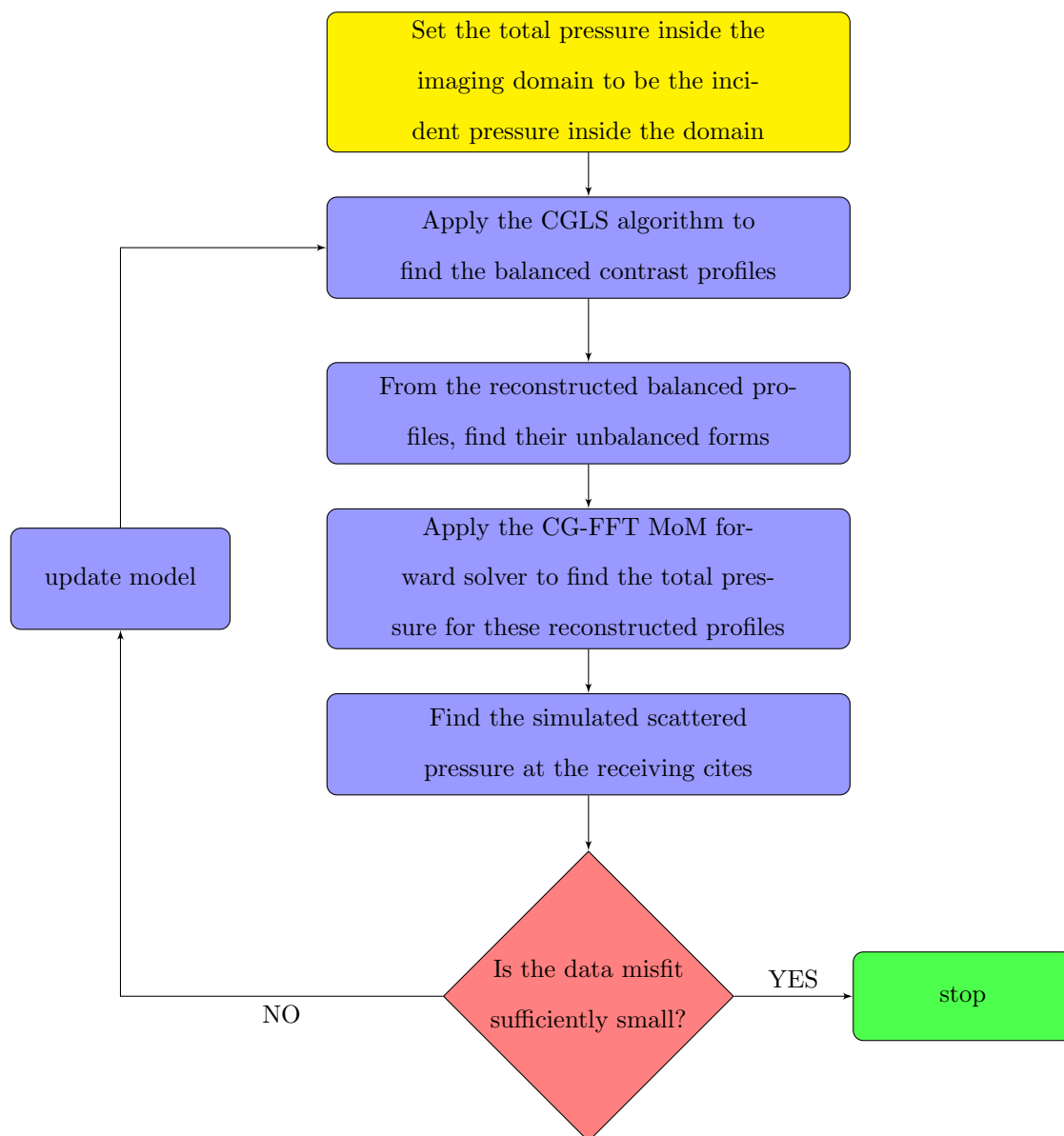
E

Flowchart of the Inversion Algorithm

In this appendix, the flowchart of the overall inversion algorithm is illustrated. As can be seen, this algorithm consists of three main parts:

1. the BIM which governs the iterative nature of the inversion algorithm.
2. the CG-FFT MoM, which acts as the forward solver of the algorithm.
3. the CGLS technique, which acts as the regularization scheme of the algorithm.

In the next page, this flowchart is shown.



References

- [1] G. Faucher, “Calibration of an ultrasound tomography system for medical imaging via 2-D contrast source inversion,” MSc. dissertation, 2012.
- [2] W. Chew, G. Otto, W. H. W. and J. H. Lin, and Y. M. Wang, “Nonlinear diffraction tomography the use of inverse scattering for imaging,” *International Journal of Imaging Systems and Technology*, 1993.
- [3] M. Moghaddam and W. C. Chew, “Study of some practical issues in inversion with the born iterative method using time domain data,” *Antennas and Propagation, IEEE Transactions on*, vol. 41, no. 2, pp. 177–184, February 1993.
- [4] P. Mojabi, M. Ostadrahimi, L. Shafai, and J. LoVetri, “Microwave tomography techniques and algorithms: A review,” *ANTEM*, 2012.
- [5] P. Mojabi and J. LoVetri, “Comparison of TE and TM inversions in the framework of the gauss-newton method,” *Antennas and Propagation, IEEE Transactions on*, vol. 58, no. 4, pp. 1336–1348, April 2010.
- [6] P. Mojabi and J. Lovetri, “Simultaneous Reconstruction of Compressibility and Density Profiles in Multiple Frequency Acoustic Inverse Scattering,” *APS/URSI*, 2013.
- [7] M. Haynes and M. Moghaddam, “Large domain, low contrast acoustic inverse scattering for ultrasound breast imaging,” *Biomedical Engineering, IEEE Transactions on*, vol. 57, no. 11, pp. 2712–2722, Nocember 2010.
- [8] W. C. Chew and J. H. Lin, “A frequency-hopping approach for microwave imaging of large inhomogeneous bodies,” *Microwave and Guided Wave Letters, IEEE*, 1995.
- [9] O. S. Haddadin and E. S. Ebbini, “Imaging strongly scattering media using a multiple frequency distorted born iterative method,” *Ultrasonics, Ferroelectrics and Frequency Control, IEEE Transactions on*, vol. 45, no. 6, pp. 1485–1496, November 1998.

-
- [10] R. F. Bloemenkamp, A. Abubakar, and P. M. van den Berg, “Inversion of experimental multi-frequency data using the contrast source inversion method,” *Inverse Problems*, 2001.
- [11] M. Li, O. Semerci, and A. Abubakar, “A contrast source inversion method in the wavelet domain,” *Inverse Problems*, 2013.
- [12] J. D. Shea, P. Kosmas, S. C. Hagness, and B. D. V. Veen, “Three-dimensional microwave imaging of realistic numerical breast phantoms via a multiple-frequency inverse scattering technique,” *Medical Physics*, vol. 37, no. 8, pp. 4210–4226, August 2010.
- [13] W. Hu, A. Abubakar, and T. M. Habashy, “Simultaneous multifrequency inversion of full-waveform seismic data,” *Geophysics*, vol. 74, no. 2, April 2009.
- [14] T. D. Mast, “Empirical relationships between acoustic parameters in human soft tissues,” *Acoustics Research Letters Online*, November 2000.
- [15] A. J. Hesford and R. C. Waag, “Reduced-rank approximations to the far-field transform in the gridded fast multiple method,” *Journal of Computational Physics*, February 2011.
- [16] M. Moghaddam and W. C. Chew, “Nonlinear two dimensional velocity profile inversion using time domain data,” *Geoscience and Remote Sensing, IEEE Transactions on*, vol. 30, no. 1, pp. 147–156, January 1992.
- [17] J. Hadamard, *Lectures on Cauchy’s Problem in Linear Partial Differential Equations*, Yale University Press, 1923.
- [18] M. Moghaddam and W. C. Chew, “Simultaneous inversion of compressibility and density in the acoustic inverse problem,” *Inverse Problems*, 1993.
- [19] R. Lavarello and M. Oelze, “A study on the reconstructions of moderate contrast targets using the distorted born iterative method,” *Ultrasonics, IEEE Transactions on*, vol. 55, no. 1, pp. 112–124, January 2008.
- [20] R. J. Lavarello and M. L. Oelze, “Density imaging using inverse scattering,” *The Journal of the Acoustical Society of America*, vol. 125, no. 2, pp. 793–802, February 2009.
- [21] A. J. Hesford and W. C. Chew, “Fast inverse scattering solutions using the distorted born iterative method and the multilevel fast multipole algorithm,” *The Journal of the Acoustical Society of America*, vol. 128, no. 2, pp. 679–690, June 2010.

- [22] T. Tran-Duc, N. L. Trung, and M. N. Do, "Modified distorted born iterative method for ultrasound tomography by random sampling," *Communications and Information Technologies (ISCIT), 2012 International Symposium on*, 2012.
- [23] K. W. A. van Dongen and W. M. D. Wright, "A full vectorial contrast source inversion scheme for three dimensional acoustic imaging of both compressibility and density profiles," *The Journal of the Acoustical Society of America*, vol. 121, no. 3, pp. 1538–1549, March 2007.
- [24] T. Rubak, P. M. Meaney, P. Meincke, and K. D. Paulsen, "Nonlinear Microwave Imaging for Breast Cancer Screening Using Gauss Newton's Method and the CGLS Inversion algorithm," *Antennas and Propagation, IEEE Transactions on*, vol. 55, no. 8, pp. 2320–2331, August 2007.
- [25] P. Mojabi and J. LoVetri, "Enhancement of the krylov subspace regularization for microwave biomedical imaging," *Medical Imaging, IEEE Transactions on*, vol. 28, no. 12, pp. 2015–2019, December 2009.
- [26] A. N. Tikhonov and V. Y. Arsenin, *Solutions of Ill-posed problems*. New York: John Wiley and Sons, 1977.
- [27] P. C. Hansen, *Rank Deficient and Discrete ill-posed problems*, Philadelphia.
- [28] W. C. Chew and Y. M. Wang, "Reconstruction of two dimensional permittivity distribution using the distorted born iterative method," *Medical Imaging, IEEE Transactions on*, vol. 9, no. 2, pp. 218–225, June 1990.
- [29] G. L. Wang, W. C. Chew, T. J. Cui, A. A. Ayadiner, D. L. Wright, and D. V. Smith, "3D near-to-surface conductivity reconstruction by inversion of VETEM data using the distorted born iterative method," *Inverse Problems*, vol. 20, November 2004.
- [30] A. Abubakar, P. M. van den Berg, T. M. Habashy, and H. Braunsch, "A multiplicative regularization approach for deblurring problems," *Image Processing, IEEE Transactions on*, vol. 13, no. 11, pp. 1524–1532, November 2004.
- [31] P. M. van den Berg, A. Abubakar, and J. T. Fokkema, "Multiplicative regularization for deblurring contrast profile inversion," *Radio Science*, 2003.
- [32] T. T. Duc, N. L. Trung, M. L. Oelze, and M. N. Do, "Application of L1 regularization for high quality reconstruction of ultrasound tomography," *IFMBE Proceedings*, 2012.
- [33] S. J. Kim, K. Koh, M. Lustig, S. Boyd, and D. Gorinevsky, "An interior point method for large scale L1 regularization least squares," *Selected Topics in Signal Processing, IEEE Journal of*, vol. 1, no. 4, pp. 606–617, December 2007.

- [34] P. Huthwaite, F. Simonetti, and N. Duric, “Combining time of flight and diffraction tomography for high resolution breast imaging: Initial in vivo results (1),” *The Journal of the Acoustical Society of America*, vol. 132, no. 3, pp. 1249–1252, September 2012.
- [35] C. Li, N. Duric, and L. Huang, “Comparison of ultrasound attenuation tomography methods for breast imaging,” *Ultrasonic Imaging and Signal Processing*, 2008.
- [36] P. Huthwaite and F. Simonetti, “High-resolution imaging without iteration: A fast and robust method for breast ultrasound tomography,” *The Journal of the Acoustical Society of America*, vol. 130, no. 3, pp. 1721–1734, September 2011.
- [37] C. Li, N. Duric, P. Littrup, and L. Huang, “In vivo breast sound-speed imaging with ultrasound tomography,” *Ultrasound in Medicine and Biology*, 2009.
- [38] J. Wiskin, D. T. Borup, S. A. Johnson, and M. Berggren, “Non linear inverse scattering: High resolution quantitative breast tissue tomography,” *The Journal of the Acoustical Society of America*, vol. 131, no. 5, pp. 3802–3813, May 2012.
- [39] F. Kamangar, G. M. Dores, and W. F. Anderson, “Patterns of cancer incidence, mortality, and prevalence across five continents: Defining priorities to reduce cancer disparities in different geographic regions of the world,” *Journal of Clinical Oncology*, vol. 24, no. 4, pp. 2137–2150, May 2006.
- [40] A. Dhawan, *Medical Image Analysis*. New Jersey: Wiley Inter Science, 2003.
- [41] M. Kriege, C. T. Brekelmans, C. B. nad Peter E. Besnard, H. M. Zonderland, and I. M. Obdeijn, “Efficacy of MRI and mammography for breast-cancer screening in women with a familial or genetic predisposition,” *The New England Journal of Medicine*, vol. 351, no. 25, pp. 427–437, July 2004.
- [42] N. Duric, P. Littrup, L. Poulou, A. Babkin, R. Pevzner, E. Holsapple, O. Rama, and C. Glide, “Detection of breast cancer with ultrasound tomography: First results with the computed ultrasound risk evaluation (cure) prototype,” *American Association of Physicists in Medicine.*, vol. 34, no. 2, pp. 773–785, February 2007.
- [43] F. Simonetti, L. Huang, and N. Duric, “A multiscale approach to diffraction tomography of complex three dimensional objects,” *American Institute of Physics*, August 2009.
- [44] T. Szabo, *Diagnostic Ultrasound Imaging*. Elsevier Academic Press, 2004.
- [45] A. Hormati, I. Jovanovic, O. Roy, and M. Vetterli, “Robust ultrasound travel time tomography using the bent ray model.”

- [46] A. C. K. Malcolm Salaney and L. E. Larsen, "Limitations of imaging with first order diffraction tomography," *Microwave Theory and Techniques, IEEE Transactions on*, vol. 32, no. 8, pp. 860–874, August 1984.
- [47] M. Oristaglio and H. Blok, *Wavefield Imaging and Inversion in Electromagnetics and Acoustics*, Delf University, 1995.
- [48] R. Pierri, G. Leone, and R. Persico, "Second order iterative approach to inverse scattering: numerical results," *J. Opt. Soc. Am*, vol. 17, no. 5, pp. 874–880, May 2000.
- [49] J. Wiskin, D. T. Borup, S. A. Johnson, and M. Berggren, "Non-linear inverse scattering: resolution quantitative breast tissue tomography," *Journal of the Acoustical Society of America*, vol. 131, no. 5, pp. 3802–3813, May 2012.
- [50] F. Lin, A. I. Nachman, and R. C. Waag, "Quantitative imaging using a time-domain eigenfunction method," *The Journal of the Acoustical Society of America*, vol. 108, no. 3, pp. 899–912, September 2000.
- [51] T. D. Mast, A. I. Nachman, and R. C. Waag, "Focusing and imaging using eigenfunctions of the scattering operator," *The Journal of the Acoustical Society of America*, vol. 102, no. 2, pp. 715–725, August 1997.
- [52] S. A. Goss, R. L. Johnston, and F. Dunn, "Comprehensive compilation of empirical ultrasonic properties of mammalian tissues," *The Journal of the Acoustical Society of America*, vol. 64, no. 2, pp. 423–457, August 1978.
- [53] M. Moghaddam and W. C. Chew, "Variable density linear acoustic inverse problem," *Ultrasonic Imaging*, 1993.
- [54] P. Mojabi and J. LoVetri, "A Fast and Efficient MoM Forward Solver for Ultrasound Tomography of Inhomogeneous Compressibility and Density Profiles," *APS/URSI*, 2013.
- [55] G. H. Golub, M. Heath, and G. Wahba, "Generalized cross validation as a method for choosing a good ridge parameter," *Technometrics*, vol. 21, no. 2, pp. 215–223, May 1979.
- [56] D. H. Staelin, A. Morgenthaler, and J. Kong, *Electromagnetic Waves*. New Jersey: Prentice Hall, 1994.
- [57] D. A. Russell. (2011, October) Acoustics and vibration animations. Pennsylvania State University. [Online]. Available: <http://www.acs.psu.edu/drussell/demos/waves/wavemotion.html>

- [58] M. O'Donnell, E. T. Jaynes, and J. G. Miller, "Kramers-kronig relationship between ultrasonic attenuation and phase velocity," *The Journal of the Acoustical Society of America*, November 1980.
- [59] P. M. Morse and K. U. Ingard, *Theoretical Acoustics*. Princeton University Press, 1968.
- [60] A. J. Hesford and R. C. wagg, "The fast multiple method and fourier convolution for the solution of acoustic scattering on regular volumetric grids," *Journal of Computational Physics*, July 2010.
- [61] [Online]. Available: <http://www.ase.uc.edu/~pnagy/ClassNotes/AEEM729%20Ultrasonic%20NDE/Part%203.pdf>
- [62] N. Duric and P. Littrup, "Development of ultrasound tomography for breast imaging: Technical assessment," *Medical Physics*, vol. 32, no. 5, May 2005.
- [63] J. F. Greenleaf, J. Ylitalo, and J. J. Gisvold, "Ultrasonic computed tomography for breast examination," *Engineering in Medicine and Biology Magazine, IEEE*, December 1987.
- [64] E. L. Madsen, J. A. Zagzebski, and G. R. Frank, "An anthropomorphic ultrasound breast phantom containing intermediate sized scatterers," *Ultrasound in Medicine and Biological*, 1982.
- [65] E. L. Madsen, W. A. Berg, E. B. Mendelson, and G. R. Frank, "Anthropomorphic breast phantoms for qualification of investigation for acrin protocol 6666," *Radiology*, vol. 239, no. 3, pp. 869–874, June 2006.
- [66] O. M. Bucci, N. Cardace, L. Crocco, and T. Isernia, "Degree of nonlinearity and a new solution procedure in scalar two-dimensional inverse scattering problems," *J. Opt. Soc. Am. A*, vol. 18, no. 8, pp. 1832–1843, Aug 2001. [Online]. Available: <http://josaa.osa.org/abstract.cfm?URI=josaa-18-8-1832>
- [67] T. L. Chow, *Mathematical Methods for Physicists: A concise introduction*. Cambridge University Press, 2000.
- [68] P. M. van den Berg and R. E. Kleinman, "A contrast source inversion method," *Inverse Problems*, July 1997.
- [69] J. D. Zaeytjyd, A. Franchois, C. Eyraud, and J. M. Geffrin, "Full Wave Three Dimensional Microwave Imaging With a Regularized Gauss Newton Method Theory and Experiment," *Antennas and Propagation, IEEE Transactions on*, vol. 55, no. 11, pp. 3279–3292, November 2007.
- [70] [Online]. Available: http://en.wikipedia.org/wiki/Toeplitz_matrix

- [71] [Online]. Available: http://en.wikipedia.org/wiki/Circulant_matrix
- [72] P. Hansen, "Deconvolution and Regularization with Toeplitz Matrices," *Numerical Algorithms*, vol. 29, no. 4, pp. 323–378, 2002. [Online]. Available: <http://dx.doi.org/10.1023/A%3A1015222829062>
- [73] A. Abubakar, G. Pan, and T. M. Habashi, "Application of the source-receiver compression scheme for 3D microwave data inversions," *Antennas and Propagation (APSURSI), IEEE International Symposium.*, July 2011.
- [74] P. Mojabi and J. LoVetri, "A Prescaled Multiplicative Regularized Gauss-Newton inversion," *Antennas and Propagation, IEEE Transactions on*, vol. 59, no. 8, pp. 2954–2963, 2011.
- [75] S. B. Kjoller, "Parameter Estimation for Large-Scale Reconstruction," Master's thesis, Technical University of Denmark, 2007.
- [76] [Online]. Available: http://en.wikipedia.org/wiki/Well-posed_problem
- [77] J. De Zaeytjij, A. Franchois, C. Eyraud, and J. M. Geffrin, "Full-wave three-dimensional microwave imaging with a regularized gauss newton method theory and experiment," *Antennas and Propagation, IEEE Transactions on*, vol. 55, no. 11, pp. 3279–3292, 2007.
- [78] A. Kirsch, *An Introduction to the Mathematical Theory of Inverse Problems*. New York: Springer-Verlag, 1996.
- [79] M. Oristaglio and H. Block, *Wavefield Imaging and Inversion in Electromagnetics and Acoustics*. Delft University course notes, 1995.
- [80] P. C. Hansen, "Numerical tools for analysis and solution of Fredholm integral equations of the first kind," *Inverse Problems.*, January 1992.
- [81] J. Pederson, "Modular Algorithms for Large-scale total variation image deblurring," Master's thesis, Technical University of Denmark, 2005.
- [82] R. L. Parker, *Geophysical Inverse Theory*. Princeton University Press, 1994.
- [83] P. Hansen, "Regularization tools: A matlab package for analysis and solution of discrete ill-posed problems," *Numerical Algorithms*, vol. 6, no. 1, pp. 1–35, 1994. [Online]. Available: <http://dx.doi.org/10.1007/BF02149761>
- [84] P. Mojabi, J. LoVetri, and L. Shafai, "A Multiplicative Regularized Gauss Newton Inversion for Shape and Location Reconstruction," *Antennas and Propagation, IEEE Transactions on*, vol. 59, no. 12, pp. 4790–4802, December 2011.

- [85] S. R. Buss, "Introduction to inverse kinematics with jacobian transpose, pseudoinverse and damped least squares methods," *IEEE Journal of Robotics and Automation*, Tech. Rep., 2004.
- [86] C. Wampler, "Manipulator inverse kinematic solutions based on vector formulations and damped least-squares methods," *Systems, Man and Cybernetics, IEEE Transactions on*, vol. 16, no. 1, pp. 93–101, 1986.
- [87] P. C. Hansen, "Analysis of discrete ill-posed problems by means of the L-curve," *Society for Industrial and Applied Mathematics*, vol. 34, no. 4, pp. 561–580, December 1992.
- [88] T. K. Jensen, "Stabilization algorithms for large-scale problems," Ph.D. dissertation, Technical University of Denmark, 2006.
- [89] P. C. Hansen, M. E. Kilmer, and R. H. Kjeldsen, "Exploiting residual information in the parameter choice for discrete ill-posed problems," *BIT Numerical Mathematics*, vol. 46, no. 1, pp. 41–59, 2006. [Online]. Available: <http://dx.doi.org/10.1007/s10543-006-0042-7>
- [90] P. M. van den Berg and A. Abubakar, "Contrast source inversion of 3D objects with electric and magnetic contrasts," *2004 URSI/EMTS Proceedings of the International Symposium on Electromagnetic Theory*, pp. 700–702, 2004.
- [91] P. C. Hansen, *Tutorial: Algebraic Iterative Reconstruction*. Technical University of Denmark, 2012.
- [92] [Online]. Available: <http://www.astm.org/BOOKSTORE/DS68/pg41.pdf>
- [93] [Online]. Available: <http://www.engineeringtoolbox.com/sound-speed-water-d.598.html>
- [94] E. L. Madsen, M. A. Hobson, G. R. Frank, H. Shi, J. Jiang, T. J. Hall, T. Varghese, M. M. Doyley, and J. B. Weaver, "Anthropomorphic breast phantoms for testing elastography systems," *Medicine and Biology, Ultrasound in*, vol. 32, no. 6, pp. 857–874, 2006.
- [95] M. O. Culjat, D. Goldenberg, P. Tewari, and R. S. Singh, "A review of tissue substitutes for ultrasound imaging," *Medicine and Biology, Ultrasound in*, vol. 36, no. 6, pp. 861–873, 2010.
- [96] J. Dang, B. Frisch, P. Lasaygues, D. Zhang, S. Tavernier, N. Felix, P. Lecoq, E. Auffray, J. Varela, S. Mensah, and M. Wan, "Development of an Anthropomorphic Breast Phantom for Combined PET, B-Mode Ultrasound and Elastographic Imaging," *Nuclear Science, IEEE Transactions on*, vol. 58, no. 3, pp. 660–667, 2011.

- [97] P. Huthwaite and F. Simonetti, "High-resolution imaging without iteration: A fast and robust method for breast ultrasound tomography," *The Journal of the Acoustical Society of America*, vol. 130, no. 3, pp. 1721–1734, 2011.
- [98] J. Richmond, "Scattering by a dielectric cylinder of arbitrary cross section shape," *Antennas and Propagation, IEEE Transactions on*, vol. 13, no. 3, pp. 334–341, 1965.
- [99] A. Elsherbeni and V. Demir, *The Finite Difference Time Domain Method for Electromagnetics: With MATLAB Simulations*. SciTech Publishing, Incorporated, 2009. [Online]. Available: <http://books.google.ca/books?id=3KMKOwAACAAJ>
- [100] M. R. Hestenes and E. Stiefel, "Methods of Conjugate Gradients for Solving Linear Systems," *Journal of Research of the National Bureau of Standards*, vol. 49, no. 6, pp. 409–436, 1952.
- [101] J. R. Shewchuk, *An Introduction to the Conjugate Gradient Method Without the Agonizing Pain*. Pittsburgh: School of Computer Science Carnegie Mellon University, 1994.
- [102] A. Abubakar, T. Habashy, G. Pan, and M.-K. Li, "Application of the Multiplicative Regularized Gauss-Newton Algorithm for Three-Dimensional Microwave Imaging," *Antennas and Propagation, IEEE Transactions on*, vol. 60, no. 5, pp. 2431–2441, 2012.
- [103] P. Mojabi and J. LoVetri, "Microwave Biomedical Imaging Using the Multiplicative Regularized Gauss-Newton Inversion," *Antennas and Wireless Propagation Letters, IEEE*, vol. 8, pp. 645–648, 2009.
- [104] P. Mojabi, J. LoVetri, and L. Shafai, "A Multiplicative Regularized Gauss Newton Inversion for Shape and Location Reconstruction," *Antennas and Propagation, IEEE Transactions on*, vol. 59, no. 12, pp. 4790–4802, 2011.
- [105] P. Mojabi and J. LoVetri, "Overview and Classification of Some Regularization Techniques for the Gauss-Newton Inversion Method Applied to Inverse Scattering Problems," *Antennas and Propagation, IEEE Transactions on*, vol. 57, no. 9, pp. 2658–2665, 2009.
- [106] D. C. Dobson and C. R. Vogel, "Convergence of an Iterative Method For Total Variation Denoising," *Society for Industrial and Applied Mathematics*, vol. 34, no. 5, pp. 1779–1791, October 1997.
- [107] S.-J. Kim, K. Koh, M. Lustig, and S. Boyd, "An efficient method for compressed sensing," in *Image Processing, 2007. ICIP 2007. IEEE International Conference on*, vol. 3, 2007, pp. III – 117–III – 120.